

Texas A&M University
J. Mike Walker 66' Department of Mechanical Engineering
Turbomachinery Laboratory
Tribology Group

**A NONHOMOGENEOUS BULK FLOW MODEL FOR PREDICTION OF
THE STATIC AND DYNAMIC FORCED PERFORMANCE OF TWO
PHASE FLOW ANNULAR SEALS**

TRC-SEAL-02-20

Research Progress Report to the Turbomachinery Research Consortium

by

Xueliang Lu

PhD Candidate

Luis San Andrés

Mast-Childs Chair Professor
Principal Investigator

June 2020

TRC Project, TEES # 400124-00079

EXECUTIVE SUMMARY

In the subsea oil and gas industry, multiphase pumps and wet gas compressors are preferred technologies as they eliminate a conventional liquid-gas separation station to save up to 30% of capital investment. Seals in multiple phase pumps must be able to operate without compromising the system efficiency and its rotordynamic stability. However, both field operation and laboratory tests show that seals operating with liquid-gas mixtures could cause rotordynamic instability issues in a turbomachinery.

This report advances a nonhomogeneous bulk flow model (NHBFM) for the prediction of the leakage and dynamic force coefficients of uniform clearance annular seals lubricated with gas in liquid mixtures. Compared to a homogeneous bulk flow model (HBFM) the NHBFM contains four diffusion coefficients in the inertia terms of the momentum equations, and a transport equation for the gas volume fraction (GVF).

To validate the model, predictions on leakage and dynamic force coefficients are compared against published results for three test seals supplied with a two-phase flow mixture. Two seals with a supply pressure $P_s = 44.8$ bara and a discharge pressure $P_a = 6.9$ bara emulate operating conditions in a subsea multiphase pump. The seals have the same diameter $D = 89.3$ mm and length $L = 57.8$ mm ($L/D = 0.65$), but different radial clearances, i.e., $c = 0.140 \pm 0.005$ mm and 0.163 ± 0.005 mm, respectively. The shaft speed is 7,500 rpm (surface speed = 35 m/s), and the seal inlet GVF increases from 0 to 0.1. The mixture consists of compressed air and a synthetic oil with a low viscosity 4.53

cp at 40 °C and density of 899 kg/m³. The flow Reynolds number is within the range of 870 to 1,100, representing a laminar flow.

The third test seal operates in a very different operating condition with a low pressure ($P_s = 2.6$ bara, $P_a = 1$ bara) and low shaft speed 3,500 rpm (surface speed = 23.3 m/s). The flow is an air in ISO VG10 mineral oil mixture with an inlet GVF spans 0 to 0.2. The maximum flow Reynolds number is less than 300. Thus, the flow is in laminar flow regime. The small pressure drop $\Delta P = 1.6$ bar emulates operating conditions of impeller eye seals in electrical submersible pumps. The seal has a diameter $D = 127$ mm, length $L = 46$ mm ($L/D = 0.36$) and radial clearance $c = 0.274 \pm 0.005$ mm.

For the first test seal operating with $P_s = 44.8$ bara and inlet GVF=0.1, the flow is mostly homogeneous as the maximum diffusion velocity at the seal exit plane is just ~0.1% of the liquid flow velocity. Thus, both the NHBFM and HBFM predict similar results for the pressure field, gas volume fraction field, leakage (mass flow rate) and shear drag torque. The difference between the predicted leakage and test data is less than 5%.

For operation with a $P_s = 44.8$ bara the NHBFM predicted direct stiffness (K) reduces faster with inlet GVF than that predicted by the HBFM. Although the NHBFM delivers 30% larger added mass (M) than the HBFM does, both models do predict a drop in M with the increase of inlet GVF. Both models predict similar direct damping coefficient (C) and cross-coupled stiffness (k) with a maximum difference of ~5% in both C and k for operation with inlet GVF= 0.1. Compared to the test data, the two models generally under predict C and k by the same amount of ~ 25%. Both C and k increase with inlet GVF for operation with inlet GVF < 0.1. Closely matching the test data, both models deliver a whirl

frequency ratio (WFR) ~ 0.3 for the pure liquid seal. WFR increases to ~ 0.35 as the inlet GVF increases to 0.1.

For the third test seal operating with a low pressure ($P_s = 2.6$ bara) both the NHBFM and HBFM predict ~ 0 direct stiffness (K). For operation with inlet GVF=0.2, the NHBFM predicted M is 3.2 kg, about $\sim 30\%$ below the test data 4 kg; the HBFM predicts a zero M . C and k predicted by both models are within uncertainty of the test data. For operation with a pure liquid or a mixture both models deliver accurate predictions in whirl frequency ratio ($WFR \sim 0.5$).

The comparisons of the predictions against test data from two-phase flow uniform clearance annular seals demonstrate that the NHBFM shows an improvement in prediction of the seals dynamic forced performance; in particular in direct stiffness (K), as compared to a HBFM. The difference in the predictions from the two models is primarily due to the distinct approaches to model the perturbed density of the two-phase flow, as is addressed later in the main context.

In contrast to commercial computational fluid dynamics (CFD) software packages that require hours or even several days to obtain the dynamics force coefficients, the current NHBFM only takes one or two minutes to complete a prediction.

NOMENCLATURE

c	Seal radial clearance [m]
$C_{i,j}$	Seal direct damping coefficients [N.s/m], $i, j = X, Y$
$c_{i,j}$	Seal cross-coupled damping coefficients [N.s/m], $i, j = X, Y$
C_D	Drag coefficient [-]
d_g	Bubble diameter [m]
D	$D = 2R$, Journal diameter [m]
f_{drag}	Drag force between the interface of the liquid and gas [N]
f_r, f_s	Friction factor on rotor and stator surfaces [-]
k_r, k_s	$k_r = f_r Re_{mr}$, $k_s = f_s Re_{ms}$, Bulk flow shear parameters, $k_r = k_s = 12$ for laminar flow
H_{XX}, H_{YY}	Seal direct complex dynamic stiffnesses [m]
h	Dimensionless seal fluid film thickness [-]
h_0	Zeroth order dimensionless seal fluid film thickness [-]
$h_{x,y}$	First order dimensionless seal film thickness along the x and y directions [-]
h_{XX}, h_{YY}	Seal cross-coupled complex dynamic stiffness coefficients [m]
$K_{i,j}$	Seal direct stiffness coefficients [N/m], $i, j = X, Y$
$k_{i,j}$	Seal cross-coupled stiffness coefficients [N/m], $i, j = X, Y$
L	Seal length [mm]
\dot{m}_g, \dot{m}_l	Mass flow rate for pure gas and pure liquid [kg/s]
\dot{m}_m	$\dot{m}_m = \dot{m}_l + \dot{m}_g$, Mass flow rate of air in oil mixture [kg/s]
$M_{i,j}$	Seal direct mass coefficients [N.s/m], $i, j = X, Y$

$m_{i,j}$	Seal cross coupled mass coefficients [N.s/m], $i, j = X, Y$
N	Shaft rotational speed [rev/min]
P	Pressure [Pa]
P_a, P_s	Ambient pressure and supply pressure [Pa]
p	Dimensionless pressure [-]
p_0	Zeroth order dimensionless pressure [-]
$p_{x,y}$	First order dimensionless pressure along the x and y directions [-]
q_g, q_l	Volumetric flow rate for pure gas and pure liquid [m ³ /s]
Q_g, Q_l	Bulk flow volumetric flow rate for pure gas and pure liquid [m ³ /s]
r_1, r_2, r_3, r_4	Diffusion coefficients [-], Eqs. (26) to (28).
R	$R = 1/2 D$, Journal radius [m]
Re_{mc}	$Re_{mc} = \frac{\rho_m V_c c}{\mu_m}$, Mixture circumferential flow Reynolds number [-]
Re_{mz}	$Re_{mz} = \frac{\rho_m V_z c}{\mu_m} = \frac{\dot{m}_m}{\pi D \mu_m}$, Mixture axial flow Reynolds number [-]
Re_{ms}	$Re_{ms} = \frac{\rho_m H}{\mu_m} (U_m^2 + W_m^2)^{0.5}$, Mixture total Reynolds number/bulk flow Reynolds number relative to stator surface.
Re_{mr}	$Re_{mr} = \frac{\rho_m H}{\mu_m} ((U_m - \Omega R)^2 + W_m^2)^{0.5}$, Mixture bulk flow Reynolds number relative to rotor surface.
$Re_{B(X)}$	$Re_{B(X)} = \frac{\rho_l U_g - U_l d_g}{\mu_l}$, relative Reynolds number along circumferential

- direction [-]
- $Re_{B(Z)}$ $Re_{B(Z)} = \frac{\rho_l |W_g - W_l| d_g}{\mu_l}$, relative Reynolds number along axial direction [-]
- U_g, U_l, W_g, W_l Velocity of gas and liquid along circumferential and axial directions [m/s]
- $\bar{U}_g, \bar{U}_l, \bar{W}_g, \bar{W}_l$ Film averaged bulk flow velocity of gas and liquid along circumferential and axial directions [m/s]
- U_m, W_m Velocity of mixture along circumferential and axial directions [m/s]
- \bar{U}_m, \bar{W}_m Film averaged two-phase flow bulk flow velocity along circumferential and axial directions [m/s]
- U_{gl}, W_{gl} Relative velocity of the gas phase (secondary phase) to the liquid phase (primary phase) along circumferential and axial directions [m/s]
- $U_{dr,g}, W_{dr,g}$ Diffusion velocity of gas along circumferential and axial directions [m/s]
- $\bar{U}_{dr,g}, \bar{W}_{dr,g}$ Film averaged diffusion velocity of gas along circumferential and axial directions [m/s]
- u_m, w_m Dimensionless velocity of mixture along circumferential and axial directions
- u_{m_0}, w_{m_0} Zeroth order dimensionless velocity of mixture along circumferential and axial directions [-]
- $u_{m_{x,y}}, w_{m_{x,y}}$ First order dimensionless velocity of mixture along circumferential and axial directions [-]
- T Temperature [K]

t	Time [s]
V_z	$V_z = Q/\pi Dc$, Bulk flow axial velocity [m/s]
V_*	Characteristic flow speed due to pressure [m/s]
α_g, α_l	Volume fraction of gas and liquid [-]
$\bar{\alpha}_g, \bar{\alpha}_l$	Film averaged gas and liquid bulk flow volume fractions [-]
$\bar{\alpha}_{g_0}, \bar{\alpha}_{l_0}$	Zeroth order film averaged gas and liquid bulk flow volume fractions [-]
$\bar{\alpha}_{g_{x,y}}$	First order film averaged liquid and gas bulk flow volume fraction [-]
ζ	Test rig structural damping ratio [-]
ε	Seal eccentricity ratio [-]
λ_g, λ_l	Mass fraction of gas and liquid [-]
μ_g, μ_l	Gas and liquid viscosities [Pa.s]
$\bar{\mu}_g, \bar{\mu}_l$	Film averaged gas and liquid bulk flow viscosities [Pa.s]
$\tilde{\mu}_g, \tilde{\mu}_l$	Dimensionless film averaged gas and liquid bulk flow viscosities [-]
$\tilde{\mu}_{g_0}, \tilde{\mu}_{l_0}$	Zeroth order dimensionless film averaged gas and liquid bulk flow viscosities
$\tilde{\mu}_{g_{x,y}}$	First order dimensionless film averaged liquid and gas bulk flow viscosity [-]
μ_m	Two-phase flow effective viscosity [Pa.s]
$\bar{\mu}_m$	Film averaged two-phase flow bulk flow effective viscosity [Pa.s]
$\tilde{\mu}_m$	Dimensionless film averaged two-phase flow bulk flow effective viscosity [-]
$\tilde{\mu}_{m_0}$	Zeroth order dimensionless film averaged two-phase flow bulk flow effective

	viscosity [-]
$\tilde{\mu}_{m_{x,y}}$	First order dimensionless film averaged two-phase flow bulk flow effective viscosity [-]
ρ_g, ρ_l	Gas and liquid density [kg/m ³]
$\bar{\rho}_g, \bar{\rho}_l$	Film averaged gas and liquid bulk flow density [kg/m ³]
$\tilde{\rho}_g, \tilde{\rho}_l$	Dimensionless film averaged gas and liquid bulk flow density [-]
$\tilde{\rho}_{g_0}$	Zeroth order dimensionless film averaged gas bulk flow density [-]
$\tilde{\rho}_{g_{x,y}}$	First order dimensionless film averaged gas bulk flow density [-]
ρ_m	Two-phase fluid density [kg/m ³]
$\bar{\rho}_m$	Film averaged mixture bulk flow density [kg/m ³]
$\tilde{\rho}_m$	Dimensionless film averaged mixture bulk flow density [-]
$\tilde{\rho}_{m_0}$	Zeroth order dimensionless film averaged two-phase flow bulk flow density
$\tilde{\rho}_{m_{x,y}}$	First order dimensionless film averaged two-phase flow bulk flow density [-]
$\Delta e_x, \Delta e_y$	Small amplitude of journal motion about the static equilibrium position [-]
∇	$\nabla = \frac{\partial}{\partial x} \vec{i} + \frac{\partial}{\partial y} \vec{j} + \frac{\partial}{\partial z} \vec{k}$, gradient vector operator
Ω	Shaft angular speed [rad/s]
ω	Excitation frequency [rad/s]
τ_g	Relaxation time for a gas bubble change from an equilibrium state to another equilibrium state [s]

$\tau_x|_0^H, \tau_z|_0^H$ Bulk flow wall shear stresses along the X and Z directions [N/m²]

Γ_k Rate of mass transfer at the interface of liquid and gas

VECTORS

\mathbf{U}_g $\mathbf{U}_g = (U_g \vec{i}, V_g \vec{j}, W_g \vec{k})$, velocity vector of gas [m/s]

\mathbf{U}_l $\mathbf{U}_l = (U_l \vec{i}, V_l \vec{j}, W_l \vec{k})$, velocity vector of liquid [m/s]

\mathbf{U}_m $\mathbf{U}_m = (U_m \vec{i}, V_m \vec{j}, W_m \vec{k})$ velocity vector of mixture [m/s]

\mathbf{U}_{gl} $\mathbf{U}_{gl} = ((U_g - U_l) \vec{i}, (V_g - V_l) \vec{j}, (W_g - W_l) \vec{k})$ relative velocity vector of the gas phase (secondary phase) to the liquid phase (primary phase) [m/s]

$\mathbf{U}_{dr,g}$ $\mathbf{U}_{dr,g} = (U_{dr,g} \vec{i}, V_{dr,g} \vec{j}, W_{dr,g} \vec{k})$, diffusion velocity of gas [m/s]

$\mathbf{U}_{dr,l}$ $\mathbf{U}_{dr,l} = (U_{dr,l} \vec{i}, V_{dr,l} \vec{j}, W_{dr,l} \vec{k})$, diffusion velocity of gas [m/s]

SUBSCRIPTS

S Structure

a Ambient

g Gas

inlet Inlet plane of seal ($Z = 0$)

m Mixture or two component flow

l Liquid

ABBREVIATIONS

ASMM	Algebraic slip mixture model
BFM	Bulk flow model
CFD	Computational fluid dynamics
GVF	Gas volume fraction
GMF	Gas mass fraction
LVF	Liquid volume fraction
SSV	Sub-synchronous vibration
WFR	Whirl frequency ratio

TABLE OF CONTENTS

	Page
EXECUTIVE SUMMARY	ii
NOMENCLATURE	v
TABLE OF CONTENTS	xii
LIST OF FIGURES	xiv
LIST OF TABLES	xix
1. INTRODUCTION.....	1
2. LITERATURE REVIEW	6
2.1. Seals operating with two-phase flow caused by material phase change	6
2.2. Seals operating with two-phase flow and without phase change	8
2.3. Summary of research on two-phase flow seals since 2010 in the Turbomachinery Laboratory of Texas A&M University	13
3. THE NONHOMOGENEOUS BULK FLOW MODEL	19
3.1. Selection of a two-phase (component) flow model.....	19
3.2. Applying the ASMM to the flow in air-oil in annular seals.....	25
3.3. The bulk flow equations for a two-component mixture in annular seals	26
3.4. The dimensionless governing equations	31
3.5. Perturbation analysis	32
3.5.1. The zeroth order equations	34
3.5.2. The first order equations.....	41
3.6. Closure	44
4. RESULTS AND DISCUSSION	46
4.1. High pressure annular seal	46
4.1.1. Static characteristics	46
4.1.2. First order flow variables	54
4.1.3. Dynamic force coefficients	57
4.2. Low pressure annular seal	72
4.3. Closure	84

5. CONCLUSION	85
REFERENCES	89
APPENDIX A DERIVATION OF MOMENTUM EQUATIONS	95
APPENDIX B DERIVATION OF DIFFUSION VELOCITY	103
APPENDIX C SOLUTION OF THE ZEROth AND FIRST ORDER EQUATIONS	107
Numerical solution of the zeroth order equation.....	108
Numerical solution of the first order equation	117
APPENDIX D FORCE COEFFICIENTS OF HIGH PRESSURE ANNULAR SEAL	118

LIST OF FIGURES

	Page
Figure 1 Flow visualization of wet seal operating with a gas and oil mixture. Inlet GVF = 0 to 0.9, journal speed = 0 rpm. Pictures taken with a stroboscope light at 30 Hz. Seal inlet pressure (P_s) = 2.0 bar (a), discharge pressure (P_a) = 1 bara. Picture reproduced from Ref. [11].	4
Figure 2 Flow visualization of wet seal operating with a gas and oil mixture. Inlet GVF = 0.9, journal speed = 1,800 rpm. Pictures taken with a stroboscope light at 30 Hz. Seal inlet pressure (P_s) = 2.0 bar (a), discharge pressure (P_a) = 1 bara. Picture reproduced from Ref. [11].	5
Figure 3 A fluid domain and a control volume filled with liquid and dispersed gas bubbles [40].	20
Figure 4 Short and long geometric scales in a bubbly flow (a) long scale interfaces, (b) short scale interfaces [40].	22
Figure 5 Experimentally estimated air and oil velocity at the seal inlet plane [51]. Supply pressure (P_s) = 2.5 bar (abs), discharge pressure (P_a) = 1 bar (abs), shaft speed (N) = 3,500 rpm (shaft surface speed ΩR = 23.3 m/s). Oil temperature (T_{in}) = 33 °C ~35 °C.	39
Figure 6 Seal leakage for pure oil and two-phase flow condition. Supply pressure (P_s) = 44.8 bara, discharge pressure (P_a) = 6.9 bara, shaft speed (N) = 7,500 rpm (ΩR = 35.1 m/s). Inlet GVF=0, 0.02, 0.04, 0.06, 0.08, and 0.1. Test data from Ref. [55].	48
Figure 7 Predicted seal shear drag power for pure oil and two-phase flow condition. Supply pressure (P_s) = 44.8 bara, discharge pressure (P_a) = 6.9 bara, shaft speed (N) = 7,500 rpm (ΩR = 35.1 m/s). Inlet GVF=0, 0.02, 0.04, 0.06, 0.08, and 0.1.	49
Figure 8 Pressure along the seal axial location predicted by HBFM and NHBFM. Shaft speed 7,500 rpm, seal inlet pressure 44.8 bara, discharge pressure 6.9 bara.	51
Figure 9 Predicted gas volume fraction (GVF) versus the seal axial coordinate (Z/L). Shaft speed 7,500 rpm, seal inlet pressure 44.8 bara, discharge pressure 6.9 bara. Symbols: nonhomogeneous bulk flow model (NHBFM), Lines: homogeneous bulk flow model (HBFM).	52

Figure 10 Axial velocity difference between the liquid and gas components along the seal axial location. Shaft speed 7,500 rpm, seal inlet pressure 44.8 bara, discharge pressure 6.9 bara.....	53
Figure 11 Real and imaginary parts of the first order fluids variables (GVF_Y, ρ_{mY}, P_Y) versus circumferential direction (Θ), axial coordinate $Z = L/2$. Shaft speed 7,500 rpm, whirl frequency 1 HZ. Seal inlet pressure 44.8 bara.	55
Figure 12 Real part of the first order pressure $Re(P_Y)$ along the circumferential direction (Θ), axial coordinate $Z = L/2$. Shaft speed 7,500 rpm, whirl frequency 1 HZ. Seal inlet pressure 44.8 bara.	57
Figure 13 Real part of direct complex dynamic stiffness, $Re(H)_{XX,YY}$, versus excitation frequency. Shaft speed 7,500 rpm (150 HZ), seal inlet pressure 44.8 bara, discharge pressure 6.9 bara. Symbols: test data in Ref. [55], Solid line: prediction from NHBFM. Broken line: prediction from HBFM.	59
Figure 14 Real part of cross-coupled complex dynamic stiffness, $Re(H)_{XY,YX}$, versus excitation frequency. Shaft speed 7,500 rpm (150 HZ), seal inlet pressure 44.8 bara, discharge pressure 6.9 bara. Symbols: test data in Ref.[55], Solid line: prediction from NHBFM. Broken line: prediction from HBFM.	60
Figure 15 Imaginary part of complex dynamic stiffness, $Ima(H)_{XX,YY}$, versus excitation frequency. Shaft speed 7,500 rpm (150 HZ), seal inlet pressure 44.8 bara, discharge pressure 6.9 bara. Symbols: test data in Ref.[55], Solid line: prediction from NHBFM. Broken line: prediction from HBFM.	62
Figure 16 Imaginary part of cross-coupled complex dynamic stiffness, $Ima(H)_{XY,YX}$, versus excitation frequency. Shaft speed 7,500 rpm (150 HZ), seal inlet pressure 44.8 bara, discharge pressure 6.9 bara. Symbols: test data in Ref.[55], Solid line: prediction from NHBFM. Broken line: prediction from HBFM.	63
Figure 17 Direct stiffness (K) versus inlet GVF. Shaft speed 7,500 rpm, seal inlet pressure 44.8 bara, discharge pressure 6.9 bara. Symbols: test data in Ref.[55], Solid line: prediction from NHBFM. Broken line: prediction from HBFM.	66
Figure 18 Direct mass (M) versus inlet GVF. Shaft speed 7,500 rpm, seal inlet pressure 44.8 bara, discharge pressure 6.9 bara. Symbols: test data in Ref.[55], Solid line: prediction from NHBFM. Broken line: prediction from HBFM.	67
Figure 19 Cross-coupled stiffness (k) versus inlet GVF. Shaft speed 7,500 rpm, seal inlet pressure 44.8 bara, discharge pressure 6.9 bara. Symbols: test data in	

Ref.[55], Solid line: prediction from NHBFM. Broken line: prediction from HBFM.	68
Figure 20 Direct damping (C) versus inlet GVF. Shaft speed 7,500 rpm, seal inlet pressure 44.8 bara, discharge pressure 6.9 bara. Symbols: test data in Ref.[55], Solid line: prediction from NHBFM. Broken line: prediction from HBFM.	69
Figure 21 Cross-coupled damping (c) versus inlet GVF. Shaft speed 7,500 rpm, seal inlet pressure 44.8 bara, discharge pressure 6.9 bara. Symbols: test data in Ref.[55], Solid line: prediction from NHBFM. Broken line: prediction from HBFM.	70
Figure 22 Whirl frequency ratio (f_w) versus inlet GVF. Shaft speed 7,500 rpm, seal inlet pressure 44.8 bara, discharge pressure 6.9 bara. Symbols: test data in Ref.[55], Solid line: prediction from NHBFM. Broken line: prediction from HBFM.	71
Figure 23 Low pressure seal mass flow rate versus inlet GVF. Shaft speed 3,500 rpm, seal inlet pressure = 2.6 ± 0.1 bara, discharge pressure = 1 bara. Symbols: test data in Ref.[11], Solid line: prediction from NHBFM. Broken line: prediction from HBFM.	73
Figure 24 Complex dynamic stiffnesses (H, h) versus excitation frequency for a low pressure uniform clearance annular seal. Shaft speed 3,500 rpm (58.3 HZ), seal inlet pressure 2.6 ± 0.1 bara, discharge pressure 1 bara. Symbols: test data in Ref.[11], Solid line: prediction from NHBFM. Broken line: prediction from HBFM.	76
Figure 25 Low pressure seal, direct stiffness (K) versus inlet GVF. Shaft speed = 3,500 rpm, seal inlet pressure = 2.6 ± 0.1 bara, discharge pressure = 1 bara. Symbols: test data in Ref.[11], Solid line: prediction from NHBFM. Broken line: prediction from HBFM.	78
Figure 26 Low pressure seal, direct mass (M) versus inlet GVF. Shaft speed 3,500 rpm, seal inlet pressure = 2.6 ± 0.1 bara, discharge pressure = 1 bara. Symbols: test data in Ref.[11], Solid line: prediction from NHBFM. Broken line: prediction from HBFM.	79
Figure 27 Low pressure seal, cross-coupled stiffness (k) versus inlet GVF. Shaft speed = 3,500 rpm, seal inlet pressure = 2.6 ± 0.1 bara, discharge pressure = 1 bara. Symbols: test data in Ref.[11], Solid line: prediction from NHBFM. Broken line: prediction from HBFM.	80

Figure 28 Low pressure seal, direct damping (C) versus inlet GVF. Shaft speed = 3,500 rpm, seal inlet pressure = 2.6 ± 0.1 bara, discharge pressure = 1 bara. Symbols: test data in Ref.[11], Solid line: prediction from NHBFM. Broken line: prediction from HBFM.	81
Figure 29 Low pressure seal, cross-coupled damping (c) versus inlet GVF. Shaft speed = 3,500 rpm, seal inlet pressure = 2.6 ± 0.1 bara, discharge pressure = 1 bara. Symbols: test data in Ref.[11], Solid line: prediction from NHBFM. Broken line: prediction from HBFM.	82
Figure 30 Whirl frequency ratio (f_w) versus inlet GVF. Shaft speed = 3,500 rpm, seal inlet pressure = 2.6 ± 0.1 bara, discharge pressure = 1 bara. Symbols: test data in Ref.[11], Solid line: prediction from NHBFM. Broken line: prediction from HBFM.	83
Figure 31 Control volume showing forces acting on the element [13]	96
Figure 32 Mesh for fluid domain with flow variables P , U_m , W_m and α_g [48].....	107
Figure 33 Control volumes for circumferential and axial velocity (U_m , W_m), pressure (P) and gas volume fraction (α_g).....	108
Figure 34 Control volume for mixture circumferential velocity U_m [48].....	109
Figure 35 Control volume for mixture axial velocity W_m [48].....	110
Figure 36 Control volume for U_m with axial velocity W_m included [48].....	112
Figure 37 Control volume for W_m with circumferential velocity U_m included [48].....	114
Figure 38 Direct stiffness (K) versus inlet GVF. Shaft speed 7,500 rpm, seal inlet pressure 31 bara, discharge pressure 6.9 bara. Symbols: test data in Ref.[55], Solid line: prediction from NHBFM. Broken line: prediction from HBFM. .	120
Figure 39 Added mass (M) versus inlet GVF. Shaft speed 7,500 rpm, seal inlet pressure 31 bara, discharge pressure 6.9 bara. Symbols: test data in Ref.[55], Solid line: prediction from NHBFM. Broken line: prediction from HBFM.....	121
Figure 40 Cross-coupled stiffness (K) versus inlet GVF. Shaft speed 7,500 rpm, seal inlet pressure 31 bara, discharge pressure 6.9 bara. Symbols: test data in Ref.[55], Solid line: prediction from NHBFM. Broken line: prediction from HBFM.	122

Figure 41 Direct damping (C) versus inlet GVF. Shaft speed 7,500 rpm, seal inlet pressure 31 bara, discharge pressure 6.9 bara. Symbols: test data in Ref.[55], Solid line: prediction from NHBFM. Broken line: prediction from HBFM. .123

Figure 42 Cross-coupled damping (c) versus inlet GVF. Shaft speed 7,500 rpm, seal inlet pressure 31 bara, discharge pressure 6.9 bara. Symbols: test data in Ref.[55], Solid line: prediction from NHBFM. Broken line: prediction from HBFM. 124

Figure 43 Whirl frequency ratio (f_w) versus inlet GVF. Shaft speed 7,500 rpm, seal inlet pressure 31 bara, discharge pressure 6.9 bara. Symbols: test data in Ref.[55], Solid line: prediction from NHBFM. Broken line: prediction from HBFM. .125

LIST OF TABLES

	Page
Table 1. Dimensions of test annular seal and fluids physical properties [55].....	47
Table 2. Calculated flow Reynolds number at the inlet and exit planes of test seal in Ref. [55].....	49
Table 3. Dimensions of test uniform clearance annular seal and fluids physical properties [11].....	72
Table 4. Calculated flow Reynolds number at the inlet and exit planes of test seal in Ref. [11].....	74

1. INTRODUCTION

In subsea oil and gas applications, a multiphase pump has to process liquid-gas mixtures with gas volume fraction (GVF) varying from 0 to 100%, and a *wet* gas compressor must process a gas with up to 10% in liquid volume fraction (LVF) [1,2]. Engineering practice shows that gas admission in the suction plane of a multiphase pump not only decreases its total head but also may induce asynchronous rotor vibrations [3,4]. Excessive sub-(or super-) synchronous shaft vibration can trip the machine and cause undesired production loss.

Annular seals, such as impeller eye seals, inter-stage seals and balance pistons, are well known devices that could heavily affect the rotordynamic performance of pump rotor-bearing system as they can generate a significant reaction force acting on the spinning rotor [5]. There are well established bulk flow models (BFM) to predict the leakage and rotordynamic force coefficients of pure liquid annular seals [6,7,8].

To predict the performance of two-phase flow seals, a homogeneous flow assumption is often used and the gas and liquid components are uniformly mixed while sharing the same pressure and velocity fields [9,10]. That is, the mixture is considered as a single phase fluid whose physical properties, such as density and viscosity are either volume fraction averaged or mass fraction weighted. Such model is usually referred as a homogeneous flow model (HBFM).

However, flow visualization tests conducted at a low supply pressure condition [11] reveal that the mixture flowing across a uniform clearance annular seal is not always

homogeneous. In 2014 [11], a seal housing made of Plexiglas allowed visualization of the air-oil mixture flowing through the seal. Figure 1 displays screen shots from videos for the air in oil mixture flowing through the thin film annulus and without shaft rotation. In Ref. [11], the videos are taken with a stroboscope light with frequency = 30 Hz, and are recorded at 60 frames/s. In each video, the mixture enters the seal at the top, and flows downwards to exit the seal clearance at the bottom. The videos show that most of the air bubbles travel separately for operation with inlet GVF < 0.7. Some of the air bubbles coalesce for operation with larger inlet GVFs. Note that although the sparger element makes bubbles 2 μm in size, by the time the mixture reaches the seal, the bubbles are large in size, much larger than the film clearance (c). Figure 2 shows the air-oil mixture with an inlet GVF of 0.9 and operation with shaft angular speed at 1.8 krpm \sim 30 Hz ($R\Omega=12$ m/s). The stroboscope light at 30 Hz freezes the shaft motion. In general, with a spinning shaft, individual gas bubbles vanish. Instead, the bubbles coalesce to form striations or fingering. The remnant air bubbles in the mixture, the ones small in size, mix uniformly with the oil to generate a milky effluent.

Zhang et al. [12] tested uniform clearance annular seals for operation with a mainly air in air-synthetic oil mixture (seal length $L = 57.8$ mm, diameter $D = 89.3$ mm, radial clearance $c_r = 0.140$ mm, 0.163 mm, and 0.188 mm). The test campaign funded by a major oil and gas company aims to investigate the rotordynamic performance of balance piston seals operating with a two component flow condition. The target inlet gas volume fraction for the test is up to 10%, while the max shaft speed is 15 krpm, and the pressure supply and discharge drop (ΔP) is 48.3 bar. Test shows that at a shaft speed of 7,500 rpm and

under some specific inlet GVF operating conditions, the floating housing of the test rig vibrates at a low sub-synchronous frequency, and this sub-synchronous frequency keeps reducing as the inlet GVF increases. The identified seal direct stiffness is negative when the SSV occurs. The authors used a homogeneous bulk flow model (HBFM) to predict the seal force coefficients; however, the model did not predict a negative direct stiffness under the said operating conditions.

The interesting research in Refs.[11] and [12] shows that a homogeneous flow model is not able to accurately predict the rotordynamic performance of an actual two-phase flow annular seal. The flow is not always homogenous, as observed in in the videos in Ref. [11]. Thus, this report aims to develop a nonhomogeneous bulk flow model (NHBFM) to better predict the leakage and rotordynamic performance of two-phase flow annular seals for the advancement of rotor dynamically stable multiphase pumps.

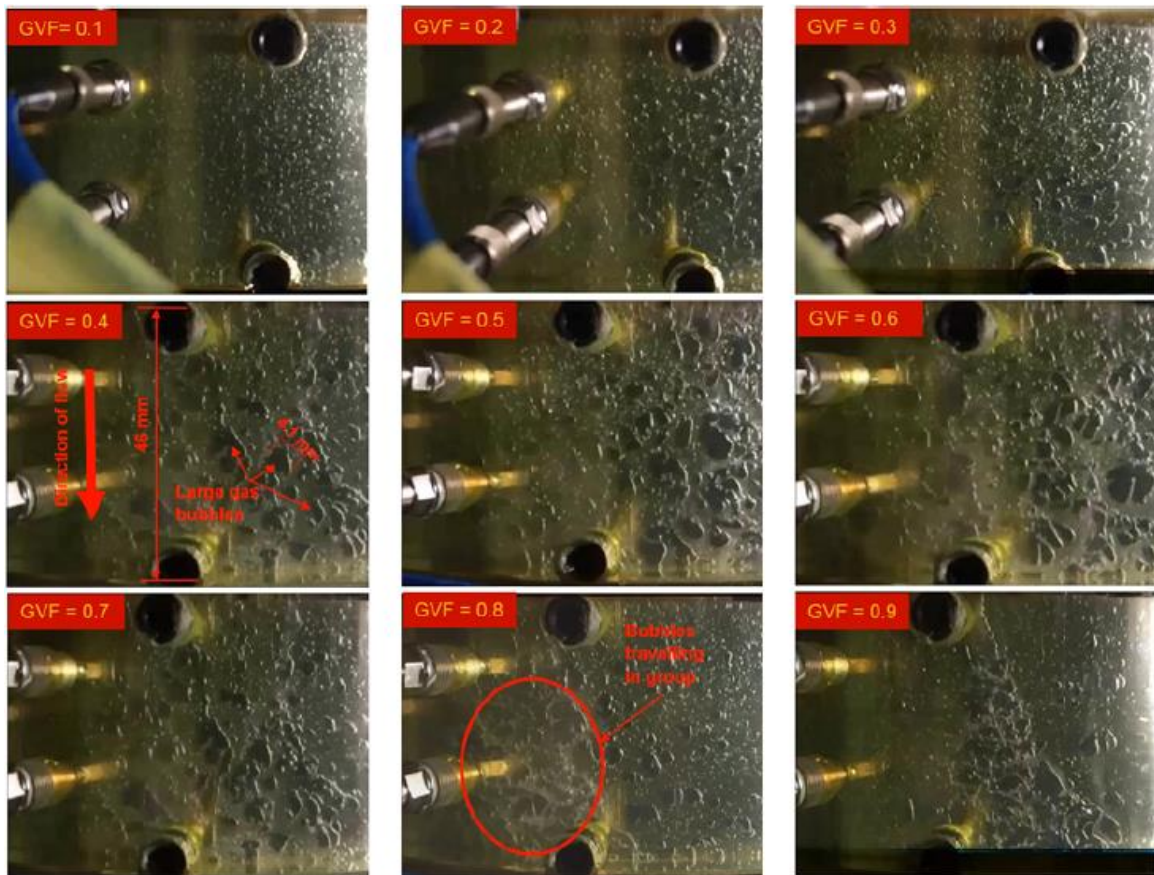


Figure 1 Flow visualization of wet seal operating with a gas and oil mixture. Inlet GVF = 0 to 0.9, journal speed = 0 rpm. Pictures taken with a stroboscope light at 30 Hz. Seal inlet pressure (P_s) = 2.0 bar (a), discharge pressure (P_a) = 1 bara. Picture reproduced from Ref. [11].



Figure 2 Flow visualization of wet seal operating with a gas and oil mixture. Inlet GVF = 0.9, journal speed = 1,800 rpm. Pictures taken with a stroboscope light at 30 Hz. Seal inlet pressure (P_s) = 2.0 bar (a), discharge pressure (P_a) = 1 bara. Picture reproduced from Ref. [11].

2. LITERATURE REVIEW¹

A liquid-gas flow can be produced by a material phase change. For example, when a saturated liquid flows through a seal, liquid vaporization may occur to develop a two-phase flow due to either a drop in fluid pressure or an increase in enthalpy induced by the shear drag force on the surfaces of the seal stator and rotor. There is another type of liquid-gas flow with two distinct materials, such as a mineral oil and air. In both types of two-phase flows, the liquid density (ρ_l) and viscosity (μ_l) are much larger than the physical properties of the gas ρ_g and μ_g ($\rho_l \gg \rho_g$ and $\mu_l \gg \mu_g$). With a two-phase flow, annular seals show different leakage and rotordynamic performance compared to those lubricated with either a pure liquid or a pure gas. The literature review first summarizes the static and dynamic performance of seals operating with a two-phase flow caused by material phase change. Next, a discussion on the characteristics of two-component fluid flow in seals follows.

2.1. Seals operating with two-phase flow caused by material phase change

In 1987, Hendricks [13] tested a nonrotating, uniform clearance cylindrical seal lubricated with liquid nitrogen and hydrogen. The author states that a two-phase flow would develop in the seal when the back (exit) pressure drops, and a reduction in seal leakage and a change in fluid pressure gradient will follow.

¹ Parts of the literature review section are reproduced from prior publications of the author, Refs. [11, 30 – 36]. The author has obtained permission from the publisher (ASME) to reproduce the materials.

Beatty and Hughes [14] (1987) introduce a turbulent flow model to predict leakage in centered smooth surface annular seals operating with an adiabatic two-phase flow. As the fluid flows through the seal, the saturated (or subcooled) liquid changes to vapor. The friction factors in the model, from which wall shear stresses are determined to account for a turbulent flow effect, are chosen from a simple correlation introduced by White [15]. The authors find that the production of a two-phase flow greatly reduces the mass flow rate across the seal.

Beatty and Hughes [16] later (1990) present another model for turbulent two-phase flow in annular seals. The model assumes a fully stratified flow of the boiling liquid and vapor phases. Each phase flows as a separate stream due to a strong centrifugal fluid inertia effect caused by a high shaft speed. Predictions for mass flow rate using the stratified flow model are slightly greater than or equal to the leakage predicted by a homogeneous two-phase flow model.

Arauz and San Andrés [17] (1997) present a bulk flow model (BFM) for a cryogenic fluid damper seal undergoing a phase change, from liquid to vapor. The authors assume a continuous vaporization model. When phase change occurs within the seal, three regions are likely to exist, all liquid, liquid-vapor (a homogeneous mixture), and all vapor. The same authors [18] conclude that the seal will have an increase in direct stiffness and a drop in cross-coupled stiffness due to the large changes in fluid compressibility as it transits from a liquid to a low quality mixture over a short spatial length.

Oike et al. [19] (1999) present experimental results for a floating ring seal working with Nitrogen liquid-vapor mixtures. The observed two-phase flow appears homogeneous

in the tests conducted at a mean temperature $T_0 = 80 \text{ K} \sim 98 \text{ K}$ in the seal upstream plenum, a pressure difference of $\Delta P = 1.25 \text{ MPa}$, and operating at a rotor speed of $0 \sim 40 \text{ krpm}$ ($R\Omega = 83 \text{ m/s}$). The authors study the effect of a two-phase flow area $A_2 (= L_2 / L$, land length under two-phase flow $L_2 /$ seal physical land length L) on the test seal leakage. A_2 increases with shaft rotational speed. Further, the ratio of mass flowrates, \dot{m}_m / \dot{m}_l , with \dot{m}_m as the measured mass flowrate under two-phase flow, also increases as the shaft speed increases. Even for operation at a shaft speed of 40 krpm ($R\Omega = 83 \text{ m/s}$), Oike et al. do not observe a transition from a homogeneous flow to a stratified flow.

Hassini and Arghir [20] (2013) study the effect of material phase change and choked flow on the rotordynamic coefficients of cryogenic liquid annular seals. The authors utilize similar bulk flow equations as those in Ref. [17] but a different method to estimate the speed of sound and to predict choked flow. When lubricated with a pure liquid, the predicted seal direct dynamic complex stiffness reduces parabolically with frequency, i.e., the dynamic stiffness contains an added mass term. When phase change occurs, the dynamic stiffness decreases less in magnitude compared with that of a pure liquid condition. The direct damping coefficient and cross-coupled stiffness show a quick increase due to an increase in mixture viscosity. In addition, phase change can lead to a choked state at the seal exit plane. In such a choked flow, the seal leakage and force coefficients are independent of the downstream (exit) pressure.

2.2. Seals operating with two-phase flow and without phase change

As stated earlier, besides working with a two-phase flow caused by a material phase

change, seals may also operate with a two-component fluid where there is no material transfer between the liquid and gas ($\rho_g \ll \rho_l$ and $\mu_g \ll \mu_l$).

In 1976, Ruud [21] finds a super-synchronous vibration (3 to 7 Hz) in a massive vertical water pump (speed 120 rpm or 2 Hz). During the pump stop process, severe rotor vibrations occurred, persisting even at a near zero shaft speed. The author successfully eliminated the shaft vibration by injecting air to the head covers and to the cavity formed by the outer surface of the blades and the casing. Later in 1996, Smith et al. [22] found a similar shaft vibration issue in a large water pump (speed 300 rpm = 5 Hz) whose natural frequency dropped from 12.5 Hz (dry condition) to 8.8 Hz when filled with water. Injecting air into the cavity behind the impeller removed the super synchronous vibration. The authors in Refs. [21,22] do not provide an explanation on why air injection eliminated the vibration problems. Smith et al. [22] speculates that air injection into the ring cavity “breaks up” pulsation pressures in the seal which stabilizes the pump.

Iwatsubo and Nishino (1993) [23] report force coefficients for a pump seal supplied with an air-water mixture whose gas volume fraction (GVF) varies from 0 (no gas) to 0.70. The seal has diameter $D = 70$ mm, length $L = 70$ mm and radial clearance $c = 0.5$ mm, and operating at a shaft speed of 3,500 rpm (surface speed $\Omega R = 13$ m/s) and under a pressure drop of 588 kPa (85 psi). Both the measured radial and tangential seal reaction forces decrease steadily with an increase in GVF. The authors also report of a shaft random vibration that becomes large in magnitude for operation at GVF = 0.7.

Brunetiere [24] (2014) presents an analysis for a face seal textured with spiral grooves on the low pressure side (inner radius). The inner and outer radii of the seal are filled with

an air-oil mixture with different gas mass fractions. With shaft rotation, the spiral grooves pump the fluid from the low pressure side and compress it, thus forming a high pressure sealing dam. The analysis assumes the mixture is homogeneous and the flow is governed by the classical Reynolds equation. The air is treated as an ideal gas. The gas mass fraction (λ_g) in the film land is derived from the transport equation:

$$\frac{D}{Dt}(\lambda_g) = \dot{m}_x \frac{\partial}{\partial x}(\lambda_g) + \dot{m}_y \frac{\partial}{\partial y}(\lambda_g) + \frac{\partial}{\partial t}(\lambda_g) = 0 \quad (0)$$

where \dot{m}_x and \dot{m}_y are the mass flow rates along the x and y directions, respectively.

San Andrés [10] (2012) develops a bulk-flow model (BFM) to predict the static and dynamic forced performance of textured seals operating with an isothermal homogeneous two-component flow mixture. Predictions show the seal leakage, direct damping and power loss decrease steadily with an increase in inlet GVF. The seal force coefficients also decrease rapidly with excitation frequency if the mixture has a large GVF. Arghir et al. [9] also using a two control volume BFM, predict the rotordynamic force coefficients in a textured annular seal operating with an air in water bubbly flow. The authors note that changes in GVF from 1% to 10% can produce frequency dependent force coefficients.

Voigt et al. [25] detail the design and construction of a large test facility to perform dynamic load tests in annular seals supplied with a wet gas with LVF to 5%, or a bubbly mixture with air content to 5%. The test rig, whose rotor is supported on two active magnetic bearings, can turn up to 10 krpm ($\Omega R=57.6$ m/s) and at a maximum supply pressure of 65 bar.

Voigt et al. [26] (2016) perform computational fluid dynamic (CFD) to predict the rotordynamic force coefficients of a smooth surface annular seal ($L/D = 0.75$) operating with a water in air (wet gas) or air in water (bubbly mixture) mixture. The CFD software solves two sets of continuity and momentum equations for the liquid and air components, respectively. In the model, both fluids (air and water) share the same pressure field, but travel at different speeds. For a wet gas, an increase in LVF to 5% produces an increase in direct stiffness and damping coefficients. For operation with $GVF < 5\%$, the predictions show a dramatic increase in direct damping with frequency and no added mass effect.

Ekeberg et al. [4] (2018) report the engineering and testing of a multiphase pump for boosting multiphase hydrocarbon mixtures with a liquid viscosity as large as 800 centipoise. The pump operates smoothly for most of operating conditions. However, while operating over a narrow range of shaft speeds, 3.5 krpm to 4.0 krpm, and while pumping a mixture with liquid viscosity 300 cp and $GVF=0.6$ at the pump suction plane, with differential pressure of ~ 40 bar, the pump experiences a sudden increase in shaft super-synchronous vibrations (1.07X~1.44 X). The super-synchronous vibration evolves into a sub-synchronous vibration when the pump inlet GVF is lowered. The original design of the pump utilizes a balance piston (a uniform clearance annular seal) with a length/diameter (L/D) ratio of 0.2 to reduce the axial load acting on the thrust bearing. Computational fluid dynamic (CFD) analysis in Ref [4] shows that the 300 cp liquid viscosity and 60 % GVF at the pump suction plane corresponds to a 200 cp liquid viscosity and 40% GVF condition at the seal inlet plane.

To solve the asynchronous shaft vibration issue, Ekeberg et al. [4] conduct a CFD

study on the balance piston seal. The authors find that under a 200 cp liquid viscosity and 40% GVF at the seal inlet plane condition the flow in the seal is not homogeneous. Along the seal circumferential direction there exists several high velocity flow fields stretching from inlet to outlet and which are occupied by almost pure gas. Between the high velocity sectors, there are liquid hold-up regimes with low axial velocity. In such a condition the authors find a negative direct stiffness.

Li et al. [27] conduct a computational fluid dynamics (CFD) study using the seal geometry and operating conditions in Ref. [12] to deliver predictions for various seal types: smooth surface annular seal, labyrinth seal with teeth on stator, and a pocket damper seal. Li et al. show modest agreement when validating their model predictions against the test results in Ref. [12]. For operation with a pressure difference of 32 bar and at a shaft speed equal to 15 krpm ($\Omega R=70$ m/s), both predicted direct stiffness (negative) and the effective damping of the labyrinth seal decrease as the inlet LVF increases from 0 to 8%. On the contrary, the pocket damper seal offers an increase in both direct stiffness (positive) and effective damping with an increase in the inlet LVF.

In a recent analytical research (2019), Grimaldi et al. [28] present a novel stratified two-phase bulk flow model to predict the leakage in annular seals. The stratified flow model considers the two-phases do not mix and move independently. The liquid being attached to the stator surface moves slowly as if in a laminar flow regime; whereas the gas is dragged by the rotor, and due to its low kinematic viscosity, flows as a turbulent core. The model computes the bulk flow shear stress using Hirs formulation [6]. The authors find that the predicted leakage matches better to test data [55] than the leakage calculated

with a homogeneous bulk flow model [10]. However, the authors had to adjust the exit pressure loss coefficient as the operating condition varies. The paper does not present seal dynamic force coefficients.

2.3. Summary of research on two-phase flow seals since 2010 in the Turbomachinery Laboratory of Texas A&M University

To solve the pressing needs toward quantifying the static and dynamic performance of two-phase flow annular seals in multiphase pumps, since 2010 the Turbomachinery Laboratory at Texas A&M University has launched a series of research projects to quantify the effect of gas admission on the leakage and rotordynamic force coefficients of two-phase flow seals. The fundamental work by San Andrés in 2012 [10] produced a homogeneous bulk flow model (HBFM). Simultaneously the laboratory started test campaigns to investigate experimentally two-phase flow annular seals.

San Andrés et al. [11] (2016) present measurements conducted in a short length ($L/D=0.36$) uniform clearance annular seal supplied with an air in oil (ISO VG10) mixture. In tests with a stationary journal and operating with a pressure supply/pressure discharge ratio=2.0, a mixture with LVF=2% and 4% increases ten-fold (or more) the damping coefficients compared with that of a dry gas seal. For operation with a spinning journal with angular speed (Ω) 3.5 krpm ($\Omega R=23.3$ m/s), and a supply pressure 2.5 bara, the leakage and drag power decrease monotonically by 25% and 85% respectively as the mixture inlet GVF increases from 0 (pure oil) to 0.9 [11] (2018). The seal with a pure liquid produces frequency independent force coefficients (K , C , M). For tests with a

mixture ($GVF_{\max}=0.9$), the seal direct dynamic stiffness (K) increases with whirl frequency. Both the seal cross-coupled stiffness (k) and direct damping (C) decrease $\sim 75\%$ as the inlet GVF increases to 0.9. The tests also reveal the appearance of a self-excited seal motion with a low frequency; an acoustic resonance whose amplitude and broad band frequency (centered at around ~ 12 Hz) persist and increase as the gas content increases.

San Andrés et al. [30-34] (2018, 2019) detail measurements of leakage and force coefficients obtained from six annular seals operating with an air in ISO VG10 oil. Each seal has a distinct clearance configuration: one is a plain seal with a small clearance ($c=0.203$ mm), and another has a larger (worn) clearance ($c=0.274$ mm); a third seal introduces a wavy clearance ($c_m= 0.191$ mm) that produces a significant centering stiffness; a fourth seal has a shallow groove pattern ($c_r=0.211$); and the fifth and sixth seals have a stepped clearance (narrow to wide and wide to narrow). The seals operate in the laminar flow region, except for the pure gas seal. For operation with a pure oil, the wavy seal shows slightly more leakage (mass flow rate) compared with the small clearance plain seal. The step clearance seal with the tightest clearance near the exit plane leaks the least. The grooved seal leaks more than the plain seals as the flow regime is laminar. For operation with oil only ($GVF=0$), the six seals show frequency independent force coefficients. The three-wave seal shows a greater direct stiffness (K) compared with that of the two uniform clearance seals and the grooved seal. The upstream step clearance seal shows $K < 0$ that increases in magnitude with supply pressure; and the downstream step clearance seal show exactly the opposite effect, $K > 0$. For operation with an air in oil mixture, the six seals produce frequency dependent force coefficients. The three-wave seal

shows the largest dynamic stiffnesses (direct and cross-coupled) and effective damping coefficient. The wavy seal *hardens* with frequency for operation with GVF as large as 0.9. The dynamic stiffness reduces with frequency quickly for the other seals. The injection of gas into the upstream step clearance seal hardens its dynamic stiffness; the effect is more pronounced as the frequency of excitation increases. For the uniform clearance seal and the three wave seal, the exiting bulk flow model predicts well the leakage and dynamic force coefficients for operation with pure oil and mixtures with a small gas content. The discrepancy between prediction and test data grows as the gas content increases, $\text{GVF} > 0.2$.

Yang et al. [35] (2019) utilize commercial CFD software to study the flow field, leakage, and force coefficients of a uniform clearance annular seal detailed in Ref. [11]. The CFD package solves two sets of continuity and momentum equations for the flow of air and oil. Using a $1 \mu\text{m}$ air bubble size ($\frac{1}{200} c$, $c=0.203 \text{ mm}$), the authors predict leakage and drag power that agrees with the test data. Both the CFD and test data show that a 20% (or less) of air volume fraction in the oil can cause a hardening effect in the seal direct stiffness versus frequency. Because of the (assumed) minute bubble size, the predicted air axial velocity equals to the oil axial velocity even though a nonhomogeneous two-fluid model is used in the CFD software.

In a later research, Yang et al. [36] (2019) conduct CFD and experimental study on the leakage and dynamic force coefficient of a pocket damper seal (PDS) operating under a wet gas condition. The test seal, operating at a speed of 5,250 rpm (surface speed of 35 m/s) is supplied with a controlled mixture of light oil in air delivered at a pressure up to

3.2 times ambient. The maximum inlet liquid volume fraction (LVF) is 2.2% that corresponds to an 84% mass content. The research results show that the ridges in a pocket limit the development of the circumferential flow speed while reducing the liquid content in the middle of a pocket. Under a wet gas condition, the PDS produces more damping compared to that for a dry gas condition. The findings agree with the conclusion made by Vannini et al [37], that a PDS can stabilize an otherwise unstable compressor (installed with labyrinth seal as balance piston) under a wet gas condition.

In a companion project, Childs and students conduct a series of tests on seals operating with an air-synthetic oil mixture. Zhang et al. [38] (2017) present test results for leakage and force coefficients for a long, smooth surface annular seal ($D = 89.3$ mm, $L/D = 0.65$, and $c = 0.188$ mm) operating with a silicon oil (PSF-5cSt) in air mixture with LVF $\leq 8\%$, at a supply pressure of 62.1 bar and at a top shaft speed 20 krpm ($\Omega R = 93.5$ m/s). The authors report $\sim 5\%$ decrease in mass flow rate as the LVF increases from 0 to 2%, which later increases by $\sim 50\%$ as the LVF further increases to 8%. For operation with discharge pressure/supply pressure ratios = 0.5 and 0.57 and at a shaft speed from 10 krpm to 20 krpm, the seal direct dynamic stiffness (K) decreases continuously as the inlet LVF increases from 0 to 8%. The cross-coupled stiffnesses (k) increase two to three times, depending on shaft speed. When lubricated with either a pure air or with a mixture, both K and k increase with excitation frequency. The tests show frequency independent direct (C) and cross-coupled damping coefficients (c) for operation with either a pure air or a mixture. An increase in the inlet LVF from 0 to 2% causes a quick increase in the cross-

over frequency where the effective damping coefficient is zero. However, a further increase in LVF from 2% to 8% reduces the cross-over frequency again.

Later Zhang et al. [12] (2018) include work pertinent to multiphase pumps. As described earlier, gas admission in the suction plane of an annular seal could generate a significant negative direct stiffness that may cause self-excited asynchronous vibration to the rotor. Tran et al. [39] (2019) extend the tests in Ref. [12] to include the effect of preswirl on the seal' force coefficients. The test seal has seal length $L = 85.725$ mm, diameter $D = 114.68$ mm, and radial clearance $c = 0.200$ mm. The max rotor speed is 5 krpm ($R\Omega = 30$ m/s) and the pressure drop is up to 41.4 bar with an exit pressure of 6.9 bar. The authors find out that as the inlet GVF increases the direct stiffness of the seal drops quickly from ~ 20 MN/m to negative for operation with a high pre-swirl condition. However, as the inlet increasing of the inlet GVF, the cross-coupled stiffness does not vary, while the direct damping coefficient actually increases. The authors claim the mixture is inhomogeneous at some operating conditions. However, no evidence is provided.

Comprehensive tests in the literature demonstrate that the HBFM detailed in Ref. [10] offers good predictions on the static and dynamic performance of annular seals lubricated by single phase flows, either a pure liquid (GVF=0), or a pure gas (LVF=0). However, experiments also show that the flow in the seal may not be homogeneous under some specific operating conditions [4, 11, 12]. Indeed, the discrepancy between test results and predictions for the dynamic force coefficients grows as the inlet gas volume fraction increases.

The desire to produce more accurate predictions for two-phase flow seals points to the necessity of advancing a model considering the effect of the velocity difference between the gas and liquid components.

3. THE NONHOMOGENEOUS BULK FLOW MODEL

3.1. Selection of a two-phase (component) flow model

Figure 3 shows a fluid domain and a control volume filled with liquid and dispersed spherical gas bubbles. The domain has a width A and length B along the circumferential (X), and axial (Z) directions, respectively. The depth (gap) of the domain is H ($H \ll A$ and $H \ll B$) along the Y direction (normal to X - Z plane); this feature is akin to a seal clearance whose film thickness is far smaller than its axial length and circumference. In the control volume, the gas volume fraction (α_g) is

$$\alpha_g = \frac{q_g}{q_g + q_l} \quad (1)$$

where q_g and q_l are the volume occupied by gas and liquid in the control volume. Accordingly, the liquid volume fraction is

$$\alpha_l = 1 - \alpha_g \quad (2)$$

The gas mass fraction (λ_g) is defined as

$$\lambda_g = \frac{\alpha_g \rho_g}{\alpha_g \rho_g + \alpha_l \rho_l} \quad (3)$$

where ρ_g and ρ_l are the density for the gas and liquid. In Figure 3, U_g , U_l , and W_g , W_l are the gas and liquid velocities flowing through the faces of the control volume along the X and Z directions, respectively.

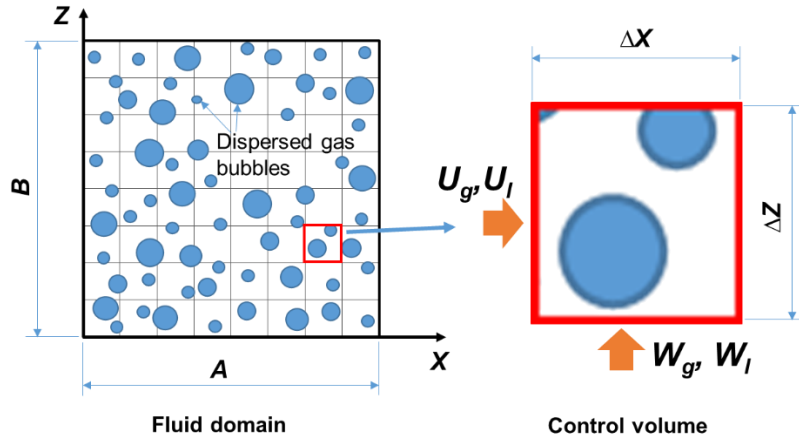


Figure 3 A fluid domain and a control volume filled with liquid and dispersed gas bubbles [40].

In the modeling for a two-phase (component) flow, Ishii and Hibiki [41] introduce a two-fluid model which offers a complete insight into the flow variables. The model contains two sets of separate conservation equations governing the mass, momentum and energy transport for each phase (or component). Additional interaction terms couple the momentum equations of the two components.

In the two-fluid model [41], the mass conservation law for the two components is

$$\frac{D}{Dt}(\dot{m}_k) = 0 \Rightarrow \frac{\partial}{\partial t}(\alpha_k \rho_k) + \nabla \cdot (\alpha_k \rho_k \mathbf{U}_k) = \Gamma_k = 0, \quad k = g, l \quad (4)$$

where \dot{m}_k is the mass flow rate of component k , $\mathbf{U}_k = U_k \vec{i} + V_k \vec{j} + W_k \vec{k}$ is the component fluid velocity vector, and $\nabla = \frac{\partial}{\partial x} \vec{i} + \frac{\partial}{\partial y} \vec{j} + \frac{\partial}{\partial z} \vec{k}$ is the gradient operator. Γ_k denotes the

mass transfer at the interface of the liquid and the gas components. Since in the current research there is no mass transfer between the two components

$$\Gamma_k = 0, k = g, l \quad (5)$$

The transport of momentum equation for each component is:

$$\frac{\partial}{\partial t}(\alpha_k \rho_k \mathbf{U}_k) + \nabla \cdot (\alpha_k \rho_k \mathbf{U}_k \mathbf{U}_k) = -\alpha_k \nabla p_k + \nabla \cdot [\alpha_k (\boldsymbol{\tau}_k + \boldsymbol{\tau}_{Tk})] + \alpha_k \rho_k \mathbf{g} + \mathbf{M}_k, k = g, l \quad (6)$$

where p_k is the pressure in phase k , $\boldsymbol{\tau}_k$ is the average viscous stress tensor, $\boldsymbol{\tau}_{Tk}$ is the turbulent stress tensor, \mathbf{g} is the gravitational acceleration, and \mathbf{M}_k is the average interfacial momentum source for phase k , and $\mathbf{M}_g = -\mathbf{M}_l$.

In seals lubricated with a two-component flow without material phase change, the fluids can be regarded as isothermal due to their high axial velocities, which immediately take away the heat generated by surface's shear drag. Thus, energy transport equations are not required.

The two-fluid model (liquid and gas) detailed above contains eight (2x4) equations: two mass conservation equations and six momentum transport equations along the X , Y and Z directions. Ishii and Hibiki [41] point out that if one is concerned with the total response of the two-phase mixture in a system, rather than the local behavior of each phase, the algebraic slip mixture model² (ASMM) is simpler and more effective for solving problems.

Damian [40] discussed the applicability of the Algebraic slip mixture model (ASMM) as well as the volume of fluid model (VOF). Both models are simplified versions of the

² The algebraic slip mixture model (ASMM) is a simplified version of the two-fluid model, and which considers the mixture as a whole with a mean density and viscosity. The relative velocity between the gas and the mixture is found analytically, as discussed in detail in Appendix B.

two-fluid model. The VOF model, advanced by Hirt and Nichols [42] (1981), can track the long scale interface (see Fig. 2a) between the gas and liquid components where the two fluids are not interpenetrating. If the two fluids are mixed together (see Figure 4 b), the ASMM model by Manninen et al. [43] (1996) is more suitable than the VOF method. Flow visualization test [29] shows that the distribution of the gas content in the seal is similar to that shown in Figure 4b. Thus, the ASMM model is suitable for the seal analysis.

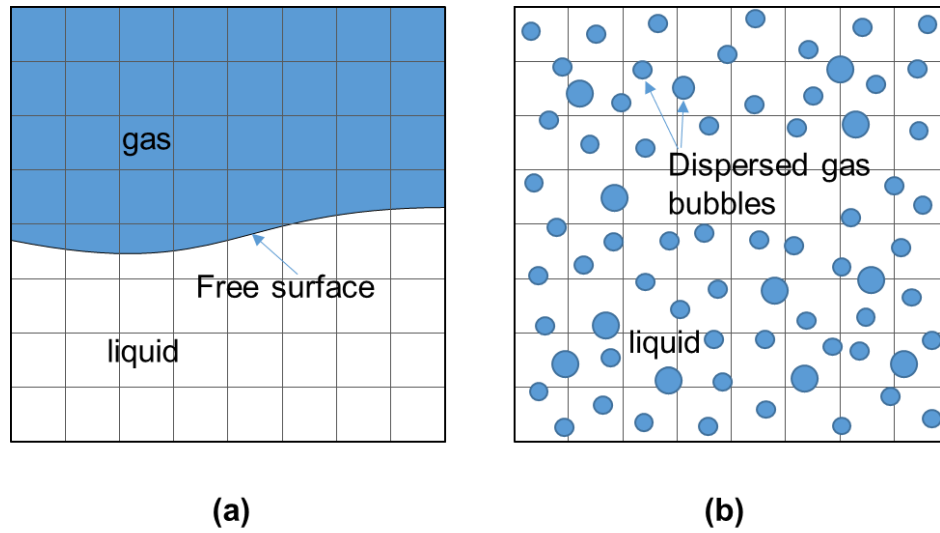


Figure 4 Short and long geometric scales in a bubbly flow (a) long scale interfaces, (b) short scale interfaces [40].

Recall that the algebraic slip mixture model (ASMM) considers the mixture as a whole, rather than two separate components [43]. Thus, adding the continuity equations for the gas and liquid in Eq. (4) makes

$$\frac{\partial}{\partial t} \rho_m + \nabla \cdot (\rho_m \mathbf{U}_m) = 0 \quad (7)$$

where \mathbf{U}_m is the velocity vector of the mixture mass center defined as

$$\mathbf{U}_m = \frac{1}{\rho_m} (\alpha_g \rho_g \mathbf{U}_g + \alpha_l \rho_l \mathbf{U}_l) \quad (8)$$

and ρ_m is the mixture density

$$\rho_m = \alpha_l \rho_l + \alpha_g \rho_g \quad (9)$$

Summing over the momentum equation of the two-phases in Eq. (6) leads to

$$\begin{aligned} & \frac{\partial}{\partial t} \sum_{k=1}^2 (\alpha_k \rho_k \mathbf{U}_k) + \nabla \cdot \sum_{k=1}^2 (\alpha_k \rho_k \mathbf{U}_k \mathbf{U}_k) \\ &= - \sum_{k=1}^2 (\alpha_k \nabla p_k) + \nabla \cdot \sum_{k=1}^2 \alpha_k (\boldsymbol{\tau}_k + \boldsymbol{\tau}_{Tk}) + \sum_{k=1}^2 (\alpha_k \rho_k \mathbf{g}) \end{aligned} \quad (10)$$

where $\boldsymbol{\tau}_k$ and $\boldsymbol{\tau}_{Tk}$ are the viscous and turbulent stress tensors. Note that the interfacial momentum disappears because the interfacial momentum forces $\mathbf{M}_g = -\mathbf{M}_l$.

Ref. [43] show that the second term in Eq. (10) can be written as:

$$\nabla \cdot \sum_{k=1}^2 (\alpha_k \rho_k \mathbf{U}_k \mathbf{U}_k) = \nabla \cdot (\rho_m \mathbf{U}_m \mathbf{U}_m) + \nabla \cdot \sum_{k=1}^2 (\alpha_k \rho_k \mathbf{U}_{dr,k} \mathbf{U}_{dr,k}) \quad (11)$$

where $\mathbf{U}_{dr,k}$ is the velocity of phase k relative to the mass center of the mixture

$$\mathbf{U}_{dr,k} = \mathbf{U}_k - \mathbf{U}_m \quad (12)$$

Substituting Eq. (11) back into Eq. (10) leads to the complete momentum equation for the mixture

$$\frac{\partial}{\partial t} (\rho_m \mathbf{U}_m) + \nabla \cdot (\rho_m \mathbf{U}_m \mathbf{U}_m) + \nabla \cdot \sum_{k=1}^2 (\alpha_k \rho_k \mathbf{U}_{dr,k} \mathbf{U}_{dr,k}) = -\nabla p_m + \nabla \cdot (\boldsymbol{\tau}_m + \boldsymbol{\tau}_{Tm}) + \rho_m \mathbf{g} \quad (13)$$

As discussed above, the algebraic slip mixture model (ASMM) consists of only four governing equations (one continuity equation and three momentum equations along the X ,

Y and Z directions), and which is much simpler than the two-fluid model that contains eight balance equations.

A prerequisite to applying the ASMM is that the system is in local equilibrium state [43]. That is, in a bubbly mixture the air bubble relaxation time (τ_g) is small compared to the system characteristic time, i.e., the external excitation period (T_ω). τ_g equals

$$\tau_g = \frac{\rho_g d_g^2}{18\mu_l} < T_\omega \quad (14)$$

where d_g is the diameter of an gas bubble.

In Ref. [29], the liquid viscosity $\mu_l = 10.6$ cP, $\rho_g = 1.14$ kg/m³. Assuming a bubble size $d_g = 0.2$ mm (the size of the seal clearance), the relaxation time³ is $\tau_g = 2.4 \times 10^{-7}$ s. For a system with an excitation frequency of 200 Hz, the period is $T_\omega = 1/200$ s = 5×10^{-3} s $\gg \tau_g$. Thus, the local equilibrium state condition is satisfied, and the algebraic slip mixture model (ASMM) is applicable for seal analysis.

In a gas in liquid mixture for multiphase pump application, the liquid is the continuous phase and the gas is a dispersed phase. In the ASMM theory, the gas volume fraction can be calculated through the gas continuity equation.

$$\frac{\partial}{\partial t}(\alpha_g \rho_g) + \nabla \cdot (\alpha_g \rho_g \mathbf{U}_g) = 0 \quad (15)$$

Substituting the gas diffusion velocity into Eq. (15) obtains the following equation:

³ The relaxation time is the time required for a gas bubble to change from one equilibrium state to the other equilibrium state. At an equilibrium state, the viscos drag force applied by the liquid to a gas bubble equals to the force caused by the density difference between the mixture and the gas, see Eq. (B-2) in Appendix B.

$$\frac{\partial}{\partial t}(\alpha_g \rho_g) + \nabla \cdot (\alpha_g \rho_g \mathbf{U}_m) = -\nabla \cdot (\alpha_g \rho_g \mathbf{U}_{dr,g}) \quad (16)$$

The right hand side of Eq. (16) equals zero if the flow is homogeneous.

3.2. Applying the ASMM to the flow in air-oil in annular seals

Since 1996 many commercial CFD packages have included the ASMM model to simulate multiphase flows [43]. The commercial CFD solvers are quite time consuming as they require to divide the fluid domain into millions of sub-elements to deliver accurate results. In seals, the fluid film thickness (H , normal to X , Y directions) is much smaller than the radius ($H/R \ll 1$) and axial length ($H/L \ll 1$). Thus, enabling the spatial average of the flow variables across the film thickness.

In the proposed model for the gas-liquid mixture, bulk flow volume fraction ($\bar{\alpha}$), density ($\bar{\rho}$) and velocity components (\bar{U} , \bar{W}) are averaged across the film thickness (H). That is,

$$\bar{\alpha}_k = \frac{1}{H} \int_0^H \alpha_k dy, \quad k = g, l \quad (17)$$

$$\bar{\rho}_k = \frac{1}{H} \int_0^H \rho_k dy, \quad k = g, l \quad (18)$$

$$\bar{U}_k = \frac{1}{H} \int_0^H U_k dy, \quad \bar{W}_k = \frac{1}{H} \int_0^H W_k dy, \quad k = g, l \quad (19)$$

above $k = g, l$ stands for gas and liquid respectively; the liquid density (ρ_l) does not change with pressure because the fluid is considered as incompressible. The air is treated as an ideal gas, and thus its density is

$$\rho_g = P / (Z_g R_g T) \quad (20)$$

above $Z_g = 1$ is the compressibility factor for an ideal gas flow at a low Mach number; R_g is the gas constant, P is the absolute pressure, and T is the absolute temperature.

The velocity components of the mixture along the circumferential (X) and axial (Z) directions are defined as⁴

$$\begin{aligned} \bar{U}_m &= \frac{1}{\bar{\rho}_m} (\bar{\alpha}_g \bar{\rho}_g \bar{U}_g + \bar{\alpha}_l \bar{\rho}_l \bar{U}_l) \\ \bar{W}_m &= \frac{1}{\bar{\rho}_m} (\bar{\alpha}_g \bar{\rho}_g \bar{W}_g + \bar{\alpha}_l \bar{\rho}_l \bar{W}_l) \end{aligned} \quad (21)$$

where $\bar{\rho}_m = \bar{\alpha}_g \bar{\rho}_g + \bar{\alpha}_l \bar{\rho}_l$ is the mixture average density. Note Eq. (19) \neq Eq. (21).

For a mixture with liquid as the continuous phase and air as the dispersed phase, the diffusion bulk flow velocities for the gas are

$$\begin{aligned} \bar{U}_{dr,g} &= \bar{U}_g - \bar{U}_m \\ \bar{W}_{dr,g} &= \bar{W}_g - \bar{W}_m \end{aligned} \quad (22)$$

3.3. The bulk flow equations for a two-component mixture in annular seals

Applying Eq. (7) on a control volume shown in Figure A-1, the bulk flow mass conservation equation is:

$$0 = \frac{\partial}{\partial t} (\bar{\rho}_m H) + \frac{\partial}{\partial x} (\bar{\rho}_m \bar{U}_m H) + \frac{\partial}{\partial z} (\bar{\rho}_m \bar{W}_m H) \quad (23)$$

⁴ Please note $\bar{\alpha}_g \bar{\rho}_g \neq \overline{\alpha_g \rho_g}$. The current model is approximate only.

The momentum equations are similar to those in a homogeneous flow BFM model [10], except that the nonhomogeneous flow BFM includes additional terms to include the influence of the diffusion velocity between the primary and secondary phases. Appendix A details the process to derive the momentum equations.

The bulk flow momentum transport equations along the circumferential (X) and axial (Z) directions are:

$$\frac{\partial}{\partial t}(\bar{\rho}_m \bar{U}_m H) + \frac{\partial}{\partial x}(\bar{\rho}_m \bar{U}_m^2 H (1+r_1)) + \frac{\partial}{\partial z}(\bar{\rho}_m \bar{U}_m \bar{W}_m H (1+r_2)) = -H \frac{\partial P}{\partial x} - \tau_{xy} \Big|_0^H \quad (24)$$

$$\frac{\partial}{\partial t}(\bar{\rho}_m \bar{W}_m H) + \frac{\partial}{\partial x}(\bar{\rho}_m \bar{U}_m \bar{W}_m H (1+r_3)) + \frac{\partial}{\partial z}(\bar{\rho}_m \bar{W}_m^2 H (1+r_4)) = -H \frac{\partial P}{\partial z} - \tau_{zy} \Big|_0^H \quad (25)$$

where the coefficients r_1 to r_4 are determined by the component's volume fractions, their density, and diffusion velocity⁵:

$$r_1 = \frac{\bar{\alpha}_g \bar{\rho}_g \bar{U}_{dr,g}^2}{\bar{\rho}_m \bar{U}_m^2} \quad (26)$$

$$r_2 = r_3 = \frac{\bar{\alpha}_g \bar{\rho}_g \bar{U}_{dr,g} \bar{W}_{dr,g}}{\bar{\rho}_m \bar{U}_m \bar{W}_m} \quad (27)$$

$$r_4 = \frac{\bar{\alpha}_g \bar{\rho}_g \bar{W}_{dr,g}^2}{\bar{\rho}_m \bar{W}_m^2} \quad (28)$$

Note set $r_1=r_2=r_3=r_4=0$ to simplify the nonhomogeneous flow model to a homogeneous flow model. Ref. [43] details a method to solve for the diffusion velocity of the secondary

⁵ Appendix B details the solution process for $U_{dr,g}$ and $U_{dr,l}$.

phase through balancing the body force of the gas phase with the drag force. The drag force is of viscous type and applies to both the liquid and gas at their interfaces.

In Eqs. (24) and (25), $\tau_x|_0^H$ and $\tau_z|_0^H$ represent the wall shear stress differences (rotor-stator) along the X and Z directions, respectively. In a single phase flow (pure liquid or pure air), Hirs' Bulk flow theory [6] characterizes well the wall shear stresses.

Salhi et al. [44] conducted tests to measure the pressure gradient in concentric cylinders supplied with a mixture of liquid (oil) and nitrogen (gas, 5% in volume fraction). The authors show that the Hirs' correlation $f = a Re^n$ (see the next paragraph) is valid for a two-phase flow with a low gas volume fraction ($\alpha_g \leq 5\%$). Thus, to begin with, the proposed nonhomogeneous model uses Hirs' method in Ref. [6] to calculate the wall shear stress differences:

$$\tau_x|_0^H = \frac{\mu_m}{H} \left(k_x \bar{U}_m - k_r \frac{\Omega R}{2} \right) \quad (29)$$

$$\tau_z|_0^H = \frac{\mu_m}{H} k_z \bar{W}_m \quad (30)$$

For a laminar flow the parameters $k_x = k_z = k_r = 12$; and for a turbulent flow $k_x = k_z = 1/2 (k_r + k_s)$. The shear parameters on the rotor and stator surfaces are $k_r = f_r Re_{mr}$, $k_s = f_s Re_{ms}$, respectively. Above the turbulent friction factors f_r and f_s are determined from Moody's

formulas [20]⁶. The mixture flow Reynolds numbers relative to the stator and rotor surfaces are

$$\text{Re}_{ms} = \frac{\rho_m H}{\mu_m} (\bar{U}_m^2 + \bar{W}_m^2)^{0.5} \quad (31)$$

$$\text{Re}_{mr} = \frac{\rho_m H}{\mu_m} ((\bar{U}_m - \Omega R)^2 + \bar{W}_m^2)^{0.5} \quad (32)$$

Awad and Muzychka [46] show that there are more than 20 equations to compute the viscosity of a two-phase flow. Each equation is suitable for a specific application. Based on predictions for leakage compared to test data, the current work selects two formulas to evaluate the effective viscosity (μ_m), one is gas volume fraction averaged and given in Eq.(33a) [47], and the other is gas mass fraction weighted and given in Eq. (33b) [48].

$$\bar{\mu}_m = \bar{\alpha}_g \bar{\mu}_g + (1 - \bar{\alpha}_g) \bar{\mu}_l + 2\sqrt{\bar{\alpha}_g (1 - \bar{\alpha}_g) \bar{\mu}_g \bar{\mu}_l} \quad (33a)$$

$$\bar{\mu}_m = \bar{\lambda}_g \bar{\mu}_g + (1 - \bar{\lambda}_g) \bar{\mu}_l \quad (33b)$$

Next, applying Eq. (16) to the control volume shown in Figure A-1, the gas volume fraction is calculated from:

$$\begin{aligned} & \frac{\partial}{\partial t} (\bar{\alpha}_g \bar{\rho}_g H) + \frac{\partial}{\partial x} (\bar{\alpha}_g \bar{\rho}_g \bar{U}_m H) + \frac{\partial}{\partial z} (\bar{\alpha}_g \bar{\rho}_g \bar{W}_m H) \\ & = -\frac{\partial}{\partial x} (\bar{\alpha}_g \bar{\rho}_g \bar{U}_{dr,g} H) - \frac{\partial}{\partial z} (\bar{\alpha}_g \bar{\rho}_g \bar{W}_{dr,g} H) \end{aligned} \quad (34)$$

If the flow is homogeneous, $\bar{U}_{dr,g} = \bar{W}_{dr,g} = 0$, then Eq. (34) reduces to

⁶ $f_{r,s} = a_m [1 + (c_m r_{r,s}/H + b_m/\text{Re}_{r,s})^e]$ is Moody's friction factor at the rotor (r) and stator (s) surfaces; $a_m=0.001375$, $b_m=5 \times 10^5$; $c_m=10^4$; $e=1/3$; and r_r and r_s are the roughness of the rotor and stator surfaces, respectively [40].

$$\frac{\partial}{\partial t}(\bar{\alpha}_g \bar{\rho}_g H) + \frac{\partial}{\partial x}(\bar{\alpha}_g \bar{\rho}_g \bar{U}_m H) + \frac{\partial}{\partial z}(\bar{\alpha}_g \bar{\rho}_g \bar{W}_m H) = 0 \quad (35)$$

At a steady state, for an annular seal operating in a centered condition, the first and second terms in Eq. (35) vanish. The film thickness $H = c$, where c is a radial clearance. The simplified equation (35) actually shows the air mass flow rate (\dot{m}_g) is constant along the axial direction

$$\bar{\alpha}_{g(z)} \bar{\rho}_{g(z)} \bar{W}_{m(z)} c = \bar{\alpha}_g^s \bar{\rho}_g^s \bar{W}_m^s c = \dot{m}_g \quad (36)$$

where $\bar{\rho}_g^s, \bar{\rho}_{g(z)}$ and $\bar{W}_m^s, \bar{W}_{m(z)}$ are the gas density and the mixture axial velocity at the supply condition and at the axial location Z , respectively. Hence, the air volume fraction $\bar{\alpha}_{g(z)}$ at a specific axial location Z satisfies the following relation

$$\bar{\alpha}_{g(z)} = \bar{\alpha}_g^s \frac{\bar{\rho}_g^s}{\bar{\rho}_{g(z)}} \frac{\bar{W}_m^s}{\bar{W}_{m(z)}} \quad (37)$$

Since the air density (ρ_g) is proportional to pressure (P), Eq. (37) can be rewritten as

$$\bar{\alpha}_{g(z)} = \bar{\alpha}_g^s \frac{P_s}{P_{(z)}} \frac{\bar{W}_m^s}{\bar{W}_{m(z)}} \quad (38)$$

where $P_{(z)}$ is the local pressure. In Eq. (38), the ratio of bulk flow axial velocities ($\frac{\bar{W}_m^s}{\bar{W}_{m(z)}}$)

comes from:

$$\frac{\bar{W}_m^s}{\bar{W}_{m(z)}} = \frac{(Q_g^s + Q_l) / A}{\left(Q_g^s \frac{P_s}{P_{(z)}} + Q_l \right) / A} = \frac{(Q_g^s + Q_l)}{\left(Q_g^s \frac{P_s}{P_{(z)}} + Q_l \right)} \quad (39)$$

where Q_g^s and Q_l are the air and oil supply volumetric flow rate, and $A = (\pi Dc)$ is the cross-section flow area. Combining Eqs. (38) and (39) gives:

$$\begin{aligned}\bar{\alpha}_{g(z)} &= \bar{\alpha}_g^s \frac{P_s}{P_{(z)}} \frac{(Q_g^s + Q_l)}{\left(Q_g^s \frac{P_s}{P_{(z)}} + Q_l\right)} \Rightarrow \bar{\alpha}_{g(z)} = \bar{\alpha}_g^s \frac{P_s}{P_{(z)}} \frac{1}{\frac{Q_g^s}{Q_g^s + Q_l} \frac{P_s}{P_{(z)}} + \frac{Q_l}{Q_g^s + Q_l}} \\ \Rightarrow \bar{\alpha}_{g(z)} &= \bar{\alpha}_g^s \frac{P_s}{P_{(z)}} \frac{1}{\bar{\alpha}_g^s \frac{P_s}{P_{(z)}} + (1 - \bar{\alpha}_g^s)} \\ &\Rightarrow \bar{\alpha}_{g(z)} = \frac{1}{1 + \frac{P_{(z)}}{P_s} \left(\frac{1}{\bar{\alpha}_g^s} - 1\right)}\end{aligned}\quad (40)$$

Eq. (40) is identical to the equation for predicting the local gas volume fraction in a homogeneous two-phase flow in Ref. [10]. Eq. (40) is set as an initial guess to start the non-homogeneous solution.

3.4. The dimensionless governing equations

Ref. [49] details the normalization of the bulk flow equations. The dimensionless parameters are: $x=x/R$, $z=z/R$, $t=\tau/\omega$, $h = H / c_*$, $u_m = \bar{U}_m / V_*$, $w_m = \bar{W}_m / V_*$, $\Lambda = \Omega R / V_*$,

$$V_* = c_*^2 P_{sa} / \mu_* R, \sigma = \omega R / V_*, p = (P - P_a) / P_{sa}, \tilde{\rho} = \bar{\rho} / \rho_*, \tilde{\mu}_m = \bar{\mu}_m / \mu_*, \alpha_g = \bar{\alpha}_g.$$

where $\text{Re}_p^* = \frac{\rho_* V_*}{\mu_* R} c_*^2$ is a typical advection flow Reynolds number, $\text{Re}_s = \frac{\rho_*}{\mu_*} \omega c_*^2$ is a

squeeze film Reynolds number, c_* is a characteristic clearance, ω is a whirl frequency,

and $P_{sa}=P_s-P_a$ is the pressure drop along the seal axial direction. The subscript * denotes a characteristic value. After normalization, the dimensionless equations are:

Continuity equation:

$$\sigma \frac{\partial}{\partial \tau} (\tilde{\rho}_m h) + \frac{\partial}{\partial x} (\tilde{\rho}_m h u_m) + \frac{\partial}{\partial z} (\tilde{\rho}_m h w_m) = 0 \quad (41)$$

Circumferential momentum equation:

$$-h \frac{\partial p}{\partial x} - \frac{\left(k_x u_m - k_J \frac{\Lambda}{2} \right) \tilde{\mu}_m}{h} = \text{Re}_s \frac{\partial}{\partial \tau} (\tilde{\rho}_m h u_m) + \text{Re}_p^* \left(\frac{\partial}{\partial x} (\tilde{\rho}_m h u_m^2 (1+r_1)) + \frac{\partial}{\partial z} (\tilde{\rho}_m h u_m w_m (1+r_2)) \right) \quad (42)$$

Axial momentum equation:

$$-h \frac{\partial p}{\partial z} - \frac{(k_y w_m) \tilde{\mu}_m}{h} = \text{Re}_s \frac{\partial}{\partial \tau} (\tilde{\rho}_m h w_m) + \text{Re}_p^* \left(\frac{\partial}{\partial x} (\tilde{\rho}_m h u_m w_m (1+r_3)) + \frac{\partial}{\partial z} (\tilde{\rho}_m h w_m^2 (1+r_4)) \right) \quad (43)$$

Gas volume fraction:

$$\sigma \frac{\partial}{\partial \tau} (\alpha_g \tilde{\rho}_g h) + \frac{\partial}{\partial x} (\alpha_g \tilde{\rho}_g u_m h) + \frac{\partial}{\partial z} (\alpha_g \tilde{\rho}_g w_m h) = -\frac{1}{V_*} \left(\frac{\partial}{\partial x} (\alpha_g \tilde{\rho}_g U_{dr,g} h) + \frac{\partial}{\partial z} (\alpha_g \tilde{\rho}_g W_{dr,g} h) \right) \quad (44)$$

3.5. Perturbation analysis

Ref. [49, 50] detail the perturbation analysis (small amplitude shaft motions) from which the seal static and dynamic characteristics are obtained. For operation with a centered condition, the seal film thickness is uniform along the circumferential direction ($H = c$). Superimposed on the static position, the journal moves with small amplitude

motions ($\Delta e_x, \Delta e_y$) $\ll c$ at frequency (ω). The film thickness (H) is described by the real part of the following equation:

$$H = c + e^{i\omega t} (\Delta e_x \cos \theta + \Delta e_y \sin \theta) \quad (45)$$

For small amplitude motions, the flow variables $\Phi = (u_m, w_m, p, \dots)$ and mixture properties ($\tilde{\rho}_m, \tilde{\mu}_m$) can be expressed as the sum of zeroth and first order complex fields

$$\Phi = \Phi_x + e^{i\omega t} (\Delta e_x \Phi_x + \Delta e_y \Phi_y) \quad (46)$$

for example,

$$\tilde{\rho}_m = \tilde{\rho}_{m_0} + e^{i\omega t} (\Delta e_x \tilde{\rho}_{m_x} + \Delta e_y \tilde{\rho}_{m_y}) \quad (47)$$

$$\tilde{\mu}_m = \tilde{\mu}_{m_0} + e^{i\omega t} (\Delta e_x \tilde{\mu}_{m_x} + \Delta e_y \tilde{\mu}_{m_y}) \quad (48)$$

$$\alpha_g = \alpha_{g_0} + e^{i\omega t} (\Delta e_x \alpha_{g_x} + \Delta e_y \alpha_{g_y}) \quad (49)$$

Substitution of the perturbation equation of gas volume fraction into the mixture density Eq.(9) and viscosity Eq.(33) and neglecting higher order terms renders:

$$\begin{aligned} \tilde{\rho}_m = & \underbrace{\alpha_{g_0} \tilde{\rho}_{g_0} + (1 - \alpha_{g_0}) \tilde{\rho}_L}_{\tilde{\rho}_{m_0}} \\ & + e^{i\omega t} \left[\Delta e_x \underbrace{(\alpha_{g_0} \tilde{\rho}_{g_x} + \alpha_{g_x} \tilde{\rho}_{g_0} - \alpha_{g_x} \tilde{\rho}_L)}_{\tilde{\rho}_{m_x}} + \Delta e_y \underbrace{(\alpha_{g_0} \tilde{\rho}_{g_y} + \alpha_{g_y} \tilde{\rho}_{g_0} - \alpha_{g_y} \tilde{\rho}_L)}_{\tilde{\rho}_{m_y}} \right] \end{aligned} \quad (50)$$

$$\begin{aligned}
\tilde{\mu}_m &= \underbrace{\alpha_{g_0} \tilde{\mu}_{g_0} + (1 - \alpha_{g_0}) \tilde{\mu}_L + 2\sqrt{\tilde{\mu}_{g_0} \tilde{\mu}_L \alpha_{g_0} (1 - \alpha_{g_0})}}_{\tilde{\mu}_{m_0}} \\
&+ e^{i\omega t} \left[\begin{aligned} &\underbrace{\Delta e_X \left(\alpha_{g_0} \tilde{\mu}_{g_x} + \alpha_{g_x} \tilde{\mu}_{g_0} - \alpha_{g_x} \tilde{\mu}_L + 2\sqrt{\tilde{\mu}_{g_0} \tilde{\mu}_L (\alpha_{g_x} - 2\alpha_{g_0} \alpha_{g_x})} \right)}_{\tilde{\mu}_{m_x}} \right. \\ &\left. + \Delta e_Y \left(\alpha_{g_0} \tilde{\mu}_{g_y} + \alpha_{g_y} \tilde{\mu}_{g_0} - \alpha_{g_y} \tilde{\mu}_L + 2\sqrt{\tilde{\mu}_{g_0} \tilde{\mu}_L (\alpha_{g_y} - 2\alpha_{g_0} \alpha_{g_y})} \right) \right]_{\tilde{\mu}_{m_y}}
\end{aligned}
\tag{51a}
\end{aligned}$$

$$\begin{aligned}
\tilde{\mu}_m &= \underbrace{\alpha_{g_0} \lambda_{g_0} + (1 - \lambda_{g_0}) \tilde{\mu}_L}_{\tilde{\mu}_{m_0}} \\
&+ e^{i\omega t} \left[\begin{aligned} &\Delta e_X \left(\lambda_{g_0} \tilde{\mu}_{g_x} + \lambda_{g_x} \tilde{\mu}_{g_0} - \lambda_{g_x} \tilde{\mu}_L \right) \right]_{\tilde{\mu}_{m_x}} \\ &\left. + \Delta e_Y \left(\lambda_{g_0} \tilde{\mu}_{g_y} + \lambda_{g_y} \tilde{\mu}_{g_0} - \lambda_{g_y} \tilde{\mu}_L \right) \right]_{\tilde{\mu}_{m_y}}
\end{aligned}
\tag{51b}
\end{aligned}$$

The above two equations are used to compute the zeroth and first order density and viscosity of the mixture. Substitution of the film thickness and flow variables into the bulk flow continuity, momentum, and gas volume fraction transport equations leads to a set of zeroth-order and first-order equations.

3.5.1. The zeroth order equations

Because the zeroth order equations are calculated in a steady state, the terms containing time derivations vanish. The zeroth order equations are:

Continuity:

$$\frac{\partial}{\partial x} \left(\tilde{\rho}_{m_0} h_0 u_{m_0} \right) + \frac{\partial}{\partial z} \left(\tilde{\rho}_{m_0} h_0 w_{m_0} \right) = 0 \tag{52}$$

Circumferential momentum:

$$-h_0 \frac{\partial p_0}{\partial x} = \frac{\left(k_{x_0} \tilde{u}_{m_0} - k_{J_0} \frac{\Lambda}{2}\right) \tilde{u}_{m_0}}{h_0} + \text{Re}_P^* \left\{ \frac{\partial}{\partial x} \left(\tilde{\rho}_{m_0} h_0 u_{m_0}^2 (1+r_1) \right) + \frac{\partial}{\partial z} \left(\tilde{\rho}_{m_0} h_0 u_{m_0} w_{m_0} (1+r_2) \right) \right\} \quad (53)$$

Axial momentum:

$$-h_0 \frac{\partial p_0}{\partial z} = \frac{\left(k_{y_0} w_{m_0}\right) \tilde{u}_{m_0}}{h_0} + \text{Re}_P^* \left\{ \frac{\partial}{\partial x} \left(\tilde{\rho}_{m_0} h_0 u_{m_0} w_{m_0} (1+r_3) \right) + \frac{\partial}{\partial z} \left(\tilde{\rho}_{m_0} h_0 w_{m_0}^2 (1+r_4) \right) \right\} \quad (54)$$

Gas volume fraction:

$$\frac{\partial}{\partial x} \left(\alpha_{g_0} \tilde{\rho}_{g_0} \tilde{u}_{m_0} h_0 \right) + \frac{\partial}{\partial z} \left(\alpha_{g_0} \tilde{\rho}_{g_0} w_{m_0} h_0 \right) = -\frac{1}{V_*} \left(\frac{\partial}{\partial x} \left(\alpha_{g_0} \tilde{\rho}_{g_0} \bar{U}_{dr,g_0} h_0 \right) + \frac{\partial}{\partial z} \left(\alpha_{g_0} \tilde{\rho}_{g_0} \bar{W}_{dr,g_0} h_0 \right) \right) \quad (55)$$

In the above equations the variables are the velocity of the mixture mass center along the circumferential (x) and axial (z) directions (u_{m_0}, w_{m_0}), the gas volume fraction and gas density ($\alpha_{g_0}, \tilde{\rho}_{g_0}$), the mixture density and viscosity $\tilde{\rho}_{m_0}, \tilde{\mu}_{m_0}$, the pressure shared by the gas and the liquid (p_0), the diffusion coefficients (r_1, r_2, r_3 , and r_4), the diffusion velocity of the gas along the x and z directions ($\bar{U}_{dr,g_0}, \bar{W}_{dr,g_0}$), and the wall shear stresses ($\tau_{xy}|_0^H$,

$\tau_{zy}|_0^H$).

There are a total of 4 equations and 15 variables. Thus, 11 more equations are needed to obtain a unique solution for the flow field. The current program considers an ideal gas, the gas density is

$$\tilde{\rho}_{g_0} = \frac{P_0}{\rho_* Z_g R_g T} \quad (56)$$

where Z_g is a compressibility factor, R_g is gas constant, and T is temperature.

The mixture density ($\tilde{\rho}_{m_0}$) is volume averaged between the density of gas ($\tilde{\rho}_{g_0}$) and liquid ($\tilde{\rho}_l$)

$$\tilde{\rho}_{m_0} = \alpha_{g_0} \tilde{\rho}_{g_0} + (1 - \alpha_{g_0}) \tilde{\rho}_l \quad (57)$$

$$\tilde{\mu}_{m_0} = \alpha_{g_0} \tilde{\mu}_{g_0} + (1 - \alpha_{g_0}) \tilde{\mu}_l + 2\sqrt{\tilde{\mu}_{g_0} \tilde{\mu}_l \alpha_{g_0} (1 - \alpha_{g_0})} \quad (58a) = (33a)$$

$$\tilde{\mu}_{m_0} = \lambda_{g_0} \tilde{\mu}_{g_0} + (1 - \lambda_{g_0}) \tilde{\mu}_l \quad (58b) = (33b)$$

$U_{dr,g}$ and $W_{dr,g}$ are the gas diffusion velocities along the circumferential (x) and axial (z) directions that determine the diffusion coefficients, and are expressed as

$$\bar{U}_{dr,g_0} = \bar{U}_{gl_0} (1 - \bar{\lambda}_{g_0}) \quad (59)$$

$$\bar{W}_{dr,g_0} = \bar{W}_{gl_0} (1 - \bar{\lambda}_{g_0}) \quad (60)$$

where $\bar{U}_{gl} = \bar{U}_g - \bar{U}_l$ and $\bar{W}_{gl} = (\bar{W}_g - \bar{W}_l)$ are the velocity difference between the gas (g) and liquid (l) along the x and z directions, and $\bar{\lambda}_{g_0}$ is the gas mass fraction. Appendix A details the solution of the diffusion velocities.

Once the diffusion velocities (\bar{U}_{dr,g_0} and \bar{W}_{dr,g_0}) are solved, the diffusion coefficients r_1 , r_2 , r_3 and r_4 are expressed as:

$$r_1 = \frac{\bar{\alpha}_{g_0} \bar{\rho}_{g_0} \bar{U}_{dr,g}^2}{\bar{\rho}_{m_0} \bar{U}_{m_0}^2} \quad (61)$$

$$r_2 = \frac{\bar{\alpha}_{g_0} \bar{\rho}_{g_0} \bar{U}_{dr,g} \bar{W}_{dr,g}}{\bar{\rho}_{m_0} \bar{U}_{m_0} \bar{W}_{m_0}} \quad (62)$$

$$r_3 = \frac{\bar{\alpha}_{g_0} \bar{\rho}_{g_0} \bar{U}_{dr,g} \bar{W}_{dr,g}}{\bar{\rho}_{m_0} \bar{U}_{m_0} \bar{W}_{m_0}} \quad (63)$$

$$r_4 = \frac{\bar{\alpha}_{g_0} \bar{\rho}_{g_0} \bar{W}_{dr,g}^2}{\bar{\rho}_{m_0} \bar{W}_{m_0}^2} \quad (64)$$

Note that r_1 , r_2 , r_3 and r_4 only influence the inertia terms in the momentum equations, Eqs. (53) and (54).

The other two equations are for the shear stresses along the circumferential (x) and axial (z) directions:

$$\tau_{xy}|_0^H = \frac{\bar{\mu}_{m_0}}{H_0} \left(k_{x_0} \bar{U}_{m_0} - k_{r_0} \frac{R\Omega}{2} \right) \quad (65)$$

$$\tau_{zy}|_0^H = \frac{(k_{z_0} \bar{W}_{m_0}) \bar{\mu}_{m_0}}{H_0} \quad (66)$$

For a laminar flow the parameters $k_{x_0} = k_{z_0} = k_{r_0} = 12$, and for a turbulent flow $k_{x_0} = k_{z_0} = \frac{1}{2} (k_{r_0} + k_{s_0})$. The shear parameters on the rotor and stator surfaces are $k_{r_0} = f_{r_0} \text{Re}_{m_{r_0}}$, $k_{s_0} = f_{s_0} \text{Re}_{m_{s_0}}$, respectively. Above the turbulent friction factors on the rotor and stator (f_{r_0} and f_{s_0}) are determined by Moody's formula⁷ [45]. So far, there are 14 variables and 14 equations, so the zeroth order equations can be solved numerically.

⁷ $(f_{r,s})_0 = a_m [1 + (c_m r_{r,s} / H + b_m / (\text{Re}_{r,s})_0)^e]$ is the zeroth order Moody's friction factor at the rotor (r) and stator (s) surfaces; $a_m = 0.001375$, $b_m = 5 \times 10^5$, $c_m = 10^4$, $e = 1/3$; and r_r and r_s are the roughness of the rotor and stator surfaces, respectively [40].

The solution of the zeroth order equations delivers the seal static pressure, the velocity field, and the mixture density, viscosity, gas volume fraction, etc. The seal mass flow rate (\dot{m}), and static reaction force (F_{X_0}, F_{Y_0}) are defined from

$$\dot{m} = \int_0^{2\pi R} \left(\rho_{m_0} H_0 W_{m_0} \right)_{Z=L} R d\theta \quad (67)$$

$$\begin{Bmatrix} F_{X_0} \\ F_{Y_0} \end{Bmatrix} = - \int_0^L \int_0^{2\pi} P_0 \begin{Bmatrix} \cos \theta \\ \sin \theta \end{Bmatrix} R d\theta dz \quad (68)$$

The boundary condition for the zeroth order equations are:

- At the inlet plane $Z = 0^-$, the pressure, the supply pressure is specified to be $P = P_s$.
- At the inlet plane $Z = 0^-$, the mixture inlet gas volume fraction is specified as α_{gs} .
- In the upstream of the seal, the gas and liquid components are well mixed. A technical report (2016) [51] details the measured air and oil volumetric flow rates (Q_{ga} and Q_l) of a uniform clearance seal ($D=0.127$, $L/D=0.36$, $c = 0.203$) for operation with a supply pressure (P_s) 2.5 bara, a discharge pressure (P_d) 1 bara, a shaft speed 3,500 rpm (shaft surface speed $\Omega R = 23.3$ m/s), and an inlet oil temperature 33 °C~35 °C. From the test data, the axial velocities of the air and oil entering the seal are

$$\begin{aligned} \bar{W}_{g_0}^{inlet} &= \frac{Q_{ga}}{\bar{\alpha}_g^s (\pi D c)} \cdot \frac{P_a}{P_s} \\ \bar{W}_l^{inlet} &= \frac{Q_l}{(1 - \bar{\alpha}_g^s) (\pi D c)} \end{aligned} \quad (69)$$

Figure 5 shows the calculated air and oil axial velocities versus gas volume fraction (GVF) at the seal inlet plane. The air and oil inlet axial velocities are quite similar.

Note that at inlet GVF = 0, the air velocity is zero because there is no air being supplied to the seal. Thus, the mixture is regarded as homogeneous at the inlet plane, and the diffusion velocities are zero, $\bar{U}_{dr,g} = \bar{W}_{dr,g} = 0$.

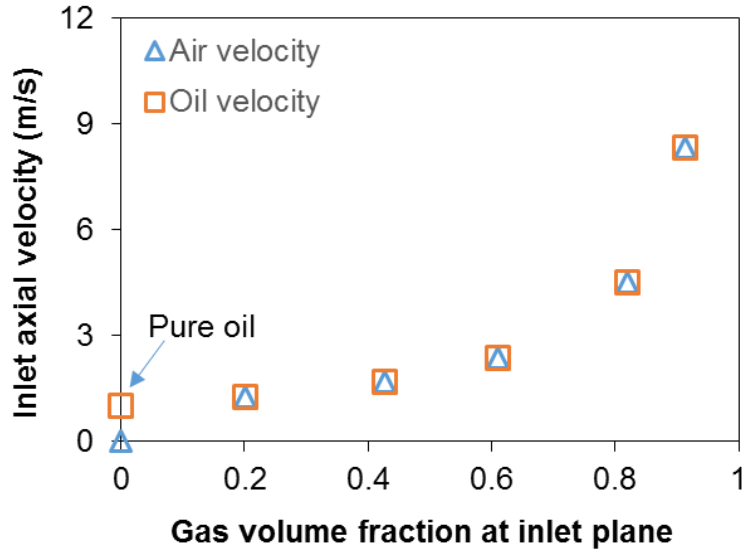


Figure 5 Experimentally estimated air and oil velocity at the seal inlet plane [51]. Supply pressure (P_s) = 2.5 bar (abs), discharge pressure (P_a) = 1 bar (abs), shaft speed (N) = 3,500 rpm (shaft surface speed $\Omega R = 23.3$ m/s). Oil temperature (T_{in}) = 33 °C ~35 °C.

- The inlet pre-swirl ratio (β) of the mixture is specified as a fraction of the shaft surface speed, $U_{ms} = \beta \Omega R$. β is the ratio of the bulk flow circumferential speed to the surface speed of the spinning journal.
- If the fluid is a pure liquid, the entrance pressure drop can be characterized by the pressure loss:

$$P_{Z=0^+} = P_e = P_s - \frac{1}{2} \bar{\rho}_l (1 + \zeta) \bar{W}_l^2 \quad (70)$$

where ζ is an (empirical) entrance pressure loss coefficient ranging from 0.1 to 0.5 [5]. Yang and San Andrés [52] offer more insight on the inlet pressure loss coefficient for sharp edge seals and round edge seals.

- For operation with a compressible flow (mixture), Arghir and Frene [53] utilize Eq. (71) to define the pressure at the seal inlet plane ($Z = 0^+$)

$$P_e = P_s \left\{ 1 + \left(\frac{\gamma_m - 1}{2} \right) (1 + \zeta) M_1^2 \right\}^{\frac{\gamma_m}{1 - \gamma_m}} \quad (71)$$

where γ_m is the ratio of specific heats for the mixture. Currently γ_m is estimated from the mass weighted averages for the gas and liquid ratios of specific heats. That is

$$\gamma_m = \bar{\lambda}_g \gamma_g + (1 - \bar{\lambda}_g) \gamma_l \quad (72)$$

In Eq. (71), $M_1 = (\bar{W}_{m_0} / a)$ is the mixture Mach number and a is the sound speed of the mixture defined as [54]

$$a^{-1} = \sqrt{\rho_{m_0} \left(\frac{\text{GVF}}{\rho_{g_0} a_g^2} + \frac{1 - \text{GVF}}{\rho_{l_0} a_l^2} \right)} \quad (73)$$

Above, the sound speed for the liquid (a_l) and air (a_g) are

$$a_l = \sqrt{\frac{\kappa}{\rho_l}}, \quad a_g = \sqrt{\gamma_g R_g T} \quad (74)$$

where κ is the bulk modulus for the liquid, γ_g is the ratio of specific heats for the gas, and R_g is the specific gas constant ($\gamma_g = 1.4$, and $R_g = 287 \text{ J}/(\text{kg}\cdot\text{K})$ for air).

- At the seal exit plane $Z = L$, the pressure is ambient $P = P_a$. Currently, the model does not include an exit pressure recovery coefficient.

The fluid variables $\Phi_0 = (U_{m0}, W_{m0}, P_0, \dots)$ are periodic: $\Phi_\theta = \Phi(\theta + 2\pi)$.

Note in the following sections both the NHBFM and the HBFM utilize the same boundary conditions for the analysis.

3.5.2. The first order equations

Solution of the zeroth order equation shows that the diffusion coefficients are rather small in magnitude, so the first order equations do not include the perturbation for the diffusion coefficients. After some simplification and dropping the higher order terms, the first order equations become:

Continuity equation:

$$i\sigma \left(h_0 \tilde{\rho}_{m_\chi} + \tilde{\rho}_{m_0} h_\chi \right) + \frac{\partial}{\partial x} \left(h_0 u_{m_0} \tilde{\rho}_{m_\chi} + h_0 \tilde{\rho}_{m_0} u_{m_\chi} + u_{m_0} \tilde{\rho}_{m_0} h_\chi \right) + \frac{\partial}{\partial z} \left(h_0 w_{m_0} \tilde{\rho}_{m_\chi} + h_0 \tilde{\rho}_{m_0} w_{m_\chi} + w_{m_0} \tilde{\rho}_{m_0} h_\chi \right) = 0$$

$$\chi = x, y \quad (75)$$

Circumferential momentum equation:

$$-h_0 \frac{\partial p_\chi}{\partial x} = \left(\gamma_{uu} + i \tilde{\rho}_{m_0} h_0 \text{Re}_s \right) u_{m_\chi} + \gamma_{uw} w_{m_\chi} + \gamma_{uh} h_\chi + \gamma_{u\rho} \tilde{\rho}_{m_\chi} + \gamma_{u\mu} \tilde{\mu}_{m_\chi}$$

$$+ \text{Re}_p^* \left[\frac{\partial}{\partial x} \left(\tilde{\rho}_{m_0} h_0 u_{m_0} u_{m_\chi} (1 + r_{1_0}) \right) + \frac{\partial}{\partial z} \left(\tilde{\rho}_{m_0} h_0 w_{m_0} u_{m_\chi} (1 + r_{2_0}) \right) \right] ; \chi = x, y \quad (76)$$

$$\left[+ \tilde{\rho}_{m_0} h_0 \left(u_{m_\chi} \frac{\partial}{\partial x} \left(u_{m_0} (1 + r_{1_0}) \right) + w_{m_\chi} \frac{\partial}{\partial z} \left(u_{m_0} (1 + r_{2_0}) \right) \right) \right]$$

Axial momentum equation:

$$\begin{aligned}
-h_0 \frac{\partial p_\chi}{\partial z} &= (\gamma_{vv} + i\tilde{\rho}_{m_0} h_0 \text{Re}_s) w_{m_\chi} + \gamma_{vu} u_{m_\chi} + \gamma_{vh} h_\chi + \gamma_{v\rho} \tilde{\rho}_{m_\chi} + \gamma_{v\mu} \tilde{\mu}_{m_\chi} \\
&+ \text{Re}_p^* \left(\frac{\partial}{\partial x} \left(\tilde{\rho}_{m_0} h_0 u_{m_0} w_{m_\chi} (1+r_{3_0}) \right) + \frac{\partial}{\partial z} \left(\tilde{\rho}_{m_0} h_0 w_{m_0} w_{m_\chi} (1+r_{4_0}) \right) \right) ; \chi = x, y \quad (77) \\
&\left(+ \tilde{\rho}_{m_0} h_0 \left(u_{m_\chi} \frac{\partial}{\partial x} (w_{m_0} (1+r_{3_0})) + w_{m_\chi} \frac{\partial}{\partial z} (w_{m_0} (1+r_{4_0})) \right) \right)
\end{aligned}$$

Gas volume fraction:

$$\begin{aligned}
&i\sigma \left(h_0 \tilde{\rho}_{g_0} \alpha_{g_\chi} + h_0 \alpha_{g_0} \tilde{\rho}_{g_\chi} + \tilde{\rho}_{g_0} \alpha_{g_0} h_\chi \right) \\
&+ \frac{\partial}{\partial x} \left(h_0 u_{m_0} \tilde{\rho}_{g_0} \alpha_{g_\chi} + h_0 u_{m_0} \alpha_{g_0} \tilde{\rho}_{g_\chi} + h_0 u_{m_\chi} \tilde{\rho}_{g_0} \alpha_{g_0} + h_\chi u_{m_0} \tilde{\rho}_{g_0} \alpha_{g_0} \right) \\
&+ \frac{\partial}{\partial z} \left(h_0 w_{m_0} \tilde{\rho}_{g_0} \alpha_{g_\chi} + h_0 w_{m_0} \alpha_{g_0} \tilde{\rho}_{g_\chi} + h_0 w_{m_\chi} \tilde{\rho}_{g_0} \alpha_{g_0} + h_\chi w_{m_0} \tilde{\rho}_{g_0} \alpha_{g_0} \right) ; \chi = x, y \quad (78) \\
&= \\
&-\frac{1}{V^*} \left\{ \frac{\partial}{\partial x} \left(h_0 u_{dr,g_0} \tilde{\rho}_{g_0} \alpha_{g_\chi} + h_0 u_{dr,g_0} \alpha_{g_0} \tilde{\rho}_{g_\chi} + h_\chi u_{dr,g_0} \tilde{\rho}_{g_0} \alpha_{g_0} \right) \right\} \\
&\left\{ + \frac{\partial}{\partial z} \left(h_0 w_{dr,g_0} \tilde{\rho}_{g_0} \alpha_{g_\chi} + h_0 w_{dr,g_0} \alpha_{g_0} \tilde{\rho}_{g_\chi} + h_\chi w_{dr,g_0} \tilde{\rho}_{g_0} \alpha_{g_0} \right) \right\}
\end{aligned}$$

In the above equations the subscript $\chi = x, y$. There are 17 variables ($u_{m_\chi}, w_{m_\chi}, \tilde{\rho}_{m_\chi}, \tilde{\mu}_{m_\chi}, \tilde{\rho}_{g_\chi}, p_\chi, \alpha_{g_\chi}, \gamma_{uu}, \gamma_{uw}, \gamma_{uh}, \gamma_{u\rho}, \gamma_{u\mu}, \gamma_{vu}, \gamma_{vw}, \gamma_{vh}, \gamma_{v\rho}, \gamma_{v\mu}$) and only 4 equations. So 13 more equations are need. Zhou [49] (Appendix B of h Ph.D. dissertation) details 10 equations for the first order shear coefficients ($\gamma_{uu}, \gamma_{uw}, \gamma_{uh}, \gamma_{u\rho}, \gamma_{u\mu}, \gamma_{vu}, \gamma_{vw}, \gamma_{vh}, \gamma_{v\rho}, \gamma_{v\mu}$). For an ideal gas, the first order gas density (ρ_{g_χ}) can be represented as

$$\tilde{\rho}_{g_\chi} = \frac{d\tilde{\rho}_g}{dP} P_\chi = \frac{p_\chi}{\rho_g Z_g R_g T}, \chi = x, y \quad (79)$$

Eqs. (50) and (51) details the first order density and viscosity equation of the mixture:

$$\tilde{\rho}_{m_\alpha} = \alpha_{g_0} \tilde{\rho}_{g_\alpha} + \alpha_{g_\chi} (\tilde{\rho}_{g_0} - \tilde{\rho}_L), \chi = x, y \quad (80)$$

$$\tilde{\mu}_{m_\chi} = \underbrace{\alpha_{g_0} \tilde{\mu}_{g_\chi}}_0 + \alpha_{g_\chi} \tilde{\mu}_{g_0} - \alpha_{g_\chi} \tilde{\mu}_L + 2\sqrt{\tilde{\mu}_{g_0} \tilde{\mu}_L (\alpha_{g_\chi} - 2\alpha_{g_0} \alpha_{g_\chi})}, \chi = x, y \quad (81a)$$

and

$$\tilde{\mu}_{m_\chi} = \underbrace{\lambda_{g_0} \tilde{\mu}_{g_\chi}}_0 + \lambda_{g_\chi} \tilde{\mu}_{g_0} - \alpha_{g_\chi} \tilde{\mu}_L, \chi = x, y \quad (81b)$$

In Eq. (81), $\alpha_{g_0} \tilde{\mu}_{g_\chi} = 0$ because the gas viscosity $\tilde{\mu}_g$ is regarded as a constant.

Thus far, there are 17 equations and 17 variables, so the first order flow equations can be solved.

The seal complex stiffness can be obtained from the integration of the first order pressures:

$$\begin{bmatrix} H_{XX} & h_{XY} \\ h_{YX} & H_{YY} \end{bmatrix} = -\int_0^L \int_0^{2\pi} \begin{bmatrix} P_X \cos \theta & P_Y \cos \theta \\ P_X \sin \theta & P_Y \sin \theta \end{bmatrix} R d\theta dz \quad (82)$$

where H and h are the direct and cross-coupled complex dynamic stiffnesses, respectively.

The real and imaginary parts of H and h render frequency dependent dynamic force coefficients for the two component flow seal:

$$\begin{aligned} K_{ij(\omega)} + i\omega C_{ij(\omega)} &\leftarrow H_{ij(\omega)} \\ k_{ij(\omega)} + i\omega c_{ij(\omega)} &\leftarrow h_{ij(\omega)} \end{aligned} \quad i, j = X, Y, i = \sqrt{-1} \quad (83)$$

where $K_{ij(\omega)}$ is the seal dynamic stiffness, and $C_{ij(\omega)}$ is the viscous damping coefficient.

The boundary condition for the first order equations are:

- For operation with a liquid, the first order pressure at the inlet plane $Z = 0^-$ is

$$P_{e_\chi} = -\frac{(1+\zeta)}{2} \left[2\bar{\rho}_{m_0} \bar{W}_{m_0} \bar{W}_{m_\chi} + \bar{W}_{m_0}^2 \bar{\rho}_{m_\chi}^2 \right], \chi = X, Y \quad (84)$$

- For operation with a mixture, the first order pressure at the inlet plane $Z = 0^-$ is

$$\begin{aligned}
P_{e_\chi} &= \frac{\partial P_0}{\partial \bar{W}_{m_0}} \bar{W}_{m_\chi} \\
\Rightarrow P_{e_\chi} &= -P_s \cdot \gamma_m \cdot (1 + \zeta) \cdot M_1 \cdot \left\{ 1 + \left(\frac{\gamma_m - 1}{2} \right) (1 + \zeta) M_1^2 \right\}^{\frac{1-2\gamma_m}{\gamma_m-1}} \cdot \frac{1}{a} \cdot \bar{W}_{m_\chi}, \chi = X, Y
\end{aligned} \tag{85}$$

where γ_m , M_1 , and a are defined in Eq. (72) and Eq. (73), \bar{W}_{m_χ} is the first order inlet mixture velocity.

- At the inlet plane $Z = 0^+$, the first order inlet pre-swirl ratio (β) of the mixture $U_{ms} = 0$.
- At the inlet plane $Z = 0^+$, the first order gas volume fraction is

$$\alpha_\chi = \frac{\partial \alpha_0}{\partial P_0} P_\chi, \text{ the subscript } \chi = X, Y.$$

- At the seal exit plane $Z = L$, the first order pressure is $P_\chi = 0$, $\chi = X, Y$.
- The first order fluid variables $\Phi_\chi = (U_{m\chi}, W_{m\chi}, P_\chi, \dots)$ are periodic: $\Phi_\theta = \Phi(\theta + 2\pi)$.

Note that since the seal is axisymmetric, the complex dynamic stiffnesses show $H_{XX} = H_{YY}$, and $h_{XY} = -h_{YX}$. Thus, the solution procedure only requires to solve for P_X . Appendix C details the solution procedure for the zeroth and first order equations.

3.6. Closure

This section presents a nonhomogeneous bulk flow model (NHBFM) for two-phase flow uniform clearance annular seals. The NHBFM has the following features:

- a) Compared to a homogeneous bulk flow model (HBFM), the NHBFM contains four additional diffusion coefficients (r_1 , r_2 , r_3 , and r_4) in the inertia terms of the circumferential and axial momentum equations. The diffusion coefficients are used to account for the influence of the drag force between the gas and liquid phases on the mixture flow fields.
- b) The NHBFM contains a transport equation for the gas volume fraction (GVF). The GVF transportation equation is based on the gas continuity equation.
- c) In the perturbation analysis, the HBFM utilizes a first order mixture density that is based on the bulk modulus of the two-phases [10]. On the other hand, the NHBFM includes a perturbation of the gas volume fraction, from which the first order mixture density is derived, as shown in Eq. (79).
- d) The NHBFM utilizes two formulas, Equations (33a) and (33b), to evaluate the effective viscosity (μ_m) of the mixture flow. Eq. (33a) is based on the gas volume averaged method [46] and Eq. (33b) is from the gas mass fraction weighted formula [47]. As will be demonstrated in the following section, Eq.(33a) is more suitable for low pressure applications (say, a few bars), and Eq. (33b) is better for applications of high pressure conditions (i.e., the supply pressure is > 20 bar), according to the current analysis.

4. RESULTS AND DISCUSSION

This section presents predictions versus measurements on the leakage, gas volume fraction, shear drag power, and dynamic force coefficients of two uniform clearance annular seals supplied with a two-component mixture and operating under both a high pressure [55] and a low pressure condition [11]. The high pressure tests emulate operating conditions for a subsea multiphase pump [55]. The low pressure seal tested by San Andrés and Lu [11] in 2018 is suitable to emulate inter-stage seals and impeller eye seals in electrical submersible pumps (ESPs).

4.1. High pressure annular seal

4.1.1. Static characteristics

Zhang and Childs [55] conduct a series of tests to quantify the effect of inlet gas volume fraction on the leakage and dynamic force coefficients of uniform clearance seals used as balance pistons in multiphase pumps. Table 1 lists one of the test seal having a nominal diameter $D = 89.3$ mm, length $L = 57.8$ mm ($L/D = 0.65$), and a radial clearance $c = 0.14$ mm. The lubricant is synthetic silicon oil with a viscosity 4.53 cP at 40 °C and a density of 899 kg/m³. The gas component is compressed dry air. During the tests, the seal discharge pressure is constant at 6.9 bara, and the supply pressure is 44.8 bara. The analysis uses a bubble diameter equal to the size of the seal radial clearance ($d_g = c$). The current analysis for the high pressure seal utilizes the viscosity formula defined in Eq. (33b) from Ref. [47] as the model integrated with this equation delivers an accurate

prediction of leakage.

As the authors in Ref. [55] describe, during the tests when the inlet gas volume fraction is greater than 4%, the floating housing holding the test seals experienced high amplitude, low frequency sub-synchronous vibrations. The frequency at which the housing vibrates reduced as the mixture inlet GVF increased. When the inlet GVF is > 6%, the housing touches the rotor, so no further tests could be conducted.

Table 1. Dimensions of test annular seal and fluids physical properties [55].

Diameter, $D = 2R$	89.3 mm
Length, L	57.8 mm
Radial Clearance c	0.14 ± 0.005 mm
Silicon Oil viscosity, μ_l	4.53 cP (40 °C)
Density, ρ_l	899 kg/m ³
Air viscosity, μ_{ga}	0.018 cP (20 °C)
Density, ρ_{ga}	1.14 kg/m ³ at $P_a = 1$ bara
Supply pressure	44.8 bara
Discharge pressures	6.9 bara
Top journal speed, Ω_{\max}	7.5 krpm
Rotor surface speed, $\frac{1}{2}D\Omega_{\max}$	35.1 m/s
Pre-swirl	0

Figure 6 shows the measured leakage [55] and predictions from the nonhomogeneous bulk flow model (NHBFM) and a homogeneous bulk flow model (HBFM). For operation with a pure liquid, an inlet pressure loss coefficient at $\zeta = 0.2$ is utilized in the prediction model. For operation with a mixture, Eq. (71) for a compressible fluid defines the pressure at the seal inlet plane ($Z = 0^+$). Both prediction models utilize an inlet pressure loss

coefficients $\zeta = 0$. In both models the exit pressure loss coefficient is nil. With an inlet GVF at $\text{GVF} < 4\%$, the predicted leakage from both models increases with GVF.

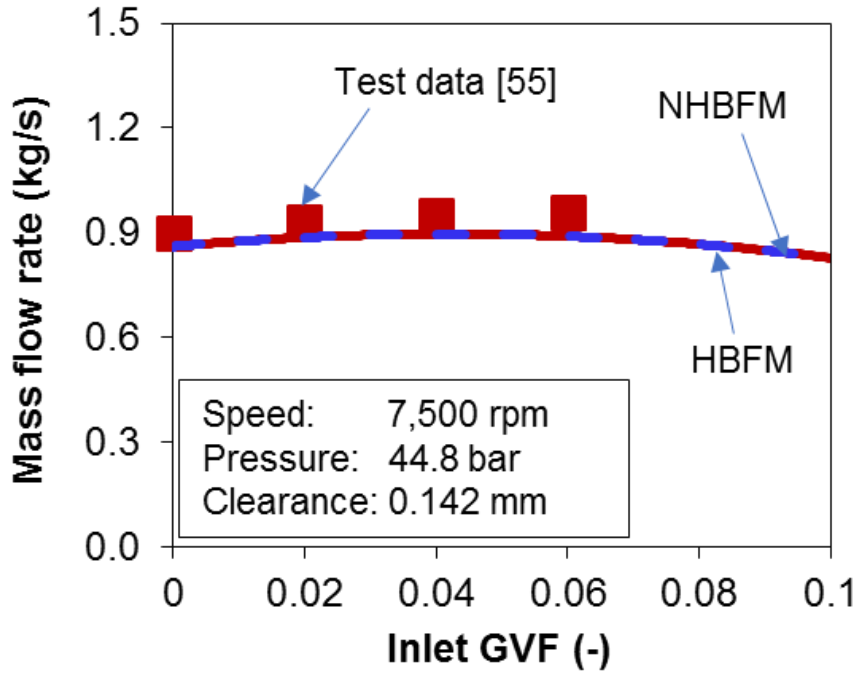


Figure 6 Seal leakage for pure oil and two-phase flow condition. Supply pressure (P_s) = 44.8 bara, discharge pressure (P_a) = 6.9 bara, shaft speed (N) = 7,500 rpm ($\Omega R = 35.1$ m/s). Inlet GVF = 0, 0.02, 0.04, 0.06, 0.08, and 0.1. Test data from Ref. [55].

Table 2 lists the flow axial, circumferential and mixture bulk flow Reynolds numbers,

defined as $Re_{mz} = \frac{\rho_m V_z c}{\mu_m}$, $Re_{mc} = \frac{\rho_m V_c c}{\mu_m}$, and $Re_{ms} = \sqrt{Re_{mz}^2 + Re_{mc}^2}$, respectively. As the

inlet GVF increases from 0 to 0.06, the inlet Reynolds number increases from 870 to 920.

For operation with inlet $\text{GVF} = 0.04$ and 0.06 , the Reynolds number is $\sim 1,100$, indicating

the mixture flow is in a laminar flow regime⁸ [66].

⁸ The definition of flow condition in Ref. [66] is for reference only as it is pertinent to pure liquid seal.

Figure 7 shows the predicted seal shear drag power versus inlet gas volume fraction (GVF). The shear drag remains constant as the inlet GVF increases from 0 to 0.1. Note at inlet GVF=0.1, the gas mass fraction is only 0.6% at the seal inlet plane. Both models deliver the same amount of shear drag power.

Table 2. Calculated flow Reynolds number at the inlet and exit planes of test seal in Ref. [55].

GVF		GMF‰		Re _{mz}		Re _{mc}		Re _{ms}	
inlet	Exit	Inlet	Exit	inlet	exit	inlet	exit	inlet	exit
0	0	0		709	709	505	505	870	870
0.02	0.12	1.16		733	792	496	486	886	929
0.04	0.22	2.36		749	890	493	480	905	1012
0.06	0.29	3.61		758	987	490	477	920	1096

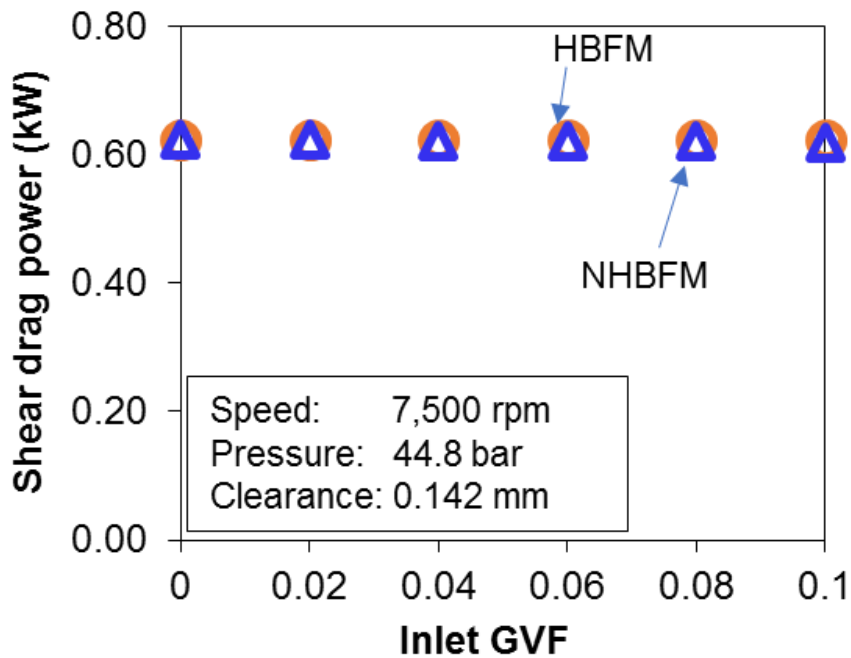


Figure 7 Predicted seal shear drag power for pure oil and two-phase flow condition. Supply pressure (P_s) = 44.8 bara, discharge pressure (P_a) = 6.9 bara, shaft speed (N) = 7,500 rpm ($\Omega R = 35.1$ m/s). Inlet GVF=0, 0.02, 0.04, 0.06, 0.08, and 0.1.

Figure 8 shows the predicted pressure profile for a centered seal from both the NHBFM and the HBFM. Both models predict similar pressure profile, and thus the graph only shows the pressure profile predicted from the NHBFM. For operation with a pure liquid condition, the pressure experiences a sudden drop at the inlet plane due to the fluid inertia effect. From Eq.(69) the pressure loss is $(P_s - P_e) = \frac{1}{2} \bar{\rho}_l (1 + \zeta) \bar{W}_l^2 = 2.9$ bar, where $\bar{\rho}_l = 899$ kg/m³, $\zeta = 0.2$, and $\bar{W}_l = \frac{\dot{m}_l}{\rho_l \pi D c} = 24.2$ m/s. The pressure drops linearly within the seal film land as the flow progresses toward the seal exit plane.

For operation with a gas in liquid mixture, the pressure profile becomes more parabolic as the inlet GVF increases. As a reference, the figure also shows the pressure profile for operation with a pure gas (GVF=1) condition. Note the large pressure drop at the inlet plane because of the large density at high supply pressure.

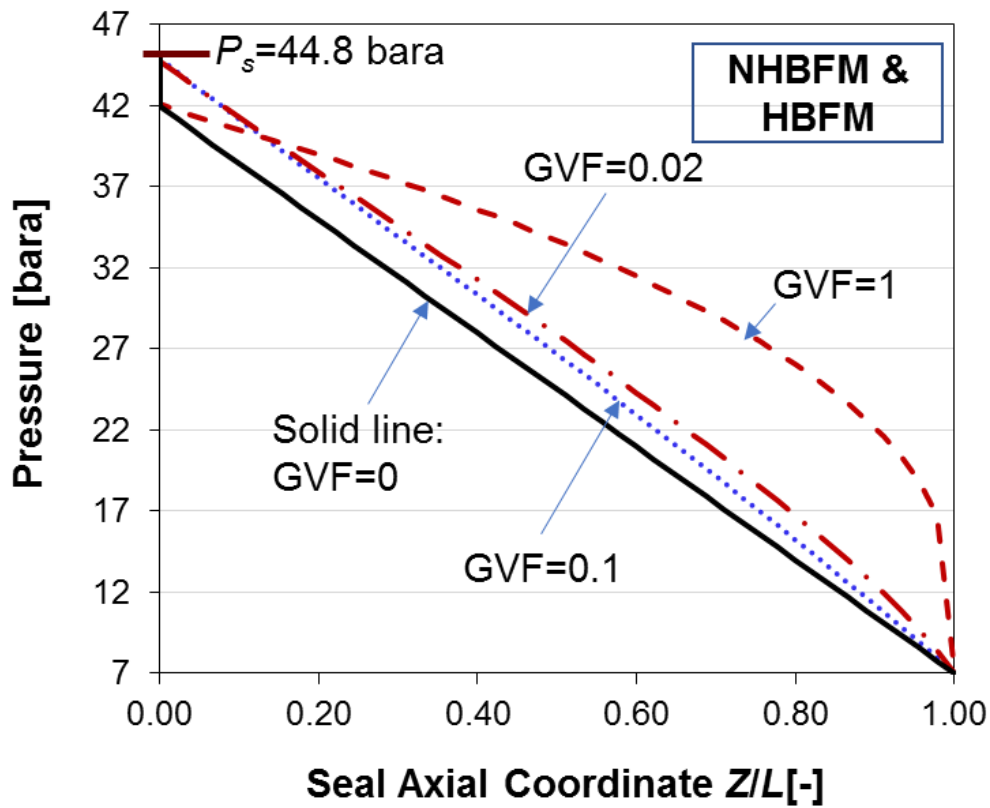


Figure 8 Pressure along the seal axial location predicted by HBFM and NHBFM. Shaft speed 7,500 rpm, seal inlet pressure 44.8 bara, discharge pressure 6.9 bara

Figure 9 shows the NHBFM and the HBFM predicted gas volume fraction along the seal axial coordinate (Z/L). The symbols represent GVF predicted by the NHBFM and the solid lines stand for the ones obtained from the HBFM. For a specific inlet GVF, because both models predict similar GVF profiles in the seal film land, the symbols and line overlap. Recall that if the two-phase flow is homogeneous, the gas volume fraction (GVF) follows Eq. (40), with the values shown on the right axis of graph.

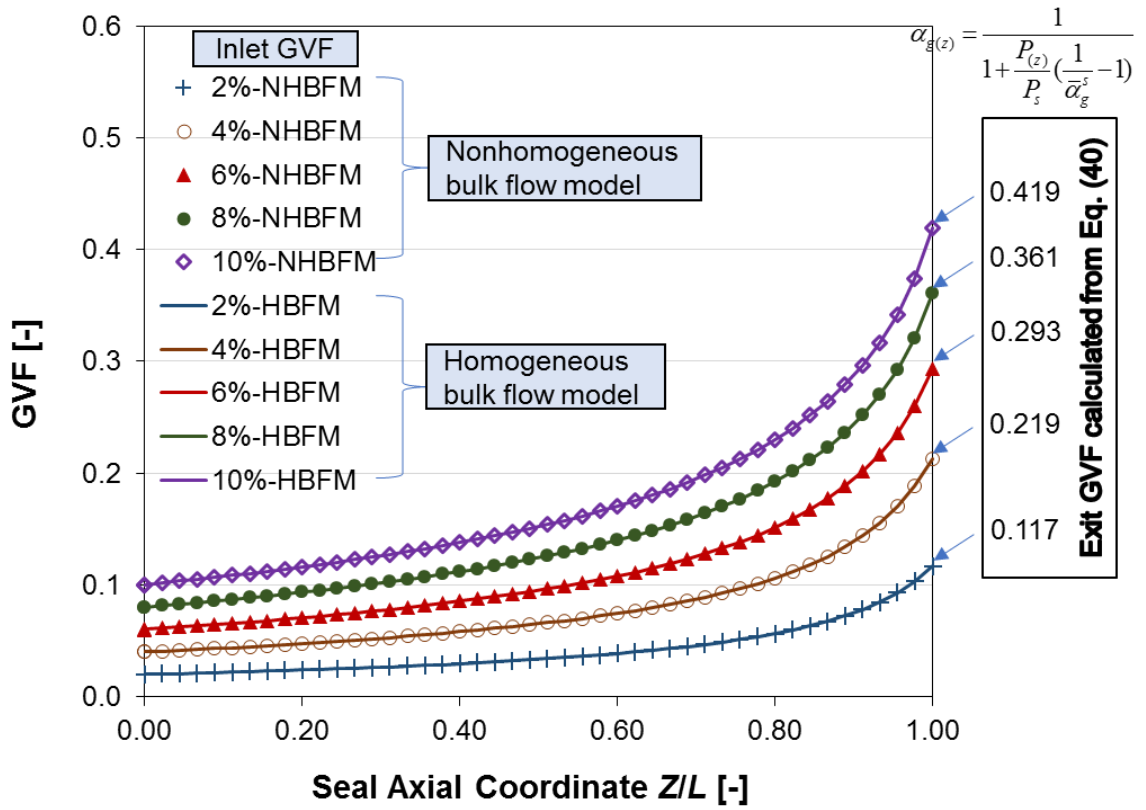


Figure 9 Predicted gas volume fraction (GVF) versus the seal axial coordinate (Z/L). Shaft speed 7,500 rpm, seal inlet pressure 44.8 bara, discharge pressure 6.9 bara. Symbols: nonhomogeneous bulk flow model (NHBFM), Lines: homogeneous bulk flow model (HBFM).

Figure 10 shows the axial velocity difference ($\bar{W}_{gl} = \bar{W}_g - \bar{W}_l$) between the gas and liquid components. Appendix B details the process to obtain \bar{W}_{gl} . Although small in magnitude (about 0.1% of the bulk flow axial velocity), the slip velocity has its maximum magnitude at the seal exit plane ($Z=L$) of the seal. The results are in agreement with a CFD analysis by Yang et al. [35] showing that the mixture is homogeneous along the seal film land; turning nonhomogeneous at the seal exit plane.

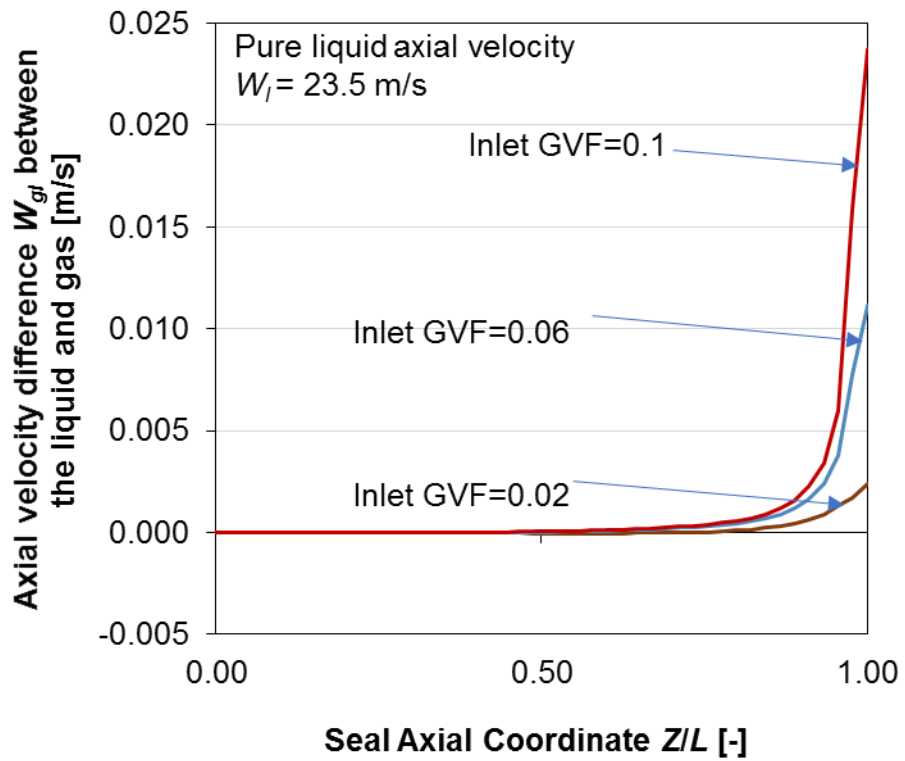


Figure 10 Axial velocity difference between the liquid and gas components along the seal axial location. Shaft speed 7,500 rpm, seal inlet pressure 44.8 bara, discharge pressure 6.9 bara.

4.1.2. First order flow variables

Eq.(82) shows that the first order pressures (P_X and P_Y) produce the seal complex dynamic force coefficients (H_{ij} and h_{ij}). Thus, this section presents examples of the NHBFM and HBFM predicted first order flow fields, such as gas volume fraction (α_{gY}), density of mixture (ρ_{mY}), and pressure (P_Y) along the seal circumferential direction (Θ) due to a perturbation⁹ $h_Y = \sin(\Theta)$.

In the NHBFM, the flow fields are solved iteratively until the first order pressure P_Y converges, i.e., $h_Y \rightarrow \alpha_{gY} \rightarrow \rho_{mY} \rightarrow P_Y \rightarrow \alpha_{gY} \dots$. Above, Eq.(78) solves α_{gY} ; Eq. (79) and Eq. (80) produces ρ_{mY} . In the HBFM, the flow variables are solved differently, i.e., $h_Y \rightarrow \rho_{mY} \rightarrow P_Y \rightarrow \rho_{mY} \dots$, where ρ_{mY} is [50]

$$\rho_{mY} = \frac{\rho_{m0}}{\kappa_{eff}} \cdot P_Y \quad (86)$$

with κ_{eff} as the mixture effective bulk modulus [50]

$$\frac{1}{\kappa_{eff}} = \frac{1}{\kappa_{liquid}} + \alpha_{g0} \left(\frac{1}{\kappa_{gas}} - \frac{1}{\kappa_{liquid}} \right) \quad (87)$$

where $\kappa_{liquid} = 1 \text{ GPa}$, and $\kappa_{gas} = 131 \text{ kPa}$ are the liquid and gas bulk modulus.

Figure 11 shows the predicted real and imaginary parts of the first order flow fields (α_{gY} , ρ_{mY} , and P_Y) along the seal circumferential coordinate (Θ), and at the axial coordinate $Z = L/2$. The shaft speed is 7,500 rpm, and the perturbation has a low frequency = 1 HZ. Recall again that the HBFM does not need α_{gY} to solve ρ_{mY} . Thus, Figure 11 does not include α_{gY} for the HBFM.

⁹ Note h_Y has an unit (m^{-1}), and P_Y has an unit Pa/m.

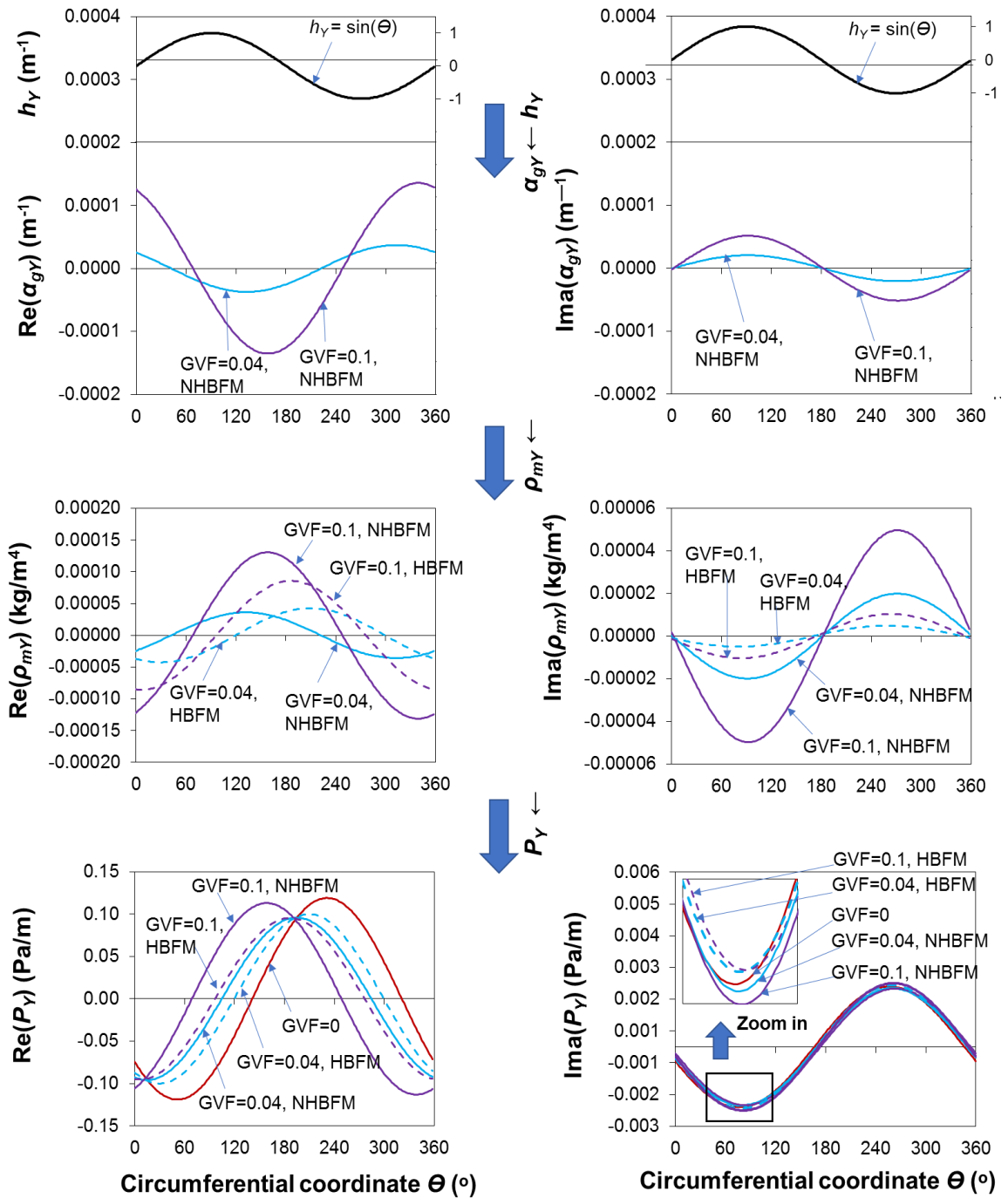


Figure 11 Real and imaginary parts of the first order fluids variables (GvF_Y , ρ_{mY} , P_Y) versus circumferential direction (θ), axial coordinate $Z = L/2$. Shaft speed 7,500 rpm, whirl frequency 1 HZ. Seal inlet pressure 44.8 bara.

The graphs on the left of Figure 11 show the real part of the first order flow fields, $\text{Re}(\alpha_{gY}, \rho_{mY}, P_Y)$; and the graphs on the right show the imaginary part of the first order flow fields $\text{Ima}(\alpha_{gY}, \rho_{mY}, P_Y)$. From top to bottom, the graphs show h_Y , α_{gY} (for the NHBFM only), ρ_{mY} , and P_Y .

For operation with a specific inlet GVF, i.e., $\text{GVF}=0.1$, the real part of the first order density (ρ_{mY}) and pressure (P_Y) predicted from the two models differ in their phase angles with respect to h_Y . However, the phase angle of the imaginary part of ρ_{mY} and P_Y remain almost unchanged. Thus, the models are expected to deliver different $\text{Re}(H, h)$ but similar $\text{Ima}(H, h)$.

Figure 12 shows the phase angle between $\text{Re}(P_Y)$ and h_Y . For operation with a pure liquid condition ($\text{GVF}=0$), $\text{Re}(P_Y)$ is 141.3° out of phase relative to (h_Y), indicating that the real part of the dynamic force opposes the shaft motion. As the inlet GVF increases from $0 \rightarrow 0.04 \rightarrow 0.1$, the phase angle reduces from $141.3^\circ \rightarrow 119.2^\circ \rightarrow 96.5^\circ$ as predicted by the HBFM, and from $141.3^\circ \rightarrow 104.8^\circ \rightarrow 68.5^\circ$ as predicted by the NHBFM. Note that the smaller the phase angle between $\text{Re}(P_Y)$ and h_Y , the more likely the seal is to produce a negative direct stiffness.

The bottom right graph on Figure 11 shows $\text{Ima}(P_Y)$ versus θ . As the inlet GVF increases, the amplitude of the NHBFM predicted $\text{Ima}(P_Y)$ slightly increases ($\sim 5\%$), indicating that for the specific operating conditions, the damping coefficient increases with inlet GVF (within the range $0 < \text{GVF} < 0.1$).

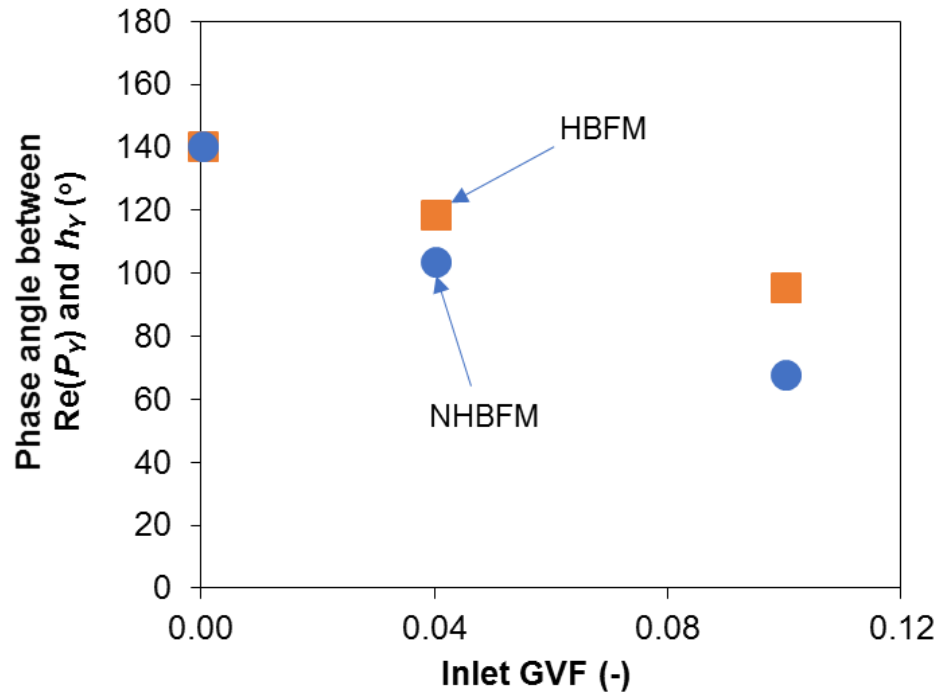


Figure 12 Real part of the first order pressure $Re(P_\gamma)$ along the circumferential direction (Θ), axial coordinate $Z = L/2$. Shaft speed 7,500 rpm, whirl frequency 1 HZ. Seal inlet pressure 44.8 bara.

4.1.3. Dynamic force coefficients

Figure 13 through Figure 16 show the predicted and the experimentally estimated complex dynamic stiffnesses versus excitation frequency (ω) for the seal tested in Ref. [55]. The inlet GVF increases discretely from 0 (pure liquid) to a mixture with inlet GVF = 6%. The symbols represent test data, the solid lines represent predictions from the current NHBFM, and the broken lines stand for predictions based on the HBFM [10]. For operation with both a pure liquid and a mixture, an inlet pressure loss coefficient $\zeta = 0.2$ is utilized for the prediction. For operation with a mixture, Eq. (71) for a compressible flow defines the pressure at the seal inlet plane ($Z = 0^+$). The predicted seal dynamic force

coefficients are obtained for a centered seal condition. Recall the test rig operates at shaft speed 7,500 rpm, supply and discharge pressures equal 44.8 bara and 6.9 bara, respectively.

Figure 13 shows the predicted and measured real parts of the seal direct complex dynamic stiffness $\text{Re}(H)_{XX,YY}$ versus excitation frequency (ω). Since the prediction is conducted at a seal centered condition, the results show $\text{Re}(H) = [\text{Re}(H)_{XX} = \text{Re}(H)_{YY}]$. Thus, the predictions only label $\text{Re}(H)$ on the graphs. The experiment shows that the seal static direct stiffness ($\text{Re}(H)_{XX,YY}$ at $\omega \rightarrow 0$ Hz) is close to ~ 23 MN/m for operation with a pure liquid. At just 2% in inlet GVF, the static direct stiffness reduces to ~ 13 MN/m. When the inlet GVF is 4%, the seal direct stiffness reduces to only ~ 5 MN/m. As the inlet GVF grows to 6%, the seal becomes statically unstable ($K = \text{Re}(H)_{\omega=0} < 0$) as it generates a negative static stiffness.

Both the NHBFM and HBFM predict a reduction of the direct stiffness as the seal inlet GVF increases. Recall from Figure 12 that as the inlet GVF increases from 0 to 0.1, the phase angle between $\text{Re}(P_Y)$ and h_Y reduces from 141.3° to 68.5° as predicted by the NHBFM, and from 141.3° to 96.5° as predicted by the HBFM. Thus, the NHBFM predicted $\text{Re}(H)$ decreases faster with inlet GVF than that predicted by the HBFM.

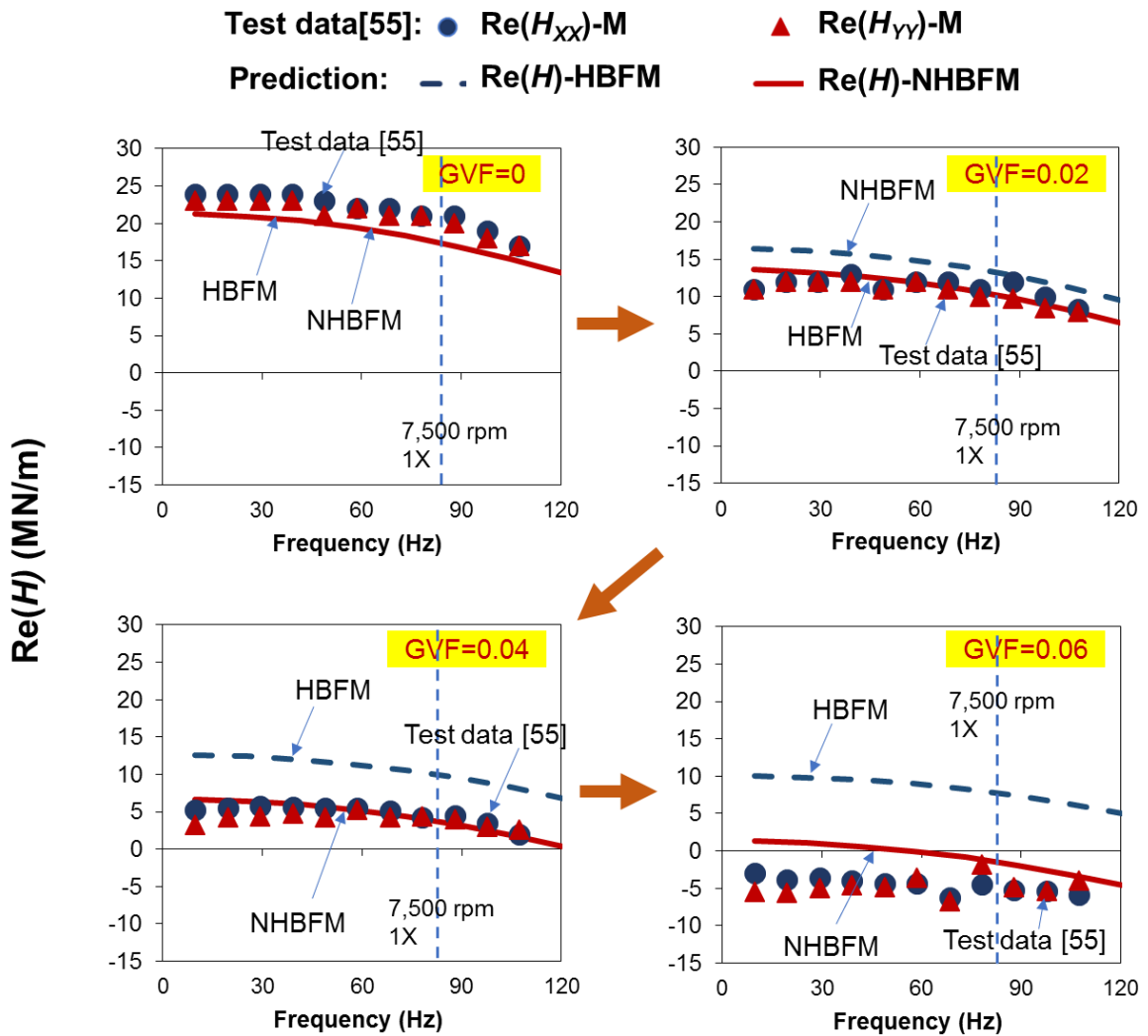


Figure 13 Real part of direct complex dynamic stiffness, $Re(H)_{xx,yy}$, versus excitation frequency. Shaft speed 7,500 rpm (150 HZ), seal inlet pressure 44.8 bara, discharge pressure 6.9 bara. Symbols: test data in Ref. [55], Solid line: prediction from NHBFM. Broken line: prediction from HBFM.

Figure 14 shows the predicted and measured real parts of the seal complex dynamic cross-coupled stiffness $Re(h)_{xy,yx}$ versus excitation frequency (ω). In general, the experimental data for operation with either a pure liquid or with a mixture with inlet GVF $\leq 6\%$ shows that the cross-coupled dynamic stiffness does not have a frequency dependent

effect. The cross-coupled dynamic stiffness increases slightly from ~12 MN/m to about 17 MN/m as the flow turns from a pure liquid to a two-phase flow mixture. Both the HBFM and NHBFM under predict the cross-coupled dynamic stiffness by ~30%. The NHBFM delivers about 8% larger $Re(h)$ compared to the HBFM prediction.

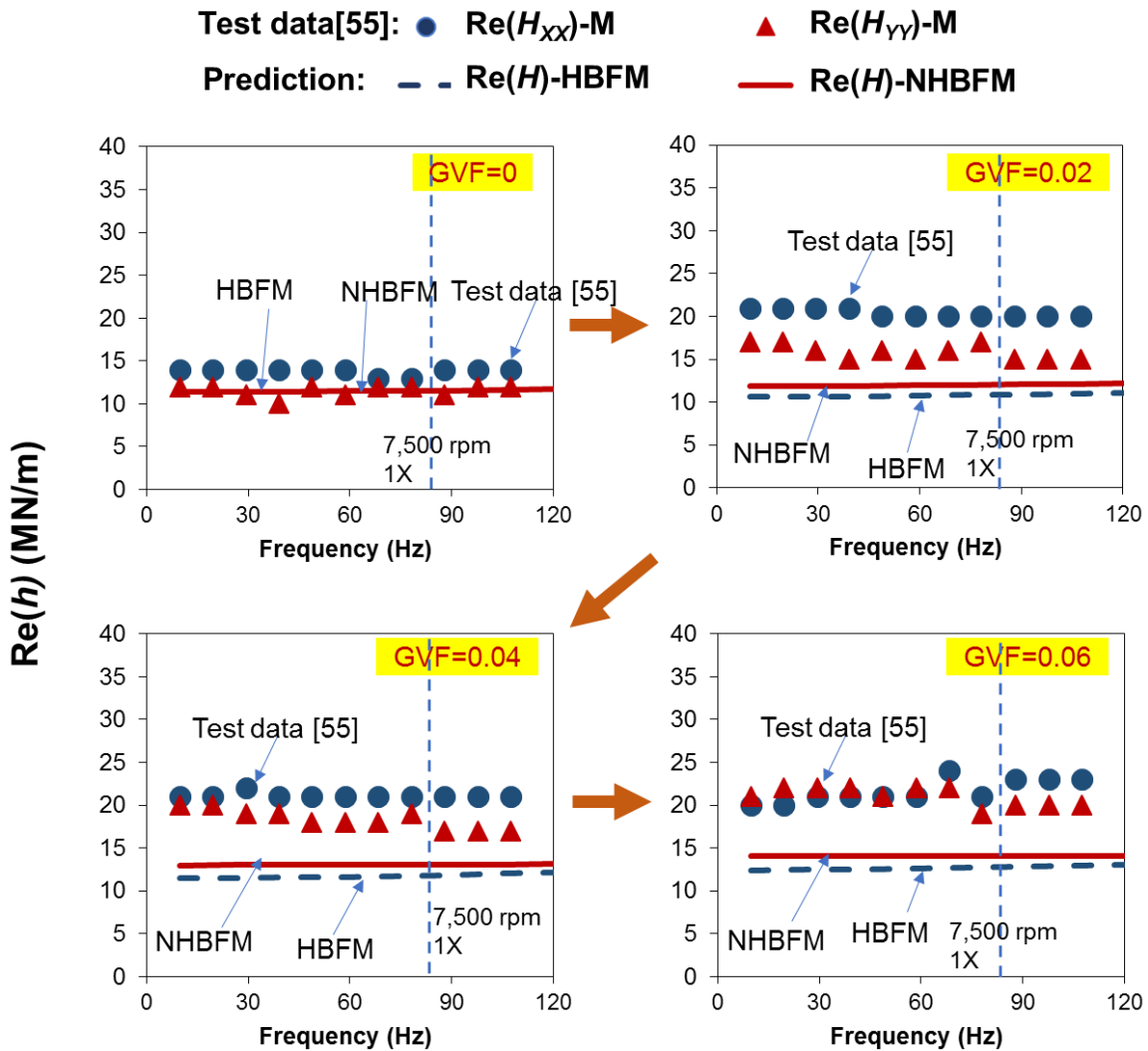


Figure 14 Real part of cross-coupled complex dynamic stiffness, $Re(H)_{XY,YX}$, versus excitation frequency. Shaft speed 7,500 rpm (150 HZ), seal inlet pressure 44.8 bara, discharge pressure 6.9 bara. Symbols: test data in Ref.[55], Solid line: prediction from NHBFM. Broken line: prediction from HBFM.

Figure 15 shows the predicted and measured imaginary parts $\text{Ima}(H)_{XX,YY}$ of the seal direct complex dynamic stiffness versus excitation frequency (ω). Both models predict well $\text{Ima}(H)_{XX,YY}$ for operation with a pure liquid, but under predicts $\text{Ima}(H)_{XX,YY}$ for the seal operating with a two-phase flow condition. Both the experiments and predictions show that $\text{Ima}(H)_{XX,YY}$ increase slightly when air mixes with a liquid. Note that at a supply pressure of 44.8 bara and an inlet GVF = 0.1, the gas mass fraction is only $\lambda_g = 5.5\%$. For operation with an inlet GVF=6%, the NHBFM predicts a 5% larger $\text{Ima}(H)_{XX,YY}$ compared to the HBFM prediction.

Figure 16 shows the predicted and measured imaginary parts ($\text{Ima}(h)_{XY,YX}$) of the seal cross-coupled complex dynamic stiffness versus excitation frequency (ω). Note that although $\text{Ima}(h)_{XY,YX}$ are quite small in magnitude compared to the direct terms, the model still predicts well $\text{Ima}(h)_{XY,YX}$ for operation with a pure liquid condition. For operation with a two-phase flow condition, the experimental estimated $\text{Ima}(h)_{XY,YX}$ are generally negligible as their magnitude is close to 0 MN/m. Both the HBFM and NHBFM deliver the same predicted $\text{Ima}(h)_{XX,YY}$ for the test seal.

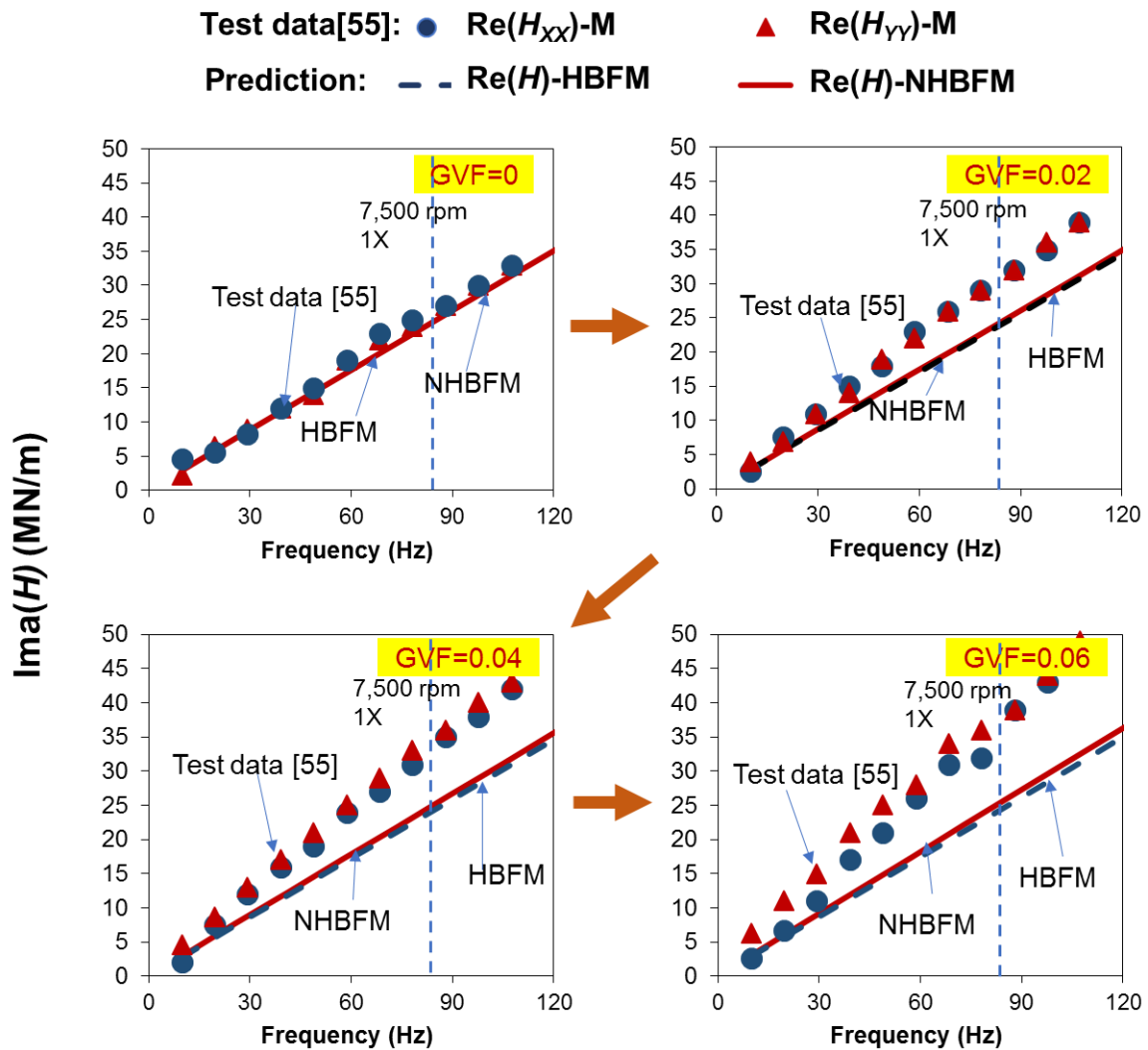


Figure 15 Imaginary part of complex dynamic stiffness, $Ima(H)_{xx,yy}$, versus excitation frequency. Shaft speed 7,500 rpm (150 HZ), seal inlet pressure 44.8 bara, discharge pressure 6.9 bara. Symbols: test data in Ref.[55], Solid line: prediction from NHBFM. Broken line: prediction from HBFM.

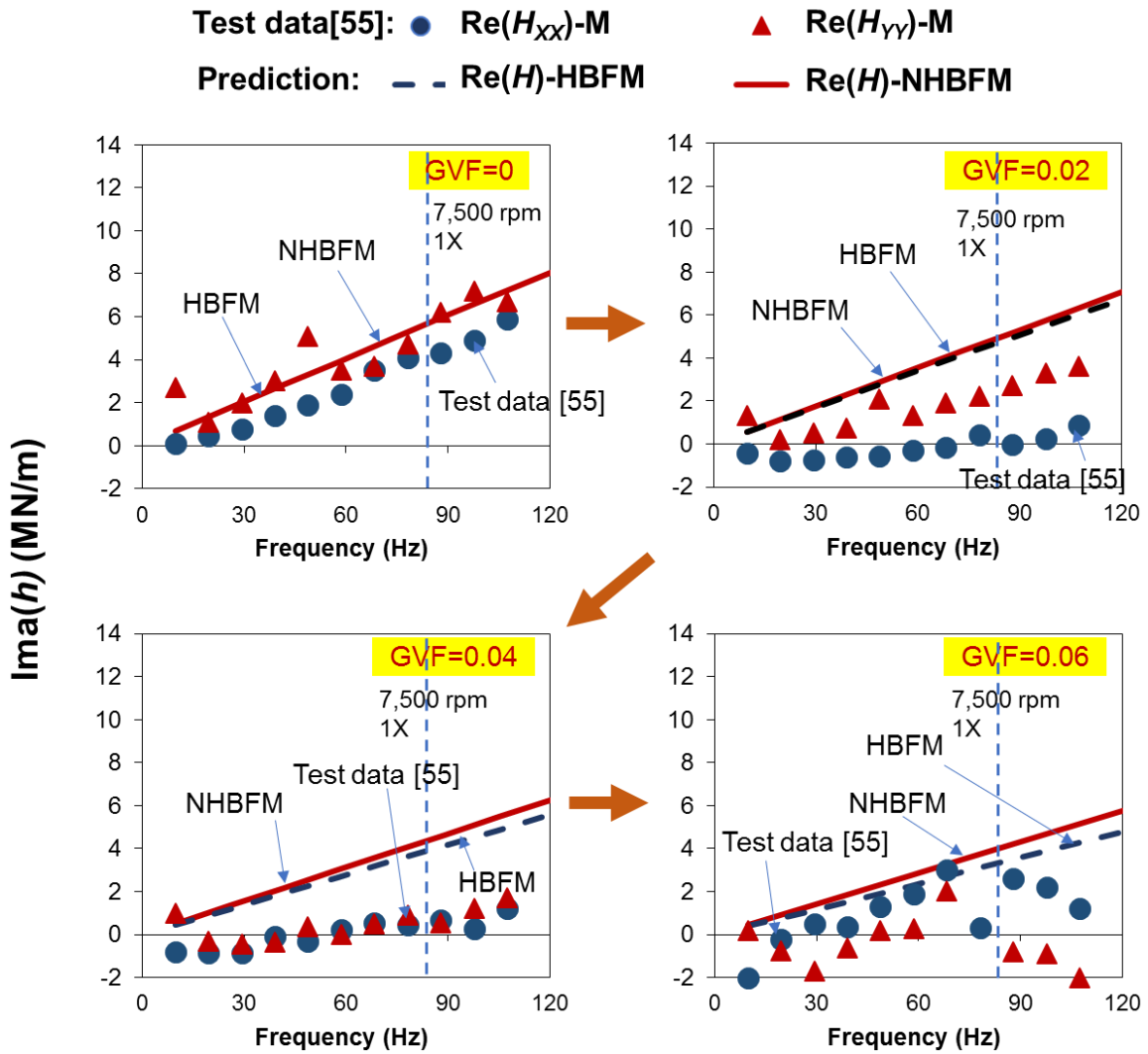


Figure 16 Imaginary part of cross-coupled complex dynamic stiffness, $\text{Ima}(H)_{xy,yx}$, versus excitation frequency. Shaft speed 7,500 rpm (150 HZ), seal inlet pressure 44.8 bara, discharge pressure 6.9 bara. Symbols: test data in Ref.[55], Solid line: prediction from NHBFM. Broken line: prediction from HBFM.

Recall that if the rotordynamic coefficients are frequency independent, the seal can be characterized by a (K, C, M) model [5]. Presently, the direct and cross-coupled stiffness (K, k) , virtual mass (M, m) , and damping coefficients (C, c) are obtained from curve fits of the real and imaginary parts of the complex dynamic stiffness (H) , i.e., $\text{Re}(H) \leftarrow K - \omega^2 M$, $\text{Re}(h) \leftarrow k - \omega^2 m$, $\text{Ima}(H) \leftarrow \omega C$, and $\text{Ima}(h) \leftarrow \omega c$.

Figure 17 through 22 show the measured [55] and predicted seal dynamic force coefficients versus inlet GVF. The symbols represent test data, the solid lines represent predictions from the current NHBFM, and the broken lines stand for predictions based on the HBFM [10]. On the bottom of each graph, there is a table detailing the correlation coefficient R^2 of the curve fit to the test data.

Figure 17 shows the measured and predicted seal direct stiffness (K) versus inlet GVF. Note that both the homogeneous bulk flow model (HBFM) [10] and the current nonhomogeneous bulk flow model (NHBFM) predict a drop in K as the inlet GVF increases from 0 to 10%. However, K predicted by the NHBFM has a larger slope compared to that from a HBFM.

Figure 18 shows the direct mass coefficient (M) versus inlet GVF. The NHBFM predicts a slightly larger M compared to the HBFM does. Both the test data and prediction show that the cross-coupled mass (m) is negligible, thus, m is not discussed here. Figure 19 shows the measured and predicted cross-coupled stiffness (k) versus inlet GVF. Both models predict similar k (in magnitude). The largest difference between the NHBFM and HBFM predicted k occurs at inlet GVF=0.1, with a ~10% difference.

Figure 20 shows the direct damping coefficients $C \leftarrow \text{Ima}(H)/\omega$. Although both

models under predict the damping coefficients (C), the models do predict a correct trend that the predicted damping coefficients increase with GVF.

The whirl frequency ratio (f_w) determines at which frequency the seal will become destabilizing to a rotor system. San Andrés [56] points out that fluid inertia effects reduce the stability of a rotor-bearing system, and develops an equation to calculate the whirl frequency ratio for operation at the concentric positions:

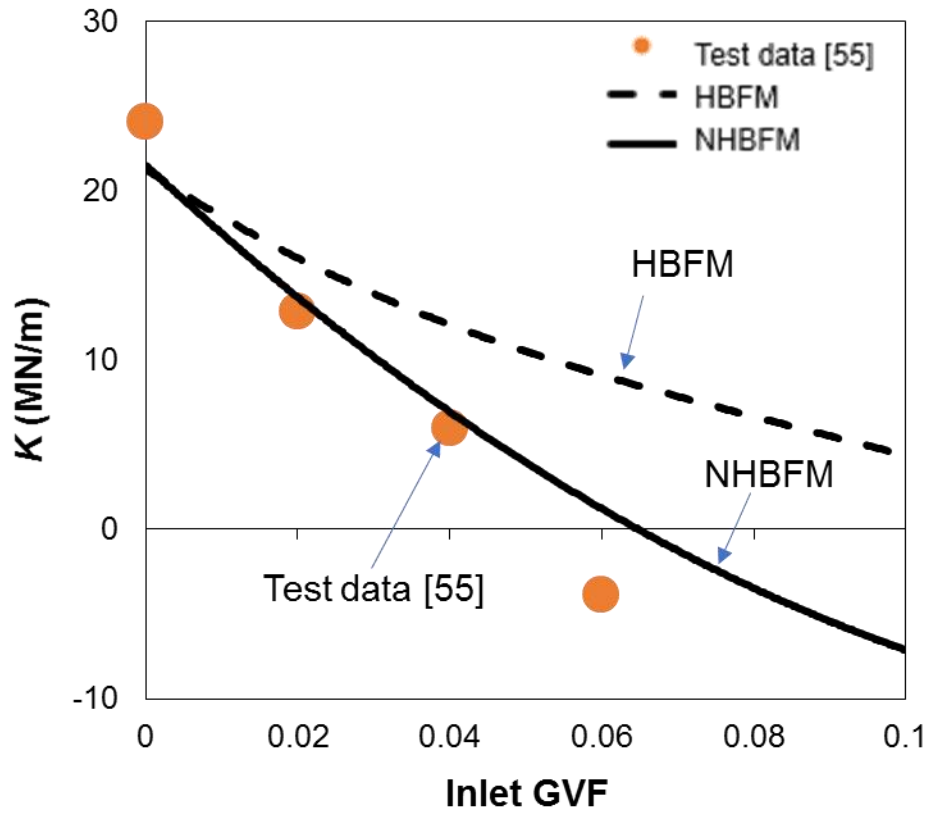
$$f_w^2 \Omega_s^2 M_{xy} + f_w \Omega_s C_{xx} - k_{xy} = 0 \quad (88)$$

Recall that the test seal in Ref. [55] shows a nil cross-coupled mass coefficient $m = M_{XY}$.

Thus, Eq. (86) reduces to

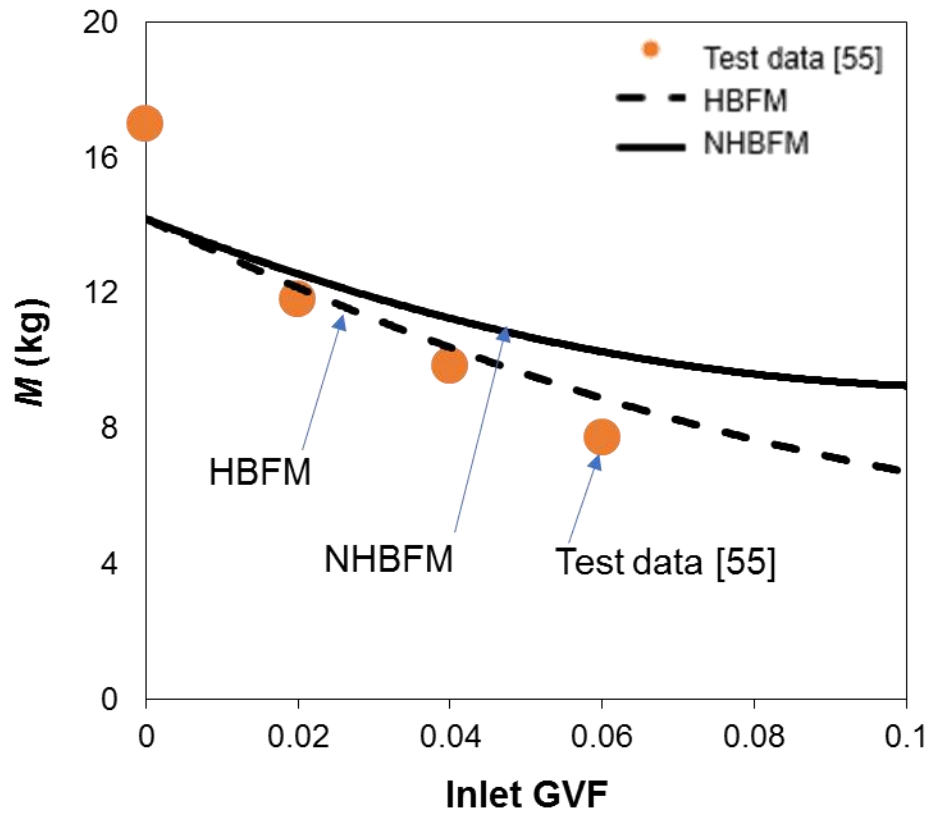
$$f_w = \frac{k}{\Omega_s C} \quad (89)$$

Figure 22 shows the predicted and experimentally estimated seal whirl frequency ratio (f_w) versus inlet GVF. For operation with a pure liquid the seal shows a whirl frequency ratio $f_w = 0.28$. For operation with a mixture f_w increases to ~ 0.38 . Both the NHBFM and the HBFM accurately predict f_w , as compared to the test data in Ref. [55].



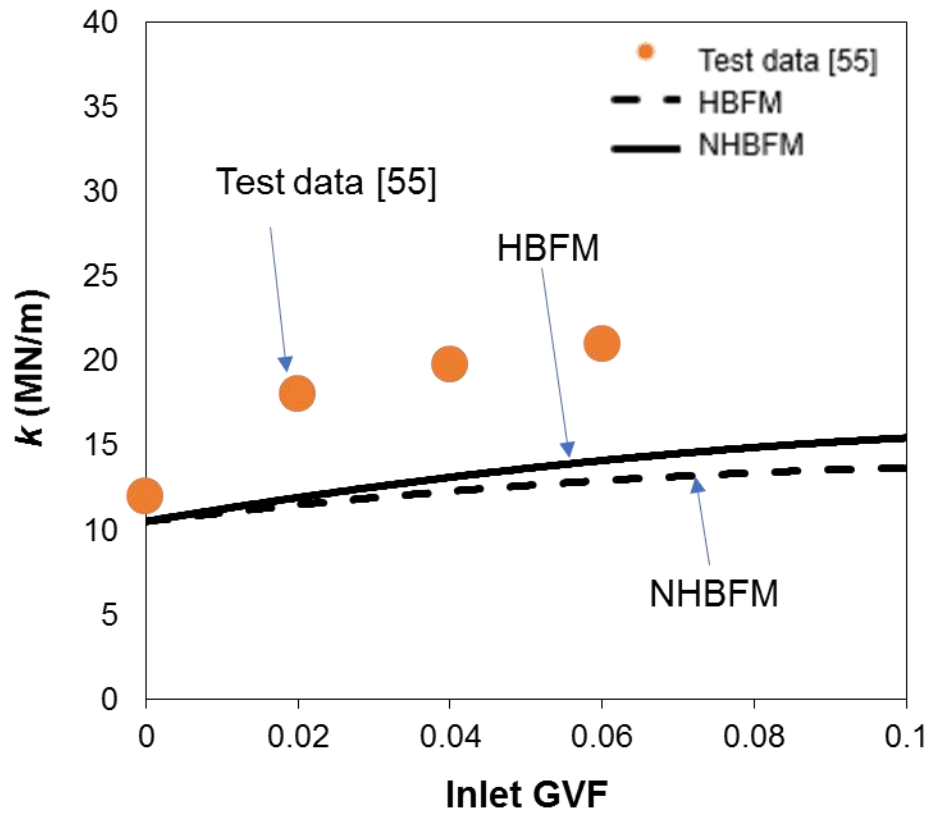
Inlet GVF	R ² of curve fit for test data [55]
0	0.96
0.02	0.87
0.04	0.85
0.06	0.76

Figure 17 Direct stiffness (K) versus inlet GVF. Shaft speed 7,500 rpm, seal inlet pressure 44.8 bara, discharge pressure 6.9 bara. Symbols: test data in Ref.[55], Solid line: prediction from NHBFM. Broken line: prediction from HBFM.



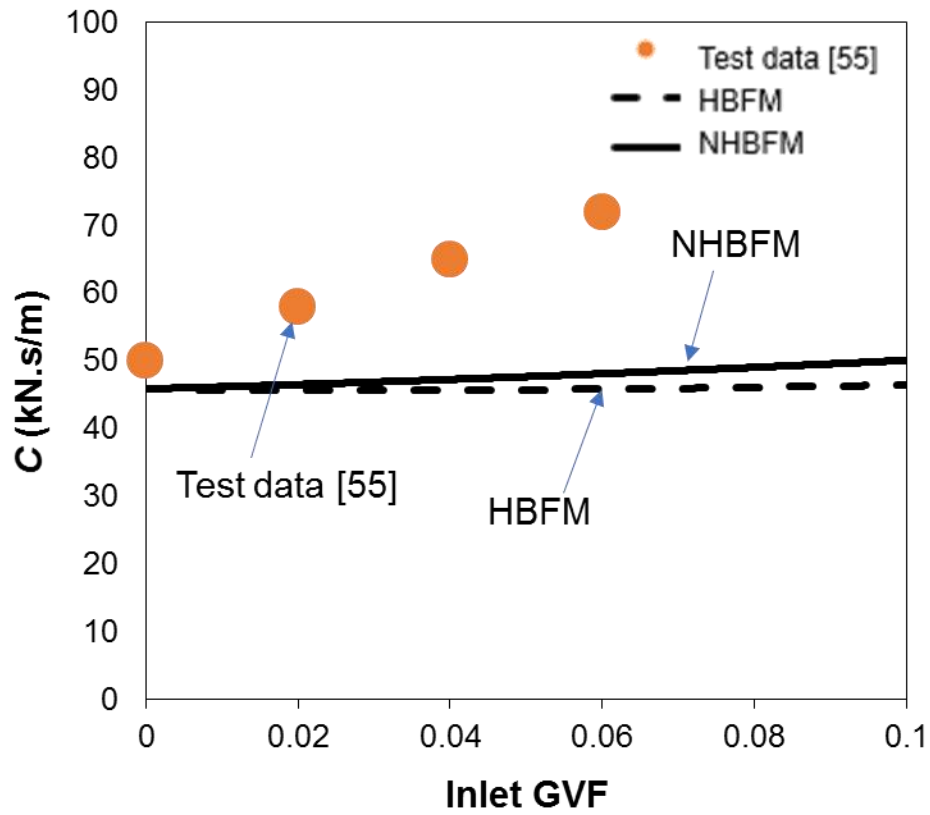
Inlet GVF	R ² of curve fit for test data [55]
0	0.96
0.02	0.87
0.04	0.85
0.06	0.76

Figure 18 Direct mass (M) versus inlet GVF. Shaft speed 7,500 rpm, seal inlet pressure 44.8 bara, discharge pressure 6.9 bara. Symbols: test data in Ref.[55], Solid line: prediction from NHBFM. Broken line: prediction from HBFM.



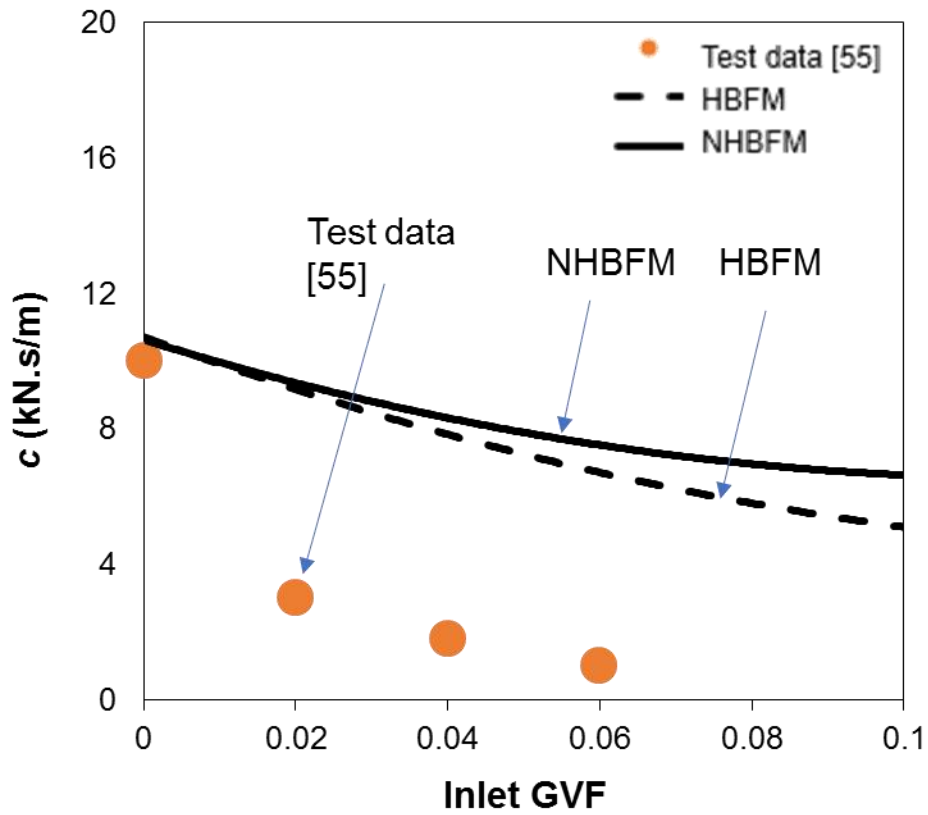
Inlet GVF	R ² of curve fit for test data [55]
0	0.99
0.02	0.99
0.04	0.97
0.06	0.96

Figure 19 Cross-coupled stiffness (k) versus inlet GVF. Shaft speed 7,500 rpm, seal inlet pressure 44.8 bara, discharge pressure 6.9 bara. Symbols: test data in Ref.[55], Solid line: prediction from NHBFM. Broken line: prediction from HBFM.



Inlet GVF	R ² of curve fit for test data [55]
0	0.99
0.02	0.99
0.04	0.99
0.06	0.99

Figure 20 Direct damping (C) versus inlet GVF. Shaft speed 7,500 rpm, seal inlet pressure 44.8 bara, discharge pressure 6.9 bara. Symbols: test data in Ref.[55], Solid line: prediction from NHBFM. Broken line: prediction from HBFM.



Inlet GVF	R ² of curve fit for test data [55]
0	0.85
0.02	0.45
0.04	0.42
0.06	0.32

Figure 21 Cross-coupled damping (c) versus inlet GVF. Shaft speed 7,500 rpm, seal inlet pressure 44.8 bara, discharge pressure 6.9 bara. Symbols: test data in Ref.[55], Solid line: prediction from NHBFM. Broken line: prediction from HBFM.

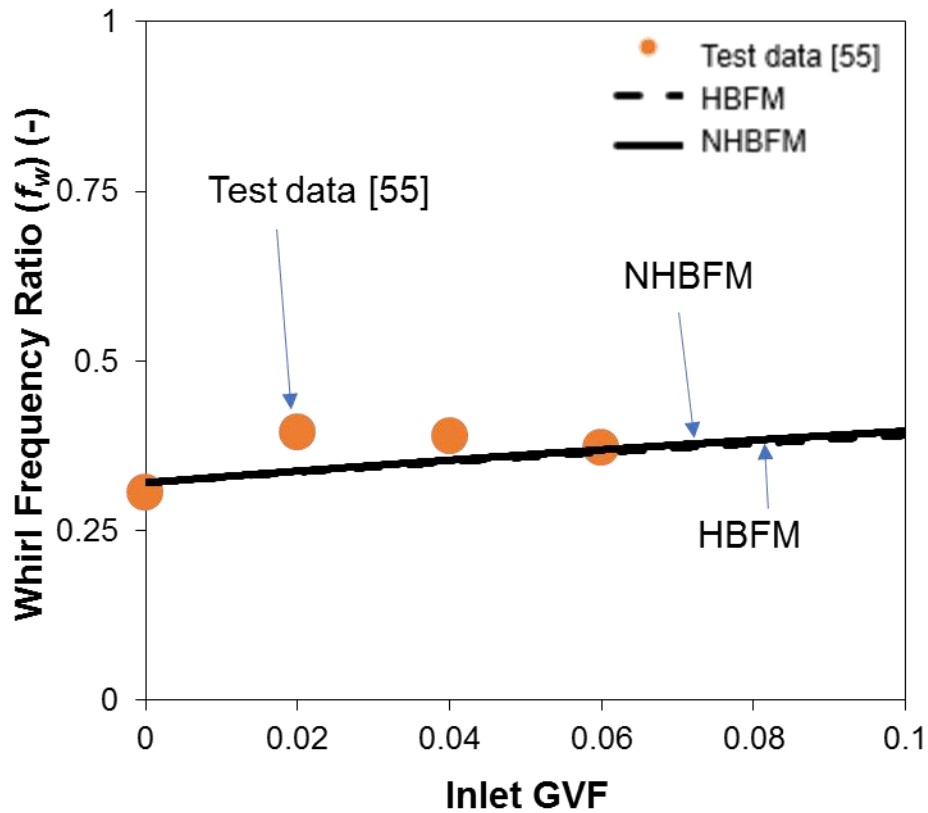


Figure 22 Whirl frequency ratio (f_w) versus inlet GVF. Shaft speed 7,500 rpm, seal inlet pressure 44.8 bara, discharge pressure 6.9 bara. Symbols: test data in Ref.[55], Solid line: prediction from NHBFM. Broken line: prediction from HBFM.

Appendix D shows predicted and measured force coefficients of one other seal tested by Zhang and Childs [55]. The seal has a nominal diameter $D = 89.3$ mm, length $L = 57.8$ mm ($L/D = 0.65$), and a radial clearance $c = 0.163 \pm 0.005$ mm. Comparisons of the predicted force coefficients against the test data for the third seal reinforces the current finding that the NHBFM predicted $Re(H)$ reduces faster with inlet GVF than that predicted by the HBFM.

4.2. Low pressure annular seal

Table 3 lists the dimensions and fluids physical properties of the low pressure seal tested by Lu and San Andrés [11] in 2018. The seal has a diameter (D) 127 mm, length (L) 46 mm and uniform radial clearance (c) 0.274 mm. The operating condition includes a supply pressure = 2.6 ± 0.1 bara, discharge pressure = 1 bara, and shaft speed = 3,500 rpm ($\Omega R = 23.3$ m/s). The lubricant is air in ISO VG10 mineral oil. Ref. [11] details the description of the test rig and the experimental procedure.

Table 3. Dimensions of test uniform clearance annular seal and fluids physical properties [11].

Diameter, $D = 2R$	127 mm
Length, L	46 mm
Radial Clearance c	0.274 \pm 0.005mm
ISO VG10 Oil viscosity, μ_l	9.8 cP (38 °C)
Density, ρ_l	875 kg/m ³
Air viscosity, μ_{ga}	0.018 cP (20 °C)
Density, ρ_{ga}	1.14 kg/m ³ at $P_a = 1$ bara
Supply pressure	2.6 \pm 0.1 bara
Discharge pressures	1 bara
Journal speed, Ω_{\max}	3.5 krpm
Rotor surface speed, $\frac{1}{2}D\Omega_{\max}$	23.3 m/s

Figure 23 shows the measured and predicted seal mass flow rate versus inlet GVF. The symbols represent test data, the solid lines represent predictions from the current NHBFM, and the broken lines stand for predictions based on the HBFM [10]. The model utilizes Eq. (33a) for the viscosity of the mixture offers accurate predictions for the mass

flow rate. The model using Eq.(33b) (gas volume fraction averaged viscosity) underestimates the leakage by ~20% at inlet GVF of 0.2, as seen in Figure 23. Note that that as the inlet GVF increases from 0 (pure liquid) to a mixture with inlet GVF of 20%, the measured leakage reduces by ~10%. Both the current NHBFM and the HBFM accurately predict the seal leakage.

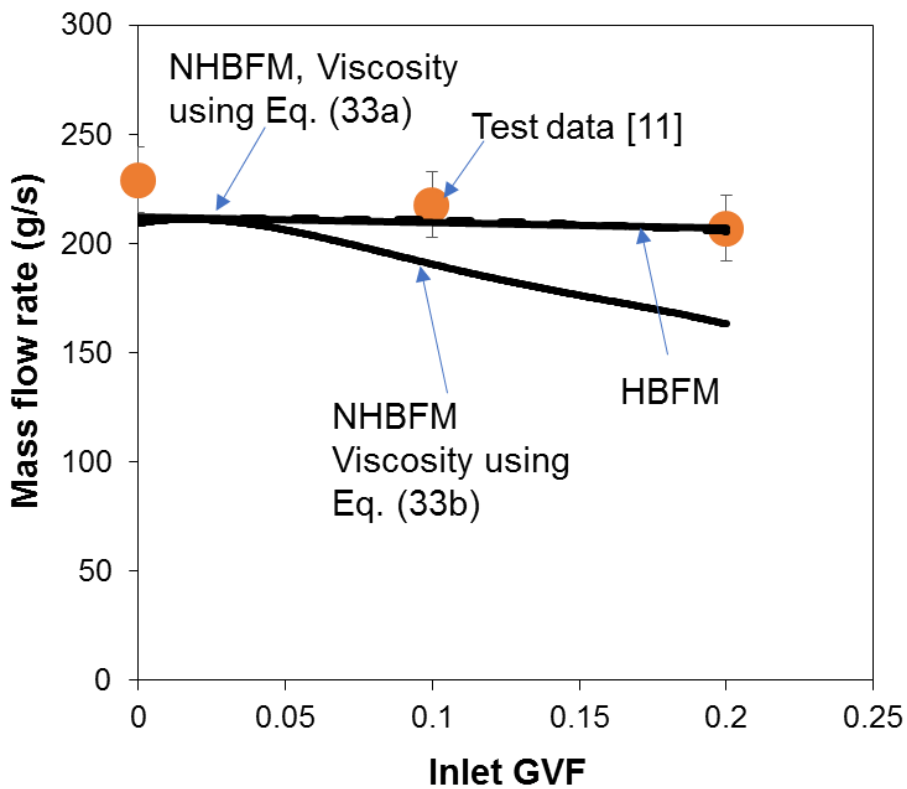


Figure 23 Low pressure seal mass flow rate versus inlet GVF. Shaft speed 3,500 rpm, seal inlet pressure = 2.6 ± 0.1 bara, discharge pressure = 1 bara. Symbols: test data in Ref.[11], Solid line: prediction from NHBFM. Broken line: prediction from HBFM.

Table 4 lists the axial, circumferential and bulk flow Reynolds numbers Re_{mz} , Re_{mc} , Re_{ms} , respectively. As the inlet GVF increases from 0 to 0.2, the maximum bulk flow Reynolds number reduces from 291 to 281. Thus, the flow is in laminar Regime.

Table 4. Calculated flow Reynolds number at the inlet and exit planes of test seal in Ref. [11].

GVF		GMF‰		Re_{mz}		Re_{mc}		Re_{ms}	
inlet	Exit	Inlet	Exit	inlet	exit	inlet	exit	inlet	exit
0	0	0		59	59	285	285	291	291
0.1	0.22	0.38		60	69	277	272	284	281
0.2	0.39	0.85		63	86	273	266	281	279

Figure 24 shows the experimentally estimated and NHBFM and HBFM predicted complex dynamic stiffnesses (H, h) versus excitation frequency (ω). The symbols represent test data, the solid lines represent predictions from the current NHBFM, and the broken lines stand for predictions based on the HBFM [10]. The graphs in the first row show $Re(H)$. Note that the NHBFM predicts a $Re(H)$ that matches well the test data. The HBFM generally under predicts the inertia effect.

Recall that in Eqs. (24) and (25) the diffusion coefficients ($r_1, r_2, r_3,$ and r_4) mainly affect the inertia terms in the momentum equations of the NHBFM. Thus, the NHBFM predicts a larger added mass compared to the added mass predicted from the HBFM. Note that in the high pressure seal (shown in Figure 18), the NHBFM delivers a larger M compared to the HBFM as well.

The graphs in the second row show $Re(h)$. The HBFM offers more accurate prediction compared to the NHBFM, in particular that $Re(h)$ grows with frequency for operation with a mixture. On the other hand, the NHBFM predicts a $Re(h)$ that is constant with frequency.

The graphs in the third row show $Ima(H)$ that increases linearly with frequency. Both the HBFM and NHBFM offer good prediction in $Ima(H)$. Both the test data and

predictions show that the $Ima(H)$ is a lineal function of frequency for operation with an inlet GVF up to 20% .

Lastly, the graphs in the fourth row show $Ima(h)$. As the graphs shown, the NHBFM offers a better prediction in $Ima(h)$. The HBFM largely under predicts $Ima(h)$. For better comparison, Figure 25 to 31 show the force coefficients estimated from (H and h).

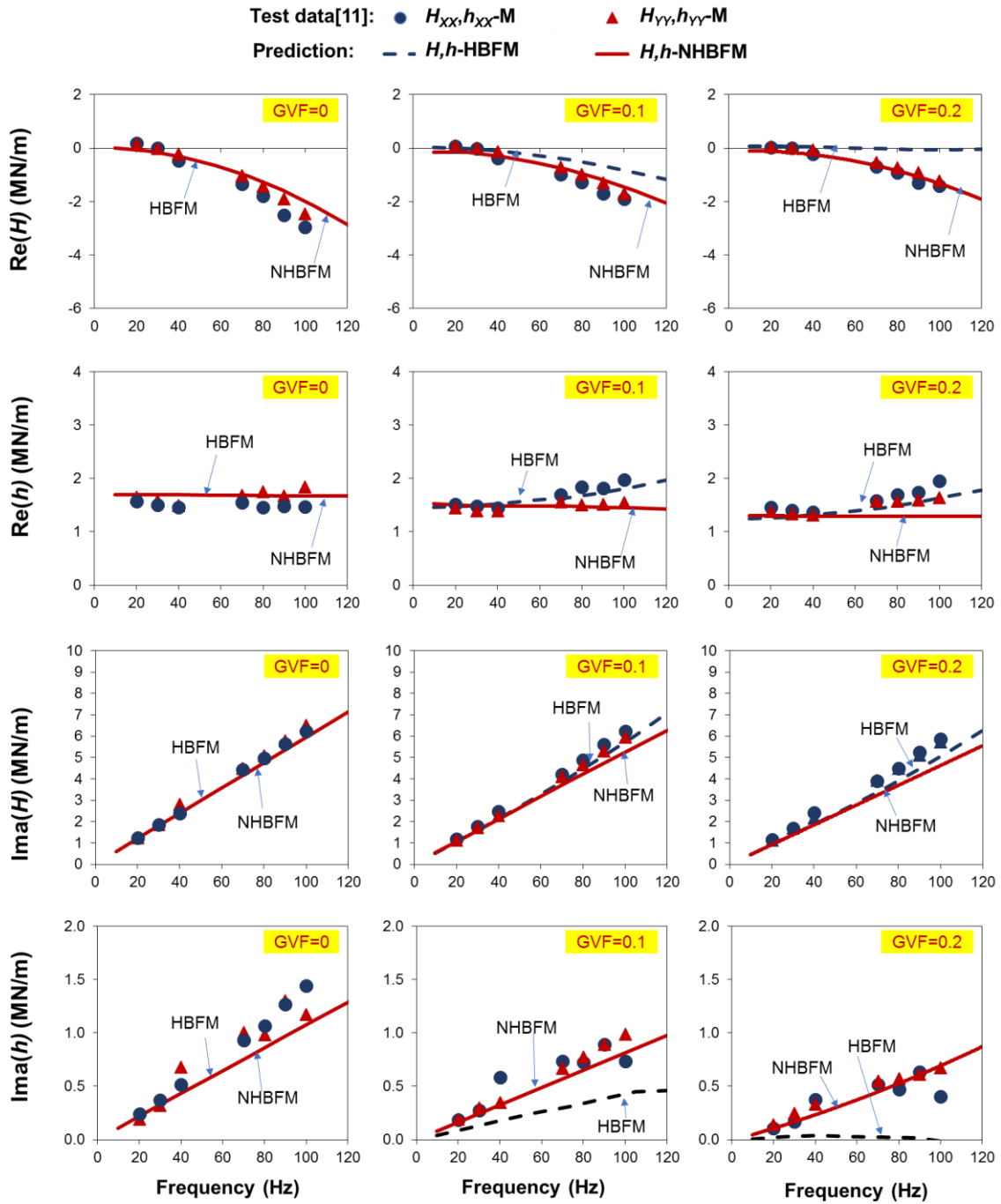


Figure 24 Complex dynamic stiffnesses (H, h) versus excitation frequency for a low pressure uniform clearance annular seal. Shaft speed 3,500 rpm (58.3 HZ), seal inlet pressure 2.6 ± 0.1 bara, discharge pressure 1 bara. Symbols: test data in Ref.[11], Solid line: prediction from NHBFM. Broken line: prediction from HBFM.

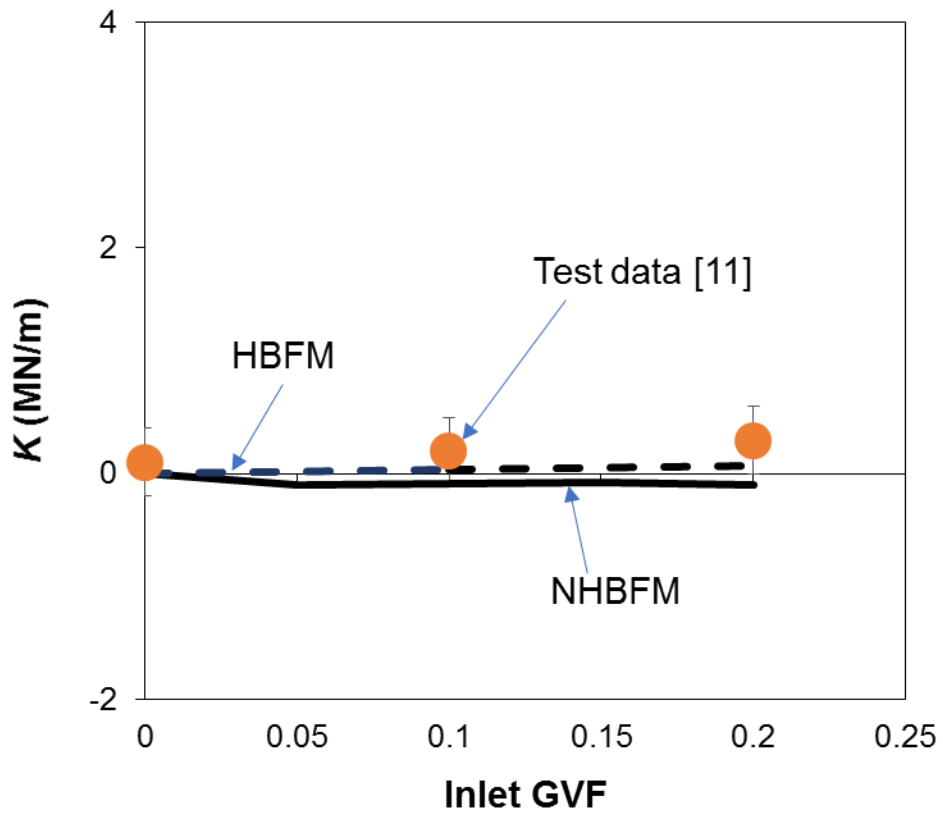
Figure 25 to 30 show the measured and predicted rotordynamic force coefficients versus inlet GVF. The symbols represent test data [11], the solid lines represent predictions from the current NHBFM, and the broken lines stand for predictions based on the HBFM [10]. On the bottom of each graph, there is a table detailing the R^2 of curve fit for the test data.

Figure 25 shows the direct stiffness (K) versus inlet GVF. Due to the low supply pressure ($P_s = 2.6$ bara), the direct stiffness (K) is small in magnitude. Both the NHBFM and the HBFM predicts a $K \sim 0$ MN/m.

Figure 26 shows the added mass coefficient (M). The NHBFM predicted added mass is larger than the one predicted from the HBFM. As the inlet GVF increases, both models predict a quick reduction of inertia coefficient. The NHBFM predicted added mass is larger than that predicted by the HBFM.

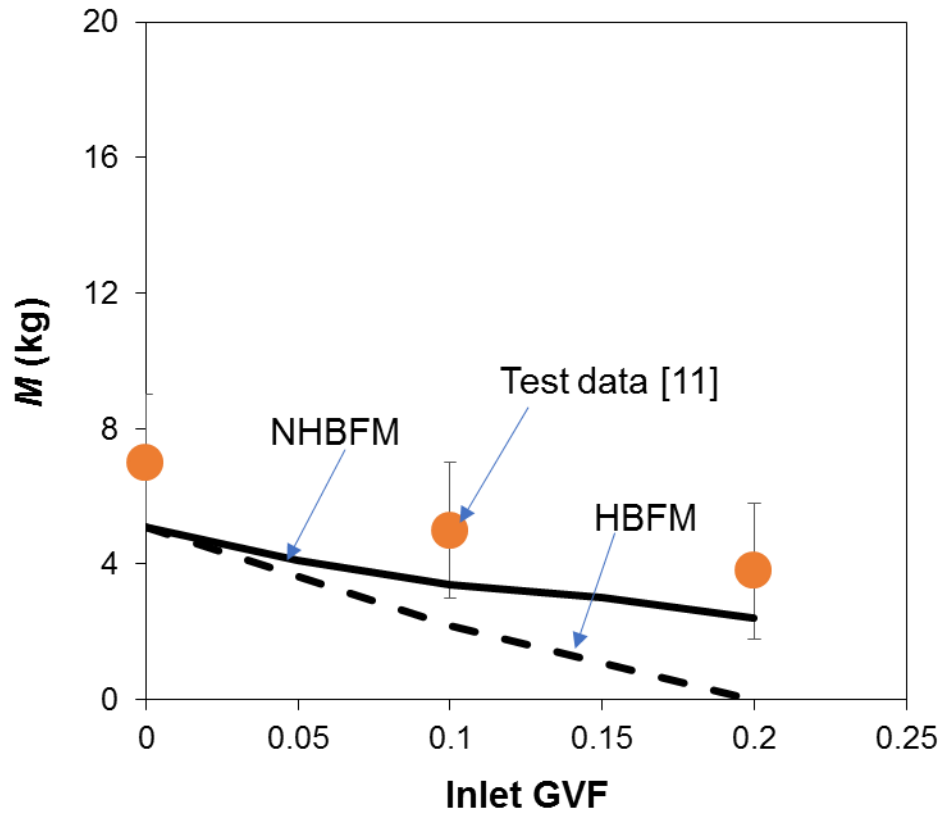
Figure 27 shows the measured and predicted cross-coupled stiffness (k). Both models offer accurate prediction in k . Figure 28 and 27 depict the direct damping (C) and cross-coupled damping coefficients (c). Note that both the experimentally estimated and predicted C and c reduce in magnitude with an increase in inlet GVF.

Figure 30 shows the predicted and experimentally estimated seal whirl frequency ratio (f_w) versus inlet GVF. For operation with either a pure liquid or a two-phase flow, both the test data and predictions show the seal whirl frequency ratio (f_w) is close to 0.5, a typical whirl frequency ratio for laminar flow annular seals.



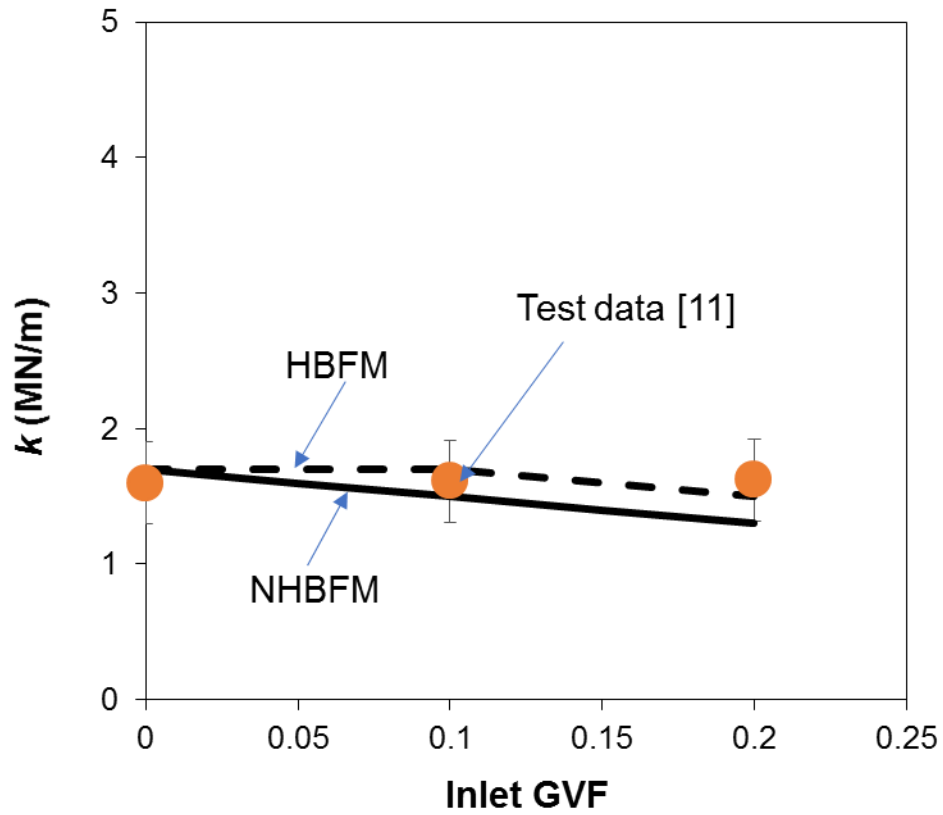
Inlet GVF	R ² of curve fit for test data [11]
0	0.99
0.1	0.99
0.2	0.98

Figure 25 Low pressure seal, direct stiffness (K) versus inlet GVF. Shaft speed = 3,500 rpm, seal inlet pressure = 2.6 ± 0.1 bara, discharge pressure = 1 bara. Symbols: test data in Ref.[11], Solid line: prediction from NHBFM. Broken line: prediction from HBFM.



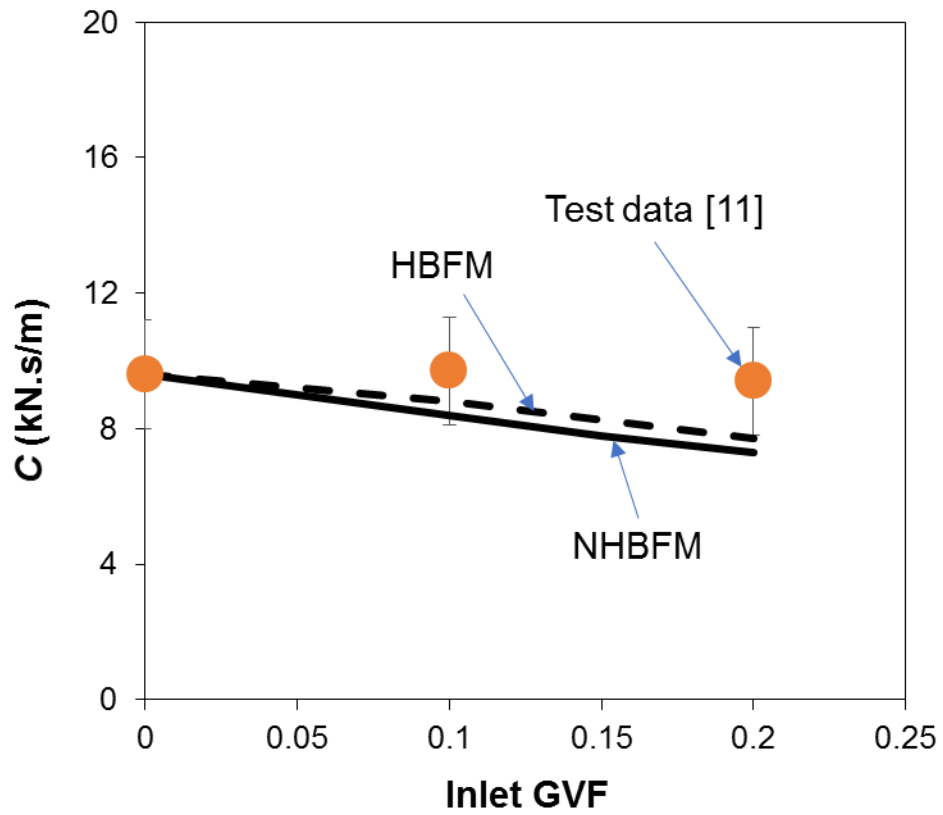
Inlet GVF	R ² of curve fit for test data [11]
0	0.99
0.1	0.99
0.2	0.98

Figure 26 Low pressure seal, direct mass (M) versus inlet GVF. Shaft speed 3,500 rpm, seal inlet pressure = 2.6 ± 0.1 bara, discharge pressure = 1 bara. Symbols: test data in Ref.[11], Solid line: prediction from NHBFM. Broken line: prediction from HBFM.



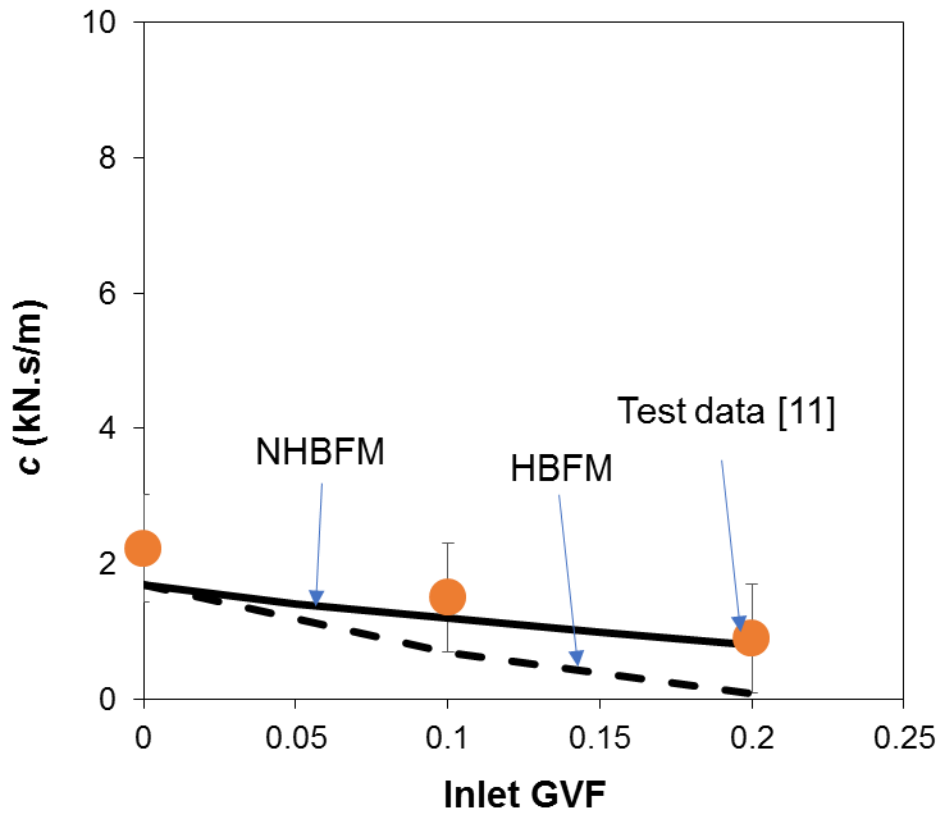
Inlet GVF	R ² of curve fit for test data [11]
0	0.90
0.1	0.86
0.2	0.93

Figure 27 Low pressure seal, cross-coupled stiffness (k) versus inlet GVF. Shaft speed = 3,500 rpm, seal inlet pressure = 2.6 ± 0.1 bara, discharge pressure = 1 bara. Symbols: test data in Ref.[11], Solid line: prediction from NHBFM. Broken line: prediction from HBFM.



Inlet GVF	R ² of curve fit for test data [11]
0	0.99
0.1	0.99
0.2	0.99

Figure 28 Low pressure seal, direct damping (C) versus inlet GVF. Shaft speed = 3,500 rpm, seal inlet pressure = 2.6 ±0.1 bara, discharge pressure = 1 bara. Symbols: test data in Ref.[11], Solid line: prediction from NHBFM. Broken line: prediction from HBFM.



Inlet GVF	R ² of curve fit for test data [11]
0	0.99
0.1	0.96
0.2	0.43

Figure 29 Low pressure seal, cross-coupled damping (c) versus inlet GVF. Shaft speed = 3,500 rpm, seal inlet pressure = 2.6 ± 0.1 bara, discharge pressure = 1 bara. Symbols: test data in Ref.[11], Solid line: prediction from NHBFM. Broken line: prediction from HBFM.

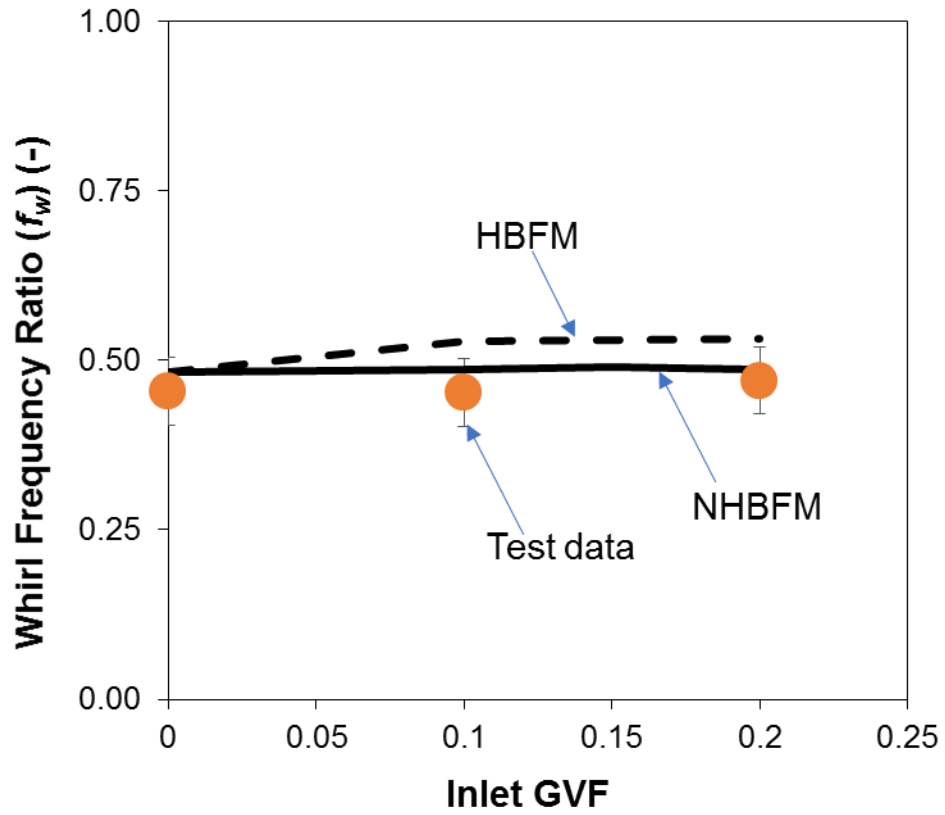


Figure 30 Whirl frequency ratio (f_w) versus inlet GVF. Shaft speed = 3,500 rpm, seal inlet pressure = 2.6 ± 0.1 bara, discharge pressure = 1 bara. Symbols: test data in Ref.[11], Solid line: prediction from NHBFM. Broken line: prediction from HBFM.

4.3. Closure

This section presented predictions on the leakage and force coefficients for two-phase flow annular seals operating under a two-phase flow condition. Predictions for the high pressure seal flow filed show that when operating with a two-phase flow the maximum diffusion velocity (velocity difference between the liquid and gas components) occurs at the seal exit plane. The maximum diffusion velocity is only about ~0.1% of the liquid flow velocity, indicating that the flow is mostly homogeneous.

Thus, both the NHBFM and HBFM [10] predict similar static pressure and gas volume fraction profiles. Therefore, both models predict similar seal leakage (mass flow rate) and shear drag torque. The comparisons of the predicted results against the test data in Refs. [55] and [11] show that both the NHBFM and HBFM can accurately predict seal leakage.

The NHBFM contains a first order transport equation for the first order gas volume fraction (α_{gY}), from which the first order mixture density (ρ_{mY}) is derived. In the HBFM in Ref. [10], ρ_{mY} is a function of the mixture gas volume fraction and the mixture bulk modulus.

A study on the first order gas volume fraction, mixture density and pressure (α_{gY} , ρ_{mY} , P_Y) uncovers that the difference in the modeling of ρ_{mY} between the two models leads to a change in first order pressures (P_Y), in particular the phase angle between h_Y and $\text{Re}(P_Y)$. However, the phase angle between h_Y and $\text{Ima}(P_Y)$ is less affected. Thus, the two models deliver force coefficients with a major difference in $\text{Re}(H)$ that produces the direct stiffness coefficient.

5. CONCLUSION

In turbomachinery, annular clearance seals such as balance pistons, impeller eye seals, and inter-stage seals restrict leakage from a high pressure zone to a low pressure zone. When operating with a two-phase flow, seals show different performance in leakage and dynamic force coefficients compared to those of the same seal working with a pure liquid [11,12]. The variation of seal force coefficients with gas volume fraction (GVF) may cause rotor asynchronous vibrations in a multiphase pump [4].

Based on the algebraic slip mixture model theory (ASMM) [41, 43], this report advances a novel nonhomogeneous bulk flow mode (NHBFM) for the prediction of the static and dynamic forced performance of two-phase flow annular seals. The NHBFM contains a first order transport equation for the first order gas volume fraction (α_{gY}), from which the first order mixture density (ρ_{mY}) is obtained, see Eq.(80). In a HBFM in Ref. [10], ρ_{mY} is a function of the bulk modulus and volume fraction of the two components, see Eq. (86).

Direct comparisons of the predictions against test data obtained for two high pressure seals in Ref. [55] and a low pressure seals in Ref. [11] serve to validate the NHBFM. The high pressure seals (seals 1 and 2) in Ref. [55] are supplied with a $P_s = 44.8$ bara and a discharge pressure $P_a = 6.9$ bara. The seals have the same diameter $D = 89.3$ mm and length $L = 57.8$ mm ($L/D = 0.65$), but different radial clearances, i.e., $c = 0.140 \pm 0.005$ mm and 0.163 ± 0.005 mm, respectively. The mixture consists of air and synthetic oil with a viscosity 4.53 cP at 40 °C and a density of 899 kg/m³. The flow Reynolds number is

within the range of 870 to 1,100, representing a laminar flow.

The low pressure seal (seal 3) operates with a supply pressure $P_s = 2.6$ bara and discharge pressure $P_a = 1$ bara. The seal has a diameter $D = 127$ mm, length $L = 46$ mm ($L/D = 0.36$) and radial clearance $c = 0.274 \pm 0.005$ mm. and the lubricant is air in ISO VG10 mineral oil. The inlet GVF increases from 0 to 0.2, and the flow is in laminar flow regime as the maximum Reynolds number is less than 300.

The major conclusions from this work are as follows.

For comparisons to high pressure seals 1 and 2 (described above):

- a) For the test seal in Ref. [55] the flow is mostly homogeneous because the maximum diffusion velocity that occurs at the seal exit plane is only $\sim 0.1\%$ of the liquid flow velocity. Thus, compared to a HBFM in Ref.[10] the NHBFM predicts similar results in static pressure, gas volume fraction profile, leakage (mass flow rate) and shear drag torque. The difference between the NHBFM and HBFM predicted leakage and test data in Refs. [55] and [11] is less than 5%.
- b) The two models predict different first order pressure fields (P_Y), in particular the phase angle between h_Y and $\text{Re}(P_Y)$. The phase angle between h_Y and $\text{Ima}(P_Y)$ is less affected. A study for a seal in Ref.[55] shows that as the inlet GVF increases from 0 to 0.1, the phase angle between $\text{Re}(P_Y)$ and h_Y reduces from 141.3° to 68.5° as predicted by the NHBFM, and from 141.3° to 96.5° as predicted by the HBFM. Thus, the NHBFM predicted $\text{Re}(H)$ decreases more with inlet GVF than that predicted by the HBFM.
- c) The NHBFM delivers a larger added mass (M) than the HBFM does. For operation

with a high pressure ($P_s = 44.8$ bara), the maximum difference in M between the two models is about 30% for operation with inlet GVF=0.1.

- d) Because the imaginary part of the first order pressures as predicted from both models is very similar in magnitude and phase, the NHBFM and HBFM predict a similar direct damping coefficient (C), with a maximum difference of ~5%. Compared to the test data in Ref. [55], the two models generally under predict C by 25%.
- e) Both the NHBFM and the HBFM predict similar cross-coupled stiffness, with a difference about 5%. Compared to the test data in Ref. [55], the two models generally under predict cross-coupled stiffness k by 25%.
- f) Both the NHBFM and HBFM deliver accurate predictions in whirl frequency ratio (WFR). For example, both models predict a $WFR \sim 0.3$ for the high pressure seal. As the inlet GVF increases from 0 to 0.1, the WFR increases from ~0.3 to ~0.35.
- g) Comparison of the predicted force coefficients against the test data for a third seal in Ref. [55] and shown in Appendix D reinforces the above conclusions, in particular that the NHBFM predicted $Re(H)$ reduces faster with inlet GVF than the one predicted by the HBFM.

For comparisons to low pressure seal 3 (described above):

- h) Both the NHBFM and HBFM predict similar mass flow rates that match closely with test data in Ref. [11].
- i) Both models predict ~ 0 direct stiffness (K) due to the low pressure (2.6 bara).
- j) The NHBFM predicted M is 3.2 kg, about ~30 % below the test data 4 kg. The

HBFM predicts a zero added mass at inlet GVF=0.2.

- k) Both the NHBFM and the HBFM predict similar cross-coupled stiffness, with a difference about 5%. Compared to the test data in Ref. [11], the two models generally accurately predict the cross-coupled stiffness within uncertainty.
- l) Both the NHBFM and HBFM predict similar damping (C), with a maximum difference of ~5%. Compared to the test data in Ref. [11], the two models generally under predict C by 25% at inlet GVF = 0.2.
- m) Both the NHBFM and HBFM deliver accurate predictions in whirl frequency ratio (WFR). WFR remains at ~0.5 for operation with a mixture.

In contrast to commercial computational fluid dynamics (CFD) software packages that require days to obtain the dynamics force coefficients for a single operation condition, the current NHBFM only takes one or two minutes to complete the prediction. Thus, the NHBFM is very computational efficient.

In this work, the overall Reynolds number $Re_{ms} < 1,100$. However, many seals do operate with turbulent flow ($Re > 2,000$). Computational fluid dynamics (CFD) analysis could help to extract the friction factors for operation with a turbulent flow condition to calibrate the NHBFM.

The current model is valid for uniform clearance seals. However, high performance multiphase pumps favor grooved seals to further reduce leakage and also damper seals (i.e., hole pattern seals) to promote rotor dynamic performance. One of future advancement is to apply the current NHBFM to grooved seals and damper seals.

REFERENCES

- [1] Liu, P., Patil, A., and Morrison, G., 2018, "Multiphase Flow Performance Prediction Model for Twin-Screw Pump," *ASME J. Fluids Eng.*, **140**, p. 031103.
- [2] Vannini, G., Bertoneri, M., Del Vescovo, G., and Wilcox, M., 2014, "Centrifugal Compressor Rotordynamics in Wet Gas Conditions," *Proc. 43rd Turbomachinery & 30th Pump Users Symposia*, Houston, TX, September 23-25.
- [3] Bibet, P. J., Klepsvik, K. H., Lumpkin, V. A., and Grimstad, H., 2013, "Design and Verification Testing of a New Balance Piston for High Boost Multiphase Pumps," *Proc. 42th Turbomachinery & 29th International Pump Users Symposia*, Houston, TX, October 1-3. <http://hdl.handle.net/1969.1/162569>.
- [4] Ekeberg, I., Bibet, P., Knudsen, H., Torbergesen, E., Kjellnes, H.F., Angeltveit, R., and Klepsvik, K., 2018, "Design and Verification Testing of Balance Piston for High-Viscosity Multiphase Pumps," *Proc. 47th Turbomachinery & 34th International Pump Users Symposia*, Houston, TX, September 17-20. <http://hdl.handle.net/1969.1/175008>.
- [5] Childs, D.W., 1993, *Turbomachinery Rotordynamics: Phenomena, Modeling, & Analysis*, John Wiley & Sons, INC, New York, NY.
- [6] Hirs, G.G., 1973, "A Bulk-Flow Theory for Turbulence in Lubricant Films," *ASME J. Lubr.Technol.*, April, 1973, pp. 137-145.
- [7] Childs, D.W., 1983, "Dynamic Analysis of Turbulent Annular Seals Based on Hirs' Lubrication Equation," *ASME J. Lubr.Technol.*, **105**, pp. 429-436.
- [8] Childs, D.W., 1983, "Finite-Length Solutions for Rotordynamic Coefficients of Turbulent Annular Seals," *ASME J. Lubr.Technol.*, **105**, pp. 434-444.
- [9] Arghir, M., Zerarka, E., and Pieanu, G., 2011, "Rotordynamic Analysis of Textured Annular Seals with Multiphase (Bubbly) Flow," *INCAS Bulletin*, **3**(3), pp 3-13.
- [10] San Andrés, L., 2012, "Rotordynamic Force Coefficients of Bubbly Mixture Annular Pressure Seals," *ASME J. Eng. Gas Turb. Power*, **134**(2), p. 022503.

- [11] San Andrés, L., Lu, X., and Zhu, J., 2018, "Leakage and Force Coefficients for Pump Annular Seals Operating with Air/Oil Mixtures: Measurements vs Predictions and Air Injection to Increase Seal Dynamic Stiffnesses," *Proc. 34th Turbomachinery & Pump Symposium*, Houston, September.
- [12] Zhang, M., Childs, D., Mclean, J., Jr., Dung, L.T., and Shrestha, H., 2018, "Experimental Study of the Leakage and Rotordynamic Coefficients of a Long Smooth Seal with Two-Phase, Mainly-Oil Mixtures," *ASME J. Tribol.*, **141**(4), p. 042201.
- [13] Hendricks, R.C., 1987, "Straight Cylindrical Seal for High-Performance Turbomachines," NASA Technical Paper 1850.
- [14] Beatty, P. A., and Hughes, W. F., 1987, "Turbulent Two-Phase Flow in Annular Seals," *ASLE Trans.*, **30**(1) pp. 11-18.
- [15] White, F. M., 1974, *Viscous Fluid Flow*, McCraw-Hill, New York, p. 486, p. 543, p. 575.
- [16] Beatty, P. A., and Hughes, W. F., 1990, "Stratified Two-Phase Flow in Annular Seals," *ASME J. Tribol.*, **112**(2) pp. 372-381.
- [17] Arauz, G. L., and San Andrés, L., 1997, "Analysis of Two-Phase Flow in Cryogenic Damper Seals - Part I: Theoretical Model," *ASME J. Tribol.*, **120**, pp. 221-227.
- [18] Arauz, G. L., and San Andrés, L., 1997, "Analysis of Two-Phase Flow in Cryogenic Damper Seals - Part II: Model Validation and Predictions," *ASME J. Tribol.*, **120**, pp. 228-233
- [19] Oike, M., Nosaka, M., Kikuchi, M., 1999, "Two-Phase Flow in Floating-Ring Seals for Cryogenic Turbopumps," *Tribol. Trans.*, **42**(2) pp. 273-281.
- [20] Hassini, M. A., Arghir, M., 2013, "Phase Change and Choked Flow Effects on Rotordynamic Coefficients of Cryogenic Annular Seals," *ASME J. Tribol.*, **135**, p. 042201.
- [21] Ruud, F.O., 1976, "Vibration of Deriaz Pumps at Dos Amigos Pumping Plant," *ASME J. Fluids Eng.*, December, **98**(4), pp. 674-679.
- [22] Smith, D.R., Price, S.M., and Kunz, F.K., 1996, "Centrifugal Pump Vibration Caused by Supersynchronous Shaft Instability Use of Pumpout Vanes to Increase Pump Shaft Stability," *Proc. 13th International Pump Users Symposium*, Houston, TX, Mar. 5-7.

- [23] Iwatsubo, T., and Nishino, T., 1993, “An Experimental Study on the Static and Dynamic Characteristics of Pump Annular Seals,” *Proc. 7th Workshop on Rotordynamic Instability Problems in High Performance Turbomachinery*, College Station, TX, May 10–12, pp. 30-45.
- [24] Brunetiere, N., 2014, “Two-phase Flow in a Mechanical Seal,” STLE Annual Meeting & Exhibition, Lake Buena Vista, Florida, May 18-22.
- [25] Voigt, A.J., Mandrum-Polsen, C., Nielsen, K. K., and Santos, I. F., 2016, “Design and Calibration of a Full Scale Active Magnetic Bearing Based Test Facility For Investigating Rotordynamic Properties of Turbomachinery Seals in Multiphase Flow,” *ASME J. Eng. Gas Turb. Power*, **139**(5), p. 052505.
- [26] Voigt, A.J., Iudiciani, P., Nielsen, K. K., and Santos, I. F., 2016, “CFD Applied for the Identification of Stiffness and Damping Properties for Smooth Annular Turbomachinery Seals in Multiphase Flow,” *ASME Paper No. GT2016-57905*.
- [27] Li, Z., Fang, Z., and Li, J., 2019, “Numerical Investigation on the Leakage and Rotordynamic Characteristics for Three Types of Annular Gas Seals in Wet Gas Conditions,” *ASME J. Eng. Gas Turb. Power*, **141**, p. 032504.
- [28] Grimaldi, G., Pascazio, G., Vannini, G., and Afferrante, L., 2019, “Stratified Two-Phase Flow in Annular Seals,” *ASME J. Eng. Gas Turb. Power*, **141**, p. 071006.
- [29] San Andrés, L., Lu, X., and Liu, Q., 2016, “Measurements of Flow Rate and Force Coefficients in a Short-Length Annular Seal Supplied with a Liquid/Gas Mixture (Stationary Journal),” *Tribol. Trans.*, **59** (4), pp. 758-767.
- [30] San Andrés, L., Lu, X., and Wu, T., 2019, “On the Influence of Gas Content on the Rotordynamic Force Coefficients of Three-Wave (Air in Oil) Annular Seal for Multiple Phase Pumps,” *ASME J. Fluids Eng.*, **142**(3), p. 031102.
- [31] Lu, X., and San Andrés, L., 2020, “Leakage and Rotordynamic Force Coefficients of a Three-Wave (Air in Oil) Wet Annular Seal: Measurements and Predications,” *ASME J. Eng. Gas Turbine Power*, **141** (3), 032503.
- [32] San Andrés, L., Lu, X., and Zhu, J., 2018, “On the Leakage and Rotordynamic Force Coefficients of Pump Annular Seals Operating with Air/Oil Mixtures: Measurements and Predictions,” *Proc. 2nd ASIA Turbomachinery & Pump Symposium*, Singapore, Mar. 22-25.

- [33] San Andrés, L., and Lu, X., 2018, “Leakage, Drag Power and Rotordynamic Force Coefficients of an Air in Oil (Wet) Annular Seal,” ASME J. Eng. Gas Turb. Power, **140**, p. 012505.
- [34] Lu, X., San Andrés, L., and Wu, T., 2020, “Leakage and Force Coefficients of a Grooved Wet (Bubbly Liquid) Seal for Multiphase Pumps and Comparisons with Prior Test Results for a Three Wave Seal,” ASME J. Eng. Gas Turbine Power, **141** (1), p. 011011.
- [35] Yang, J., San Andrés, L., and Lu, X., 2019, “On the Leakage, Torque and Dynamic Force Coefficients of an Air in Oil (Wet) Annular Seal: a CFD Analysis Anchored to Test Data,” ASME J. Eng. Gas Turbine Power, **141** (2), 021008.
- [36] Yang, J., San Andrés, L., and Lu, X., 2019, “Leakage and Dynamic Force Coefficients of a Pocket Damper Seal Operating under a Wet Gas Condition: Test vs. Predictions,” J. Eng. Gas Turbine Power, 141(11), p.111001.
- [37] Vannini, G., Bertoneri, M., Nielsen, K. K, Ludiciani, P., and Stronach, R., 2016, “Experimental Results and Computational Fluid Dynamics Simulations of Labyrinth and Pocket Damper Seals for Wet Gas Compression,” ASME J. Eng. Gas Turbines Power, **138**(5), pp. 052501.
- [38] Zhang, M., James E. Mclean Jr., and Childs, D., 2017 “Experimental Study of the Static and Dynamic Characteristics of a Long Smooth Seal with Two-Phase, Mainly-Air Mixtures,” ASME J. Eng. Gas Turb. Power, **139**(12), p. 122504.
- [39] Tran, D.L., Childs, D., Shrestha, H., and Zhang, M., 2020, “Preswirl and Mixed-Flow (Mainly-Liquid) Effects on Rotordynamic Performance of a Long (L/D= 0.75) Smooth Seal,” ASME J. Eng. Gas Turb. Power, 142(3), p. 031012.
- [40] Damian, S.M., 2013, “An Extended Mixture Model for the Simultaneous Treatment of Short and Long Scale Interfaces”, Ph.D. thesis, Dissertationsschrift, Universidad Nacional del Litoral.
- [41] Ishii, M., and Hibiki, T., 2010, *Thermo-Fluid Dynamics of Two-Phase Flow*, Springer New York Dordrecht Heidelberg London, Chap. 9, Chap. 13.
- [42] Hirt C.W., and Nichols, B.D., 1981, “Volume of Fluid (VOF) Method for the Dynamics of Free Boundaries,” J. Comput. Phys., **39**, pp. 201-225.

- [43] Manninen, M., Taivassalo, V., and Kallio, S., 1996, "On the Mixture Model for Multiphase Flow," Espoo 1996, Technical Research Center of Finland, VTT Publications 288. 67p.
- [44] Salhi, A., C. Rey, and J. M. Rosant, 1992, "Pressure Drop in Single-Phase and Two-Phase Couette-Poiseuille Flow," *J. Fluids Eng.*, **114**(1), pp: 80-84.
- [45] Nelson, C.C., and Nguyen, D.T., 1987, "Comparison of Hir's Equation with Moody's Equation for Determining Rotordynamic Coefficients of Annular Pressure Seals," *ASME J. Tribol.*, **109**, pp.144-148.
- [46] Awad, M.M., and Muzychka, Y.S., 2008, "Effective Property Models for Homogeneous Two-Phase Flows," *Eep Therm. Fluid SCI*, **33**(1), pp.106-113.
- [47] Fourar, M., Bories, S., 1995, "Experimental Study of Air-Water Two-Phase Flow through a Fracture (Narrow Channel)", *Int. J. Multiphase Flow*, **21**, pp. 621-637.
- [48] Cicchitti, A., Lombaradi, C., Silversti, M., Soldaini, G., Zavattarlli, R., 1960, "Two-Phase Cooling Experiments – Pressure Drop Heat Transfer Burnout Measurements", *Energia Nucleare*, 7 (6), pp. 407–425.
- [49] Zhou, Y., 1992, "Thermohydrodynamic Analysis of Product-Lubricated Hydrostatic Bearings in Turbulent Regime," Ph.D. Thesis, Texas A&M University, College Station, TX.
- [50] Arauz, G.L., 1997, "Analysis of Two-Phase Flow in Damper Seals for Cryogenic Turbomachinery," Ph.D. Thesis, Texas A&M University, College Station, TX.
- [51] San Andrés, L., and Lu, X., 2016, "Leakage and Rotordynamic Force Coefficients in an (Air in Oil) Wet Seal: Influence of Shaft Speed," Annual Report to the TAMU Turbomachinery Research Consortium, TRC-Seal-01-16, Texas A&M University.
- [52] Yang, J., and San Andrés, L., 2019, "On the Influence of the Entrance Section on the Rotordynamic Performance of a Pump Seal with Uniform Clearance: A Sharp Edge versus A Round Inlet," *ASME J. Eng. Gas Turbine Power*, **141**, p. 031029-2.
- [53] Arghir, M, and Frene, J., 2001, "Numerical Solution of Lubrication's Compressible Bulk Flow Equations. Applications to Annular Gas Seals Analysis," *Proc. ASME Turbo Expo conference*. New Orleans, LA, July 4-7.
- [54] Andrews, M. J., and O'Rourke, P. J., 1996, "The Multiphase Particle-in-Cell (MP-PIC) Method for Dense Particulate Flows," *Int. J. Multiphase Flow*, **22**(2), pp. 379–402.

- [55] Zhang, M., 2017, “Experimental Study of the Static and Dynamic Characteristics of a Long (L/D=0.65) Smooth Annular Seal Operating under Two-Phase (Liquid/Gas) Conditions, Ph.D. thesis, Texas A&M University, College Station, TX.
- [56] San Andrés, L., 1991, “Effect of Eccentricity on the Force Response of a Hybrid Bearing”, *Tribol. Trans.*, **34**(4), pp. 537-544.
- [57] Schiller, L., and Naumann, Z., 1935, “A Drag Coefficient Correlation,” *VDI Zeitung*, **77**, pp. 318-320.
- [58] Clift, R., Grace, J.R., and Weber, M.E., 1978, *Bubbles, Drops, and Particles*. London: Academic Press, 351 p.
- [59] Massey, B.S., Ward Smith, J., 2012, *Mechanics of Fluids, 9th Edition*, Spon Press, New York, Chap. 7, pp. 247-254.
- [60] Patanka, S.V., *Numerical Heat Transfer and Fluid Flow*, Hemisphere, Washington, D.C., 1980.
- [61] Van Doormaal, J.P., and Raithby, G.D., 1984, “Enhancements of the Simple Method for Predicting Incompressible Fluid Flows,” *Numer. Heat Transf.*, **7**, pp.147-163.
- [62] Soulas, T., and San Andrés, L., 2007, “A Bulk Flow Model for Off-Centered Honeycomb Gas Seals,” *ASME J. Eng. Gas Turbine Power*, **129**, pp. 185-194.
- [63] Zhou, Y., San Andrés, L., and Childs, D. W., 1993, “Thermal Effects in Cryogenic Liquid Annular Seals-Part I: Theory and Approximate Solution,” *ASME J. Tribol.*, **115**, pp. 267-276.
- [64] San Andrés, L., Zhou, Y., and Childs, D. W., 1993, “Thermal Effects in Cryogenic Liquid Annular Seals-Part II: Numerical Solution and Results,” *ASME J. Tribol.*, **115**, pp. 277-283.
- [65] San Andrés, L., 2009, “Notes 12. (a) Annular Pressure (Damper) Seals, and (b) Hydrostatic Journal Bearings,” *Modern Hydrodynamic Lubrication Theory*, Libraries Texas A&M University Repository, <http://hdl.handle.net/1969.1/93252>.
- [66] Zirkelback, N., and San Andrés, L., **1997**, “Bulk-Flow Model for the Transition to Turbulence Regime in Annular Pressure Seals”, *Tribol. Trans.*, **39** (4), pp. 835-842.

APPENDIX A

DERIVATION OF MOMENTUM EQUATIONS

Recall from Eq. (13) that the mixture momentum equation is [43]

$$\frac{\partial}{\partial t} \rho_m \mathbf{U}_m + \nabla \cdot \rho_m \mathbf{U}_m \mathbf{U}_m + \nabla \cdot \sum_{k=1}^2 (\alpha_k \rho_k \mathbf{U}_{dr,k} \mathbf{U}_{dr,k}) = -\nabla p_m + \nabla \cdot (\boldsymbol{\tau}_m + \boldsymbol{\tau}_{Tm}) + \rho_m \mathbf{g} \quad (\text{A-1})$$

$k = g, l$

Using Eq. (11), Eq. (A-1) can be rewritten as

$$\frac{\partial}{\partial t} \rho_m \mathbf{U}_m + \nabla \cdot \sum_{k=1}^2 (\alpha_k \rho_k \mathbf{U}_k \mathbf{U}_k) = -\nabla p_m + \nabla \cdot (\boldsymbol{\tau}_m + \boldsymbol{\tau}_{Tm}) + \rho_m \mathbf{g}, \quad k = g, l \quad (\text{A-2})$$

The velocity of component k can be written as the sum of the diffusion velocity and the mixture velocity

$$\mathbf{U}_k = \mathbf{U}_{dr,k} + \mathbf{U}_m, \quad k = g, l \quad (\text{A-3})$$

In Hirs' bulk flow theory, the turbulent effect is accounted by the wall shear stresses. Thus, the second term on the right hand side of Eq. (A-2) can be written as

$$\nabla \cdot (\boldsymbol{\tau}_m + \boldsymbol{\tau}_{Tm}) \rightarrow \boldsymbol{\tau} \quad (\text{A-4})$$

Using the film averaged variables, Eq. (A-2) becomes Eq. (A-3)

$$\frac{\partial}{\partial t} \bar{\rho}_m \bar{\mathbf{U}}_m + \nabla \cdot \sum_{k=1}^2 (\bar{\alpha}_k \bar{\rho}_k \bar{\mathbf{U}}_k \bar{\mathbf{U}}_k) = -\nabla \bar{p}_m + \boldsymbol{\tau} + \bar{\rho}_m \mathbf{g}, \quad k = g, l \quad (\text{A-5})$$

The X-momentum Equation

Considering the control volume as shown in Figure 31, the conservation of momentum along the X direction leads to:

$$\begin{aligned} & \oint_{CS} (\bar{\alpha}_l \bar{\rho}_l \bar{U}_l \bar{\mathbf{U}}_l \cdot d\mathbf{A}) \\ &= \left(\frac{\partial}{\partial x} (\bar{\alpha}_l \bar{\rho}_l H (\bar{U}_{dr,l} + \bar{U}_m)^2) + \frac{\partial}{\partial z} (\bar{\alpha}_g \bar{\rho}_g (\bar{U}_{dr,l} + \bar{U}_m) (\bar{W}_{dr,l} + \bar{W}_m) H) \right) \cdot \Delta x \Delta z \end{aligned} \quad (\text{A-10})$$

Similarly, the second term on the RHS of Eq. (A-8) for the gas component becomes

$$\begin{aligned} & \oint_{CS} (\bar{\alpha}_g \bar{\rho}_g \bar{U}_g \bar{\mathbf{U}}_g \cdot d\mathbf{A}) \\ &= \left(\frac{\partial}{\partial x} (\bar{\alpha}_g \bar{\rho}_g H (\bar{U}_{dr,g} + \bar{U}_m)^2) + \frac{\partial}{\partial z} (\bar{\alpha}_l \bar{\rho}_l (\bar{U}_{dr,g} + \bar{U}_m) (\bar{W}_{dr,g} + \bar{W}_m) H) \right) \cdot \Delta x \Delta z \end{aligned} \quad (\text{A-11})$$

Substitute Eq. (A-10) and Eq. (A-11) into Eq. (A-8)

$$\sum_{k=1}^2 \oint_{CS} (\bar{\alpha}_k \bar{\rho}_k \bar{U}_k \bar{\mathbf{U}}_k \cdot d\mathbf{A}) = \left(\begin{aligned} & \frac{\partial}{\partial x} (\bar{\alpha}_l \bar{\rho}_l (\bar{U}_{dr,l} + \bar{U}_m)^2 H) + \\ & \frac{\partial}{\partial z} (\bar{\alpha}_l \bar{\rho}_l (\bar{U}_{dr,l} + \bar{U}_m) (\bar{W}_{dr,l} + \bar{W}_m) H) + \\ & \frac{\partial}{\partial x} (\bar{\alpha}_g \bar{\rho}_g (\bar{U}_{dr,g} + \bar{U}_m)^2 H) + \\ & \frac{\partial}{\partial z} (\bar{\alpha}_g \bar{\rho}_g (\bar{U}_{dr,g} + \bar{U}_m) (\bar{W}_{dr,g} + \bar{W}_m) H) \end{aligned} \right) \cdot \Delta x \Delta z \quad (\text{A-12})$$

After some algebra, Eq. (A-12) becomes

$$\sum_{k=1}^2 \oint_{CS} (\bar{\alpha}_k \bar{\rho}_k \bar{U}_k \bar{\mathbf{U}}_k \cdot d\mathbf{A}) = \left(\begin{aligned} & \frac{\partial}{\partial x} (\bar{\rho}_m \bar{U}_m^2 + \bar{\alpha}_l \bar{\rho}_l \bar{U}_{dr,l}^2 + \bar{\alpha}_g \bar{\rho}_g \bar{U}_{dr,g}^2) H + \\ & \frac{\partial}{\partial z} (\bar{\alpha}_m \bar{\rho}_m \bar{U}_m + \bar{\alpha}_l \bar{\rho}_l \bar{U}_{dr,l} \bar{W}_{dr,l} + \bar{\alpha}_g \bar{\rho}_g \bar{U}_{dr,g} \bar{W}_{dr,g}) H \end{aligned} \right) \cdot \Delta x \Delta z \quad (\text{A-13})$$

Rewrite Eq. (A-13):

$$\sum_{k=1}^2 \oint_{CS} (\bar{\alpha}_k \bar{\rho}_k \bar{U}_k \bar{\mathbf{U}}_k \cdot d\mathbf{A}) = \left(\begin{aligned} & \frac{\partial}{\partial x} \left(\bar{\rho}_m \bar{U}_m^2 H \left(1 + \frac{\bar{\alpha}_l \bar{\rho}_l \bar{U}_{dr,l}^2 + \bar{\alpha}_g \bar{\rho}_g \bar{U}_{dr,g}^2}{\bar{\rho}_m \bar{U}_m^2} \right) \right) + \\ & \frac{\partial}{\partial z} \left(\bar{\rho}_m \bar{U}_m \bar{W}_m H \left(1 + \frac{\bar{\alpha}_l \bar{\rho}_l \bar{U}_{dr,l} \bar{W}_{dr,l} + \bar{\alpha}_g \bar{\rho}_g \bar{U}_{dr,g} \bar{W}_{dr,g}}{\bar{\rho}_m \bar{U}_m \bar{W}_m} \right) \right) \end{aligned} \right) \cdot \Delta x \Delta z \quad (\text{A-14})$$

Substitute Eq. (A-7) and (A-14) into Eq. (A-6):

$$\sum F_x = \left(\begin{aligned} & \frac{\partial}{\partial t} (\bar{\rho}_m \bar{U}_m H) + \\ & \frac{\partial}{\partial x} \left(\bar{\rho}_m \bar{U}_m^2 H \left(1 + \frac{\bar{\alpha}_l \bar{\rho}_l \bar{U}_{dr,l}^2 + \bar{\alpha}_g \bar{\rho}_g \bar{U}_{dr,g}^2}{\rho_m U_m^2} \right) \right) + \\ & \frac{\partial}{\partial z} \left(\bar{\rho}_m \bar{U}_m \bar{W}_m H \left(1 + \frac{\bar{\alpha}_l \bar{\rho}_l \bar{U}_{dr,l} \bar{W}_{dr,l} + \bar{\alpha}_g \bar{\rho}_g \bar{U}_{dr,g} \bar{W}_{dr,g}}{\bar{\rho}_m \bar{U}_m \bar{W}_m} \right) \right) \end{aligned} \right) \Delta x \Delta z \quad (\text{A-15})$$

The X-forces acting on the control volume as shown in Figure 31 is

$$\sum F_x = F_{x^-} + F_{\perp x} - F_{x^+} - \tau_{xy} \Big|_0^H \Delta x \Delta z \quad (\text{A-16})$$

where the individual force components acting on the surface on the control volume are

$$F_{x^-} = \left(P - \frac{\partial P}{\partial x} \frac{\Delta x}{2} \right) \left(H - \frac{\partial H}{\partial x} \frac{\Delta x}{2} \right) \Delta z \quad (\text{A-17})$$

$$F_{x^+} = \left(P + \frac{\partial P}{\partial x} \frac{\Delta x}{2} \right) \left(H + \frac{\partial H}{\partial x} \frac{\Delta x}{2} \right) \Delta z \quad (\text{A-18})$$

For a small angle β , the X-component of the force acting on the top surface is

$$F_{\perp x} = P \Delta x \Delta z \sin \beta \simeq P \Delta x \Delta z \tan \beta = P \Delta x \Delta z \frac{\partial H}{\partial x} \quad (\text{A-19})$$

$\tau_{x|_H}$ and $\tau_{x|_0}$ are the wall shear stress imposed by the rotor and stator on the control volume.

Substituting Eq. (A-17) - (A-19) into Eq. (A-16) and neglecting terms that contain $\left(\frac{\Delta x}{2}\right)^2$

produces

$$\sum F_x = -H \frac{\partial P}{\partial x} \Delta x \Delta z - \tau_{xy} \Big|_0^H \Delta x \Delta z \quad (\text{A-20})$$

Combining Eq. (A-15) and Eq. (A-20) renders

$$\begin{aligned}
& \frac{\partial}{\partial t}(\bar{\rho}_m \bar{U}_m H) + \frac{\partial}{\partial x}(\bar{\rho}_m \bar{U}_m^2 H (1+r_1)) + \frac{\partial}{\partial z}(\bar{\rho}_m \bar{U}_m \bar{W}_m H (1+r_2)) \\
& = -H \frac{\partial P}{\partial x} - \tau_{xy} \Big|_0^H
\end{aligned} \tag{A-21}$$

where $r_1 = \frac{\bar{\alpha}_l \bar{\rho}_l \bar{U}_{dr,l}^2 + \bar{\alpha}_g \bar{\rho}_g \bar{U}_{dr,g}^2}{\bar{\rho}_m \bar{U}_m^2}$, $r_2 = \frac{\bar{\alpha}_l \bar{\rho}_l \bar{U}_{dr,l} \bar{W}_{dr,l} + \bar{\alpha}_g \bar{\rho}_g \bar{U}_{dr,g} \bar{W}_{dr,g}}{\bar{\rho}_m \bar{U}_m \bar{W}_m}$. Eq. (A-21) is the X-

momentum equation for the mixture.

Z-momentum Equation

Similarly, the conservation of momentum in the Z direction leads to:

$$\sum F_Z = \frac{\partial}{\partial t} \int_{CV} \bar{\rho}_m \bar{W}_m d\forall + \sum_{k=1}^2 \oint_{CS} (\bar{\alpha}_k \bar{\rho}_k \bar{W}_k \bar{U}_k \cdot d\mathbf{A}) \tag{A-22}$$

The first term on the RHS of Eq. (A-22) is

$$\frac{\partial}{\partial t} \int_{CV} \bar{\rho}_m \bar{W}_m d\forall = \frac{\partial}{\partial t} (\bar{\rho}_m \bar{W}_m H \Delta x \Delta z) \tag{A-23}$$

The second term on the RHS of Eq. (A-22) can be written as

$$\sum_{k=1}^2 \oint_{CS} (\bar{\alpha}_k \bar{\rho}_k \bar{W}_k \bar{U}_k \cdot d\mathbf{A}) = \oint_{CS} (\bar{\alpha}_l \bar{\rho}_l \bar{W}_l \bar{U}_l \cdot d\mathbf{A}) + \oint_{CS} (\bar{\alpha}_g \bar{\rho}_g \bar{W}_g \bar{U}_g \cdot d\mathbf{A}) \tag{A-24}$$

The first term on the RHS of Eq. (A-24) for the liquid component becomes:

$$\oint_{CS} (\bar{\alpha}_l \bar{\rho}_l \bar{W}_l \bar{U}_l \cdot d\mathbf{A}) = \left(\frac{\partial}{\partial x} (\bar{\alpha}_l \bar{\rho}_l \bar{W}_l \bar{U}_l H) + \frac{\partial}{\partial z} (\bar{\alpha}_l \bar{\rho}_l \bar{W}_l^2 H) \right) \cdot \Delta x \Delta z \tag{A-25}$$

Substitute Eq. (A-3) into Eq. (A-25)

$$\begin{aligned}
& \oint_{CS} (\bar{\alpha}_l \bar{\rho}_l \bar{W}_l \bar{U}_l \cdot d\mathbf{A}) \\
& = \left(\frac{\partial}{\partial x} (\bar{\alpha}_l \bar{\rho}_l (\bar{W}_{dr,l} + \bar{W}_m) (\bar{U}_{dr,l} + \bar{U}_m) H) + \frac{\partial}{\partial z} (\bar{\alpha}_l \bar{\rho}_l (\bar{W}_{dr,l} + \bar{W}_m)^2 H) \right) \cdot \Delta x \Delta z
\end{aligned} \tag{A-26}$$

Similarly, for the gas component

$$\begin{aligned}
& \oint_{CS} (\bar{\alpha}_g \bar{\rho}_g \bar{W}_g \bar{\mathbf{U}}_g \cdot d\mathbf{A}) \\
&= \left(\frac{\partial}{\partial x} (\bar{\alpha}_g \bar{\rho}_g (\bar{W}_{dr,g} + \bar{W}_m) (\bar{U}_{dr,g} + \bar{U}_m) H) + \frac{\partial}{\partial z} (\bar{\alpha}_g \bar{\rho}_g (\bar{W}_{dr,g} + \bar{W}_m)^2 H) \right) \cdot \Delta x \Delta z
\end{aligned} \tag{A-27}$$

Substitute Eq. (A-26) and (A-27) into Eq. (A-24)

$$\begin{aligned}
& \sum_{k=1}^2 \oint_{CS} (\bar{\alpha}_k \bar{\rho}_k \bar{W}_k \bar{\mathbf{U}}_k \cdot d\mathbf{A}) \\
&= \left(\frac{\partial}{\partial x} (\bar{\alpha}_l \bar{\rho}_l (\bar{W}_{dr,l} + \bar{W}_m) (\bar{U}_{dr,l} + \bar{U}_m) H) + \frac{\partial}{\partial z} (\bar{\alpha}_l \bar{\rho}_l (\bar{W}_{dr,l} + \bar{W}_m)^2 H) \right) \cdot \Delta x \Delta z \\
&+ \left(\frac{\partial}{\partial x} (\bar{\alpha}_g \bar{\rho}_g (\bar{W}_{dr,g} + \bar{W}_m) (\bar{U}_{dr,g} + \bar{U}_m) H) + \frac{\partial}{\partial z} (\bar{\alpha}_g \bar{\rho}_g (\bar{W}_{dr,g} + \bar{W}_m)^2 H) \right) \cdot \Delta x \Delta z
\end{aligned} \tag{A-28}$$

Reorganize Eq. (A-28)

$$\begin{aligned}
& \sum_{k=1}^2 \oint_{CS} (\bar{\alpha}_k \bar{\rho}_k \bar{W}_k \bar{\mathbf{U}}_k \cdot d\mathbf{A}) \\
&= \left(\frac{\partial}{\partial x} (\bar{\rho}_m \bar{U}_m \bar{W}_m + \bar{\alpha}_l \bar{\rho}_l \bar{U}_{dr,l} \bar{W}_{dr,l} + \bar{\alpha}_g \bar{\rho}_g \bar{U}_{dr,g} \bar{W}_{dr,g}) H + \frac{\partial}{\partial z} (\bar{\alpha}_l \bar{\rho}_l \bar{W}_{dr,l}^2 + \bar{\alpha}_g \bar{\rho}_g \bar{W}_{dr,g}^2 + \bar{\rho}_m \bar{W}_m^2) H \right) \Delta x \Delta z
\end{aligned} \tag{A-29}$$

Rewrite Eq. (A-29) as

$$\begin{aligned}
& \sum_{k=1}^2 \oint_{CS} (\bar{\alpha}_k \bar{\rho}_k \bar{W}_k \bar{\mathbf{U}}_k \cdot d\mathbf{A}) \\
&= \left(\frac{\partial}{\partial x} \left(\bar{\rho}_m \bar{U}_m \bar{W}_m H \left[1 + \frac{\bar{\alpha}_l \bar{\rho}_l \bar{U}_{dr,l} \bar{W}_{dr,l} + \bar{\alpha}_g \bar{\rho}_g \bar{U}_{dr,g} \bar{W}_{dr,g}}{\bar{\rho}_m \bar{U}_m \bar{W}_m} \right] \right) + \frac{\partial}{\partial z} \left(\bar{\rho}_m \bar{W}_m^2 H \left(1 + \frac{\bar{\alpha}_l \bar{\rho}_l \bar{W}_{dr,l}^2 + \bar{\alpha}_g \bar{\rho}_g \bar{W}_{dr,g}^2}{\bar{\rho}_m \bar{W}_m^2} \right) \right) \right) \Delta x \Delta z
\end{aligned} \tag{A-30}$$

Substitute Eq. (A-23) and (A-30) into Eq. (A-42)

$$\sum F_z = \left(\begin{aligned} & \frac{\partial}{\partial t} (\bar{\rho}_m \bar{W}_m H) + \\ & \frac{\partial}{\partial x} \left(\bar{\rho}_m \bar{U}_m \bar{W}_m H \left(1 + \frac{\bar{\alpha}_l \bar{\rho}_l \bar{U}_{dr,l} \bar{W}_{dr,l} + \bar{\alpha}_g \bar{\rho}_g \bar{U}_{dr,g} \bar{W}_{dr,g}}{\bar{\rho}_m \bar{U}_m \bar{W}_m} \right) \right) + \\ & \frac{\partial}{\partial z} \left(\bar{\rho}_m \bar{W}_m^2 H \left(1 + \frac{\bar{\alpha}_l \bar{\rho}_l \bar{W}_{dr,l}^2 + \bar{\alpha}_g \bar{\rho}_g \bar{W}_{dr,g}^2}{\bar{\rho}_m \bar{W}_m^2} \right) \right) \end{aligned} \right) \Delta x \Delta z \quad (\text{A-31})$$

The Z-forces acting on the control volume as shown in Figure A-1 is

$$\sum F_z = F_{z-} - F_{z+} - \tau_{zy} \Big|_0^H \Delta x \Delta z \quad (\text{A-32})$$

where the individual force components acting on the surface on the control volume are

$$F_{z-} = \left(P - \frac{\partial P}{\partial z} \frac{\Delta z}{2} \right) H \Delta x \quad (\text{A-33})$$

$$F_{z+} = \left(P + \frac{\partial P}{\partial z} \frac{\Delta z}{2} \right) H \Delta x \quad (\text{A-34})$$

τ_{rz} and τ_{sz} are the wall shear stress imposed by the rotor and stator on the control volume.

Substituting Eq. (A-33), and (A-34) into Eq. (A-32) produces

$$\sum F_z = -H \frac{\partial P}{\partial z} \Delta x \Delta z - \tau_{zy} \Big|_0^H \Delta x \Delta z \quad (\text{A-35})$$

Combining Eq. (A-31) and (A-35) renders

$$\begin{aligned} & \frac{\partial}{\partial t} (\bar{\rho}_m \bar{W}_m H) + \frac{\partial}{\partial x} (\bar{\rho}_m \bar{U}_m \bar{W}_m H (1+r_3)) + \frac{\partial}{\partial z} (\bar{\rho}_m \bar{W}_m^2 H (1+r_4)) \\ & = -H \frac{\partial P}{\partial z} - \tau_{zy} \Big|_0^H \end{aligned} \quad (\text{A-36})$$

where $r_3 = \frac{\bar{\alpha}_l \bar{\rho}_l \bar{U}_{dr,l} \bar{W}_{dr,l} + \bar{\alpha}_g \bar{\rho}_g \bar{U}_{dr,g} \bar{W}_{dr,g}}{\bar{\rho}_m \bar{U}_m \bar{W}_m}$, $r_4 = \frac{\bar{\alpha}_l \bar{\rho}_l \bar{W}_{dr,l}^2 + \bar{\alpha}_g \bar{\rho}_g \bar{W}_{dr,g}^2}{\bar{\rho}_m \bar{W}_m^2}$. Eq. (A-36) is the

Z-momentum equation for the mixture.

APPENDIX B

DERIVATION OF DIFFUSION VELOCITY

Appendix B addresses to the modeling of the diffusion velocity of a liquid-gas two-component flow with liquid as the primary flow and gas the secondary flow. The diffusion velocity of the secondary phase (gas) represents the velocity of the gas mass center relative to the mass center of the mixture [43], as defined below

$$\begin{aligned}
 \bar{\mathbf{U}}_{\text{dr,g}} &= \bar{\mathbf{U}}_g - \bar{\mathbf{U}}_m \\
 \rightarrow \bar{\mathbf{U}}_{\text{dr,g}} &= \bar{\mathbf{U}}_g - (\lambda_g \bar{\mathbf{U}}_g + \lambda_l \bar{\mathbf{U}}_l) \\
 \rightarrow \bar{\mathbf{U}}_{\text{dr,g}} &= \bar{\mathbf{U}}_g - \lambda_g \bar{\mathbf{U}}_g - (1 - \lambda_g) \bar{\mathbf{U}}_l \\
 \rightarrow \bar{\mathbf{U}}_{\text{dr,g}} &= (\bar{\mathbf{U}}_g - \bar{\mathbf{U}}_l) - \lambda_g (\bar{\mathbf{U}}_g - \bar{\mathbf{U}}_l) \\
 \rightarrow \bar{\mathbf{U}}_{\text{dr,g}} &= \bar{\mathbf{U}}_{\text{gl}} (1 - \lambda_g)
 \end{aligned} \tag{B-1}$$

where $\bar{\mathbf{U}}_{\text{gl}} = \bar{\mathbf{U}}_g - \bar{\mathbf{U}}_l$ is the velocity difference between the air and liquid, $\bar{\mathbf{U}}_m$ is the

velocity of the the mixture, and $\lambda_g = \frac{\bar{\alpha}_g \bar{\rho}_g}{\bar{\rho}_m}$ is the mass fraction of the gas phase.

The relative velocity of the gas to the liquid is given can be obtained from Eq. (B-2)

$$\frac{1}{2} \bar{\rho}_l \frac{\pi d_g^2}{4} C_D |\bar{\mathbf{U}}_{\text{gl}}| \bar{\mathbf{U}}_{\text{gl}} = \frac{4\pi}{3} \left(\frac{d_g}{2} \right)^3 (\bar{\rho}_g - \bar{\rho}_m) \mathbf{a} \tag{B-2}$$

where d_g is the diameter of air bubbles, C_D is a drag coefficient, and \mathbf{a} is the acceleration of the gas phase [43]

$$\mathbf{a} = \mathbf{g} - (\bar{\mathbf{U}}_m \cdot \nabla) \bar{\mathbf{U}}_m - \frac{\partial \bar{\mathbf{U}}_m}{\partial t} \tag{B-3}$$

The left hand side of Eq. (B-2) depicts the drag force applied on the gas bubble by the liquid domain; the right hand side of Eq. (B-2) represent the balance force caused by the density difference between the mixture and gas.

Eq. (B-2) can be simplified as

$$|\bar{\mathbf{U}}_{gl}| \bar{\mathbf{U}}_{gl} = \frac{4}{3} \frac{d_g}{C_D} \frac{(\bar{\rho}_g - \bar{\rho}_m)}{\bar{\rho}_l} \mathbf{a} \quad (\text{B-4})$$

There are several models to for the drag coefficient, one of the often used formula is the Schiller and Naumann model [57-59]

$$C_D = \begin{cases} \frac{24}{\text{Re}_B} (1 + 0.15 \text{Re}_B^{0.687}) & \text{Re}_B \leq 1,000 \\ 0.44 & \text{Re}_B > 1,000 \end{cases} \quad (\text{B-5})$$

where Re_B is the relative Reynolds number for the liquid and gas.

$$\text{Re}_B = \frac{\bar{\rho}_l |\bar{\mathbf{U}}_{gl}| d_g}{\bar{\mu}_l} \quad (\text{B-6})$$

Substituting Eq. (B-5) and Eq. (B-6) into Eq. (B-4) obtains Eq. (B-7)

$$\begin{aligned} \bar{\mathbf{U}}_{gl} &= \frac{\bar{\rho}_g d_g^2}{18 \bar{\mu}_l} \frac{1}{(1 + 0.15 \text{Re}_B^{0.687})} \frac{(\bar{\rho}_g - \bar{\rho}_m)}{\bar{\rho}_g} \mathbf{a} \\ \rightarrow \bar{\mathbf{U}}_{gl} &= \frac{\tau_g}{f_{drag}} \frac{\bar{\rho}_g - \bar{\rho}_m}{\bar{\rho}_g} \mathbf{a} \end{aligned} \quad (\text{B-7})$$

where $\tau_g = \frac{\bar{\rho}_g d_g^2}{18 \bar{\mu}_l}$ in Eq. (14) is the relaxation time for a gas bubble. The drag function

f_{drag} is defined as [57-59]

$$f_{drag} = \begin{cases} 1 + 0.15 \text{Re}_B^{0.687} & \text{Re}_B \leq 1,000 \\ 0.0183 \text{Re}_B & \text{Re}_B > 1,000 \end{cases} \quad (\text{B-8})$$

Based on Eqs. (B-1), the diffusion velocity along the X direction is

$$\bar{U}_{dr,g} = \bar{U}_{gl} (1 - \lambda_g) \quad (\text{B-9})$$

From Eq. (B-7), the relative velocity between the liquid and gas along the X direction is

$$\bar{U}_{gl} = \frac{\tau_g}{f_{fdrag(x)}} \frac{\bar{\rho}_g - \bar{\rho}_m}{\bar{\rho}_g} a_x \quad (\text{B-10})$$

From Eq. (B-3), for a vertical seal, $g_x = 0$.

$$a_x = -\left(\frac{\partial \bar{U}_m}{\partial x} + \frac{\partial \bar{W}_m}{\partial z}\right) \bar{U}_m - \frac{\partial \bar{U}_m}{\partial t} \quad (\text{B-11})$$

From Eq. (B-8), the drag function along the X direction is

$$f_{fdrag(x)} = \begin{cases} 1 + 0.15 \text{Re}_{B(X)}^{0.687} & \text{Re}_{B(X)} \leq 1,000 \\ 0.0183 \text{Re}_{B(X)} & \text{Re}_{B(X)} > 1,000 \end{cases} \quad (\text{B-12})$$

From Eq. (B-6), the relative Reynolds number

$$\text{Re}_{B(X)} = \frac{\bar{\rho}_l |\bar{U}_g - \bar{U}_l| d_g}{\bar{\mu}_l} \quad (\text{B-13})$$

Similarly, the Z component of the diffusion velocity is

$$\bar{W}_{dr,g} = \bar{W}_{gl} (1 - \lambda_g) \quad (\text{B-14})$$

From Eq. (B-7), the relative velocity between the liquid and gas along the Z direction is

$$W_{gl} = \frac{\tau_g}{f_{fdrag(z)}} \frac{\bar{\rho}_g - \bar{\rho}_m}{\bar{\rho}_g} a_z \quad (\text{B-15})$$

From Eq. (B-3), for a vertical seal, $g_z = 9.8 \text{ m/s}^2$.

$$a_z = g_z - \left(\frac{\partial \bar{U}_m}{\partial x} + \frac{\partial \bar{W}_m}{\partial z}\right) \bar{W}_m - \frac{\partial \bar{W}_m}{\partial t} \quad (\text{B-16})$$

From Eq. (B-8), the drag function along the z direction is

$$f_{fdrag(Z)} = \begin{cases} 1 + 0.15 \text{Re}_{B(Z)}^{0.687} & \text{Re}_{B(Z)} \leq 1,000 \\ 0.0183 \text{Re}_{B(Z)} & \text{Re}_{B(Z)} > 1,000 \end{cases} \quad (\text{B-17})$$

From Eq. (B-6), the relative Reynolds number

$$\text{Re}_{B(X)} = \frac{\bar{\rho}_l |\bar{U}_g - \bar{U}_l| d_g}{\bar{\mu}_l} \quad (\text{B-18})$$

APPENDIX C

SOLUTION OF THE ZEROth AND FIRST ORDER EQUATIONS

The zeroth and first order mass conservation equations, momentum equations, and gas volume fraction partial differential equations are discretized using the finite volume method as described in Refs. [60,61]. The discretized fluid domain consists of a series of rectangular control volumes where the velocities are located at the interfaces midway between the nodes of pressure, as shown in Figure 32. The x coordinate extends from 0 to $2\pi R$, and the z coordinate is along the seal axial direction. The i and j are the indices for the x and z node numbers. Figure 33 shows the control volumes for the circumferential and axial speeds, the pressure, and gas volume fraction (P , U_m , W_m and α_g), respectively. Note the control volumes for pressure (P) coincides with the control volume for gas volume fraction (α_g).

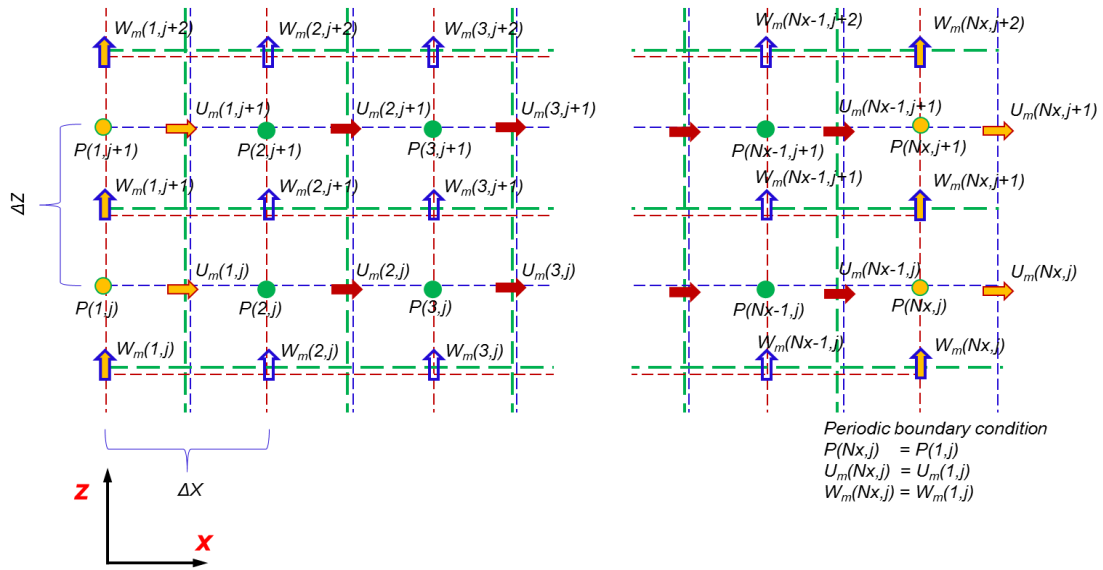


Figure 32 Mesh for fluid domain with flow variables P , U_m , W_m and α_g [48].

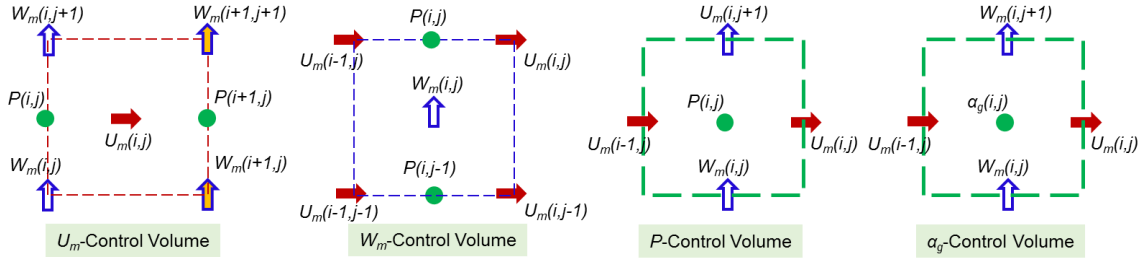


Figure 33 Control volumes for circumferential and axial velocity (U_m , W_m), pressure (P) and gas volume fraction (α_g).

Numerical solution of the zeroth order equation

The solution of the discretized equations follows the SIMPLEX algorithm of Van Doormaal and Raithby (1984). San Andrés et al. utilize the procedure to solve hydrostatic bearings [49] and fluid flow annular seals [62-65]. The continuity, momentum, and gas volume fraction equations are integrated over their control volumes to obtain the discretized equations.

Figure 34 shows the U_m control volume with the corresponding pressure nodes where the capital letters (E , W , N , S) represent the center of the East, West, North, South control volume, and the lower case letters (e,w,n,s) stand for the boundary face of a specific control volume, and the letter P represent the prime variable. Following Ref. [48] the discretized form of the circumferential momentum equation on the U_m control volume is:

$$\left[\left[\frac{k_x \tilde{\mu}_m}{h} \right]_P^{U_m} \delta_x^{U_m} \delta_z^{U_m} + \sum_{nb} a_{nb}^{U_m} \right] u_{m,P} = \sum_{nb} (a_{nb}^{U_m} u_{m,nb}) + h_P^{U_m} (p_P - p_E) \delta z^{U_m} + \left[\frac{k_J \tilde{\mu}_m \Lambda}{h} \frac{\Lambda}{2} \right]_P^{U_m} \delta_x^{U_m} \delta_z^{U_m} \quad (\text{C-1})$$

where $h_p^{U_m}$ is the film thickness at the U_m control volume, δz^{U_m} is the axial length of the cell, the subscript ‘nb’ means neighboring flow variables (namely East, West, North and South), and

$$a_{nb}^{U_m} : \begin{aligned} a_E^{U_m} &= Re_p^* \left[\left[-F_e^{U_m}, 0 \right] \right] (1 + r_1^e); & a_W^{U_m} &= Re_p^* \left[\left[F_w^{U_m}, 0 \right] \right] (1 + r_1^w) \\ a_N^{U_m} &= Re_p^* \left[\left[-F_n^{U_m}, 0 \right] \right] (1 + r_2^n); & a_S^{U_m} &= Re_p^* \left[\left[F_s^{U_m}, 0 \right] \right] (1 + r_2^s) \end{aligned}$$

$$\sum_{nb} a_{nb}^{U_m} : Re_p^* \left\{ \left[\left[F_e^{U_m}, 0 \right] \right] (1 + r_1^e) + \left[\left[-F_w^{U_m}, 0 \right] \right] (1 + r_1^w) + \left[\left[F_n^{U_m}, 0 \right] \right] (1 + r_2^n) + \left[\left[-F_s^{U_m}, 0 \right] \right] (1 + r_2^s) \right\}$$

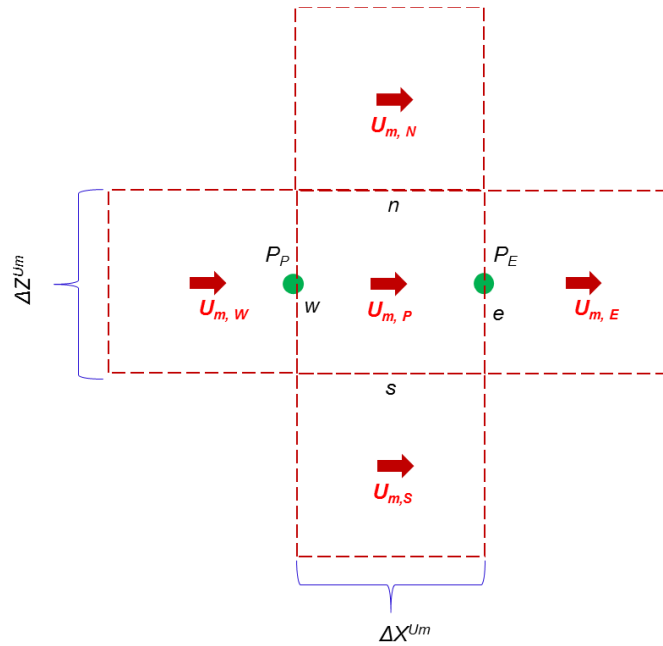


Figure 34 Control volume for mixture circumferential velocity U_m [48].

Figure 35 shows the W_m control volume with the corresponding pressure nodes. The lubricant flows from the south control volumes to the north ones.

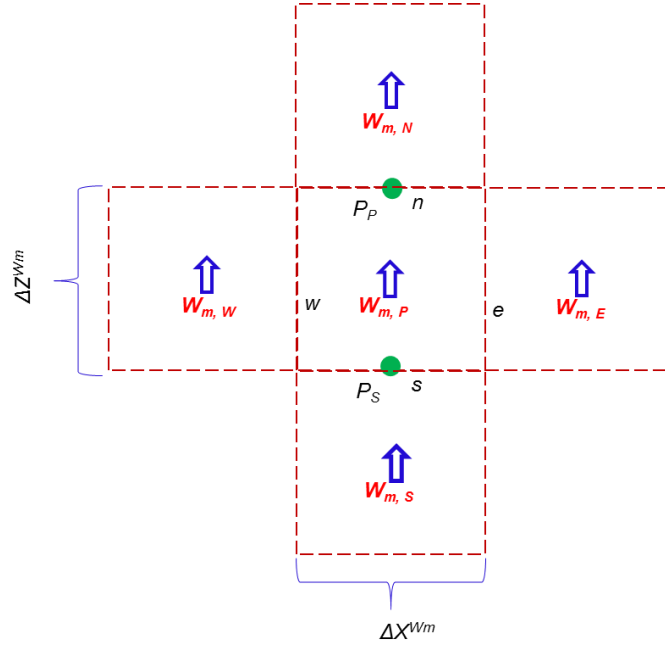


Figure 35 Control volume for mixture axial velocity W_m [48].

Similarly, the discretized form of the axial momentum equation on the W_m control volume is:

$$\left[\left[\frac{k_y \tilde{\mu}_m}{h} \right]_P^{W_m} \delta_x^{W_m} \delta_z^{W_m} + \sum_{nb} a_{nb}^{W_m} \right] w_{m,P} = \sum_{nb} (a_{nb}^{W_m} w_{m,nb}) + h_P^{W_m} (p_S - p_P) \delta z^{W_m} \quad (C-2)$$

where $h_P^{W_m}$ is the film thickness at the W_m control volume, δz^{W_m} is the axial length of the cell, the subscript 'nb' means neighboring flow variables (namely East, West, North and South), and

$$a_{nb}^{W_m} : \quad a_E^{W_m} = Re_p^* \left[[-F_e^w, 0] \right] (1 + r_3^e); \quad a_W^{W_m} = Re_p^* \left[[F_w^{W_m}, 0] \right] (1 + r_3^w)$$

$$a_N^{W_m} = Re_p^* \left[[-F_n^w, 0] \right] (1 + r_4^n); \quad a_S^{W_m} = Re_p^* \left[[F_s^{W_m}, 0] \right] (1 + r_4^s)$$

$$\sum_{nb} a_{nb}^{W_m} :$$

$$Re_p^* \left\{ \left[\left[F_e^{W_m}, 0 \right] \right] (1+r_3^e) + \left[\left[-F_w^{W_m}, 0 \right] \right] (1+r_3^w) + \left[\left[F_n^{W_m}, 0 \right] \right] (1+r_4^n) + \left[\left[-F_s^{W_m}, 0 \right] \right] (1+r_4^s) \right\}$$

The equation for pressure correction remains the same as those in Ref. [48].

In the above equations, the coefficients $(r_1)^{e,w}$ and $(r_2)^{n,s}$ are solved on the U_m control volume. Figure 36 shows the U_m control volume with the axial velocity W_m included. The figure introduces the indexes (i, j) to explain how the flow properties on the face of the U_m control volume are computed. For example, the mixture circumferential velocity $U_m(i, j) = U_{m,P}$, $U_m(i+1, j) = U_{m,E}$, $U_m(i-1, j) = U_{m,W}$, etc. Thus, on the east surface of the control volume, the flow variables $\Phi^e = (\alpha_g, \rho_g, \rho_m, U_m, P, \dots)^e$ are

$$\begin{aligned} P^e &= P(i+1, j) \\ \rho_g^e &= \frac{P^e}{ZR_g T} \\ \alpha_g^e &= \alpha_g(i+1, j) \\ \rho_m^e &= \alpha_g^e \rho_g^e + (1 - \alpha_g^e) \rho_l \\ c_g^e &= \frac{\alpha_g^e \rho_g^e}{\alpha_g^e \rho_g^e + (1 - \alpha_g^e) \rho_l} \end{aligned} \tag{C-3}$$

The velocity on the east face 'e' is computed as

$$\begin{aligned} U_m^e &= 0.5(U_m(i+1, j) + U_m(i, j)) \\ W_m^e &= 0.5(W_m(i+1, j+1) + U_m(i+1, j)) \end{aligned} \tag{C-4}$$

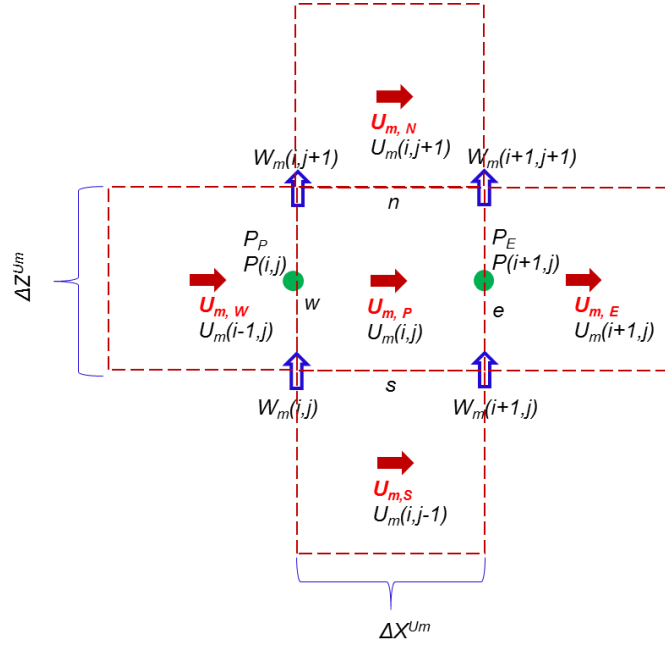


Figure 36 Control volume for U_m with axial velocity W_m included [48].

The velocity gradient on the east face 'e' is computed as

$$\begin{aligned} \left. \frac{\partial W_m}{\partial z} \right|^e &= \frac{W_m(i+1, j+1) - W_m(i+1, j)}{\Delta Z^{Um}} \\ \left. \frac{\partial U_m}{\partial z} \right|^e &= \frac{U_m(i+1, j) - U_m(i, j)}{\Delta X^{Um}} \end{aligned} \quad (C-5)$$

From Appendix A, the relative velocity between the liquid and air is

$$U_{gl}^e = \frac{\tau_g}{f_{drag(x)}} \frac{\rho_g - \rho_m}{\bar{\rho}_g} a_x \Big|_e \quad (C-6)$$

where $\tau_g^e = \frac{\rho_g d_g^2}{18\mu_l} \Big|_e$ is the air bubble relaxation time.

The drag coefficient

$$f_{drag} \Big| ^e = \begin{cases} 1 + 0.15 \text{Re}_{B(x)}^{0.687} \Big| ^e & \text{Re}_{B(x)} \Big| ^e \leq 1,000 \\ 0.0183 \text{Re}_{B(x)} \Big| ^e & \text{Re}_{B(x)} \Big| ^e > 1,000 \end{cases} \quad (\text{C-7})$$

where the relative Reynolds number $\text{Re}_{B(x)} \Big| ^e = \frac{\rho_l |U_{gl} | d_g \Big| ^e}{\mu_l}$, and the acceleration of the

gas phase $a_{X_0} \Big| ^e = g_x - \left(\frac{\partial \bar{U}_{m_0}}{\partial x} + \frac{\partial \bar{W}_{m_0}}{\partial z} \right) \bar{U}_{m_0} \Big| ^e$. If the seal is vertically positioned, $g_x = 0$.

The relative velocity U_{gl}^e in Eq. (C-6) can be solved using Newton-Raphson Method.

Then, the drift velocity is obtained from

$$U_{dr,g}^e = U_{gl} \left(1 - c_g \right) \Big| ^e \quad (\text{C-8})$$

Thus, the coefficient $(r_1)^e$

$$r_1^e = \frac{\alpha_g \rho_g U_{dr,g}^2 \Big| ^e}{\rho_m U_m^2} \quad (\text{C-9})$$

A similar process applies to the procedure to solve $(r_1)^w$, except that:

The velocity on the west face 'w' is computed as

$$\begin{aligned} U_m^w &= 0.5(U_m(i, j) + U_m(i-1, j)) \\ W_m^w &= 0.5(W_m(i, j+1) + U_m(i, j)) \end{aligned} \quad (\text{C-10})$$

The velocity gradient on the west face 'w' is computed as

$$\begin{aligned} \frac{\partial W_m}{\partial z} \Big| ^w &= \frac{W_m(i, j+1) - W_m(i, j)}{\Delta Z^U} \\ \frac{\partial U_m}{\partial z} \Big| ^w &= \frac{U_m(i, j) - U_m(i-1, j)}{\Delta X^U} \end{aligned} \quad (\text{C-11})$$

$$\begin{aligned}
a_E^{\alpha_g} &= \frac{\rho_g}{\rho_m} \left| \left[-F_e^{\alpha_g}, 0 \right] + \frac{1}{V_*} \left[-F_{De}^{\alpha_g}, 0 \right] \right|^e, \quad F_e^{\alpha_g} = \rho_m U_m h \delta z|^e, \quad F_{De}^{\alpha_g} = \rho_g U_{dr,g} h \delta z|^e \\
a_W^{\alpha_g} &= \frac{\rho_g}{\rho_m} \left| \left[F_w^{\alpha_g}, 0 \right] + \frac{1}{V_*} \left[F_{Dw}^{\alpha_g}, 0 \right] \right|^w, \quad F_w^{\alpha_g} = \rho_m U_m h \delta z|^w, \quad F_{Dw}^{\alpha_g} = \rho_g U_{dr,g} h \delta z|^w \\
a_N^{\alpha_g} &= \frac{\rho_g}{\rho_m} \left| \left[-F_n^{\alpha_g}, 0 \right] + \frac{1}{V_*} \left[-F_{Dn}^{\alpha_g}, 0 \right] \right|^n, \quad F_n^{\alpha_g} = \rho_m W_m h \delta z|^n, \quad F_{Dn}^{\alpha_g} = \rho_g W_{dr,g} h \delta z|^n \\
a_S^{\alpha_g} &= \frac{\rho_g}{\rho_m} \left| \left[F_s^{\alpha_g}, 0 \right] + \frac{1}{V_*} \left[F_{Ds}^{\alpha_g}, 0 \right] \right|^s, \quad F_s^{\alpha_g} = \rho_m U_m h \delta z|^s, \quad F_{Ds}^{\alpha_g} = \rho_g W_{dr,g} h \delta z|^s \\
\\
a_p^{\alpha_g} &= \frac{\rho_g}{\rho_m} \left| \left[F_e^{\alpha_g}, 0 \right] + \frac{1}{V_*} \left[F_{De}^{\alpha_g}, 0 \right] + \frac{\rho_g}{\rho_m} \left| \left[-F_w^{\alpha_g}, 0 \right] + \frac{1}{V_*} \left[-F_{Dw}^{\alpha_g}, 0 \right] + \right. \right. \\
&\quad \left. \left. \frac{\rho_g}{\rho_m} \left| \left[F_n^{\alpha_g}, 0 \right] + \frac{1}{V_*} \left[F_{Dn}^{\alpha_g}, 0 \right] + \frac{\rho_g}{\rho_m} \left| \left[-F_s^{\alpha_g}, 0 \right] + \frac{1}{V_*} \left[-F_{Ds}^{\alpha_g}, 0 \right] \right| \right| \right|^e
\end{aligned}$$

This report uses the computational analysis on a homogeneous bulk flow [10] as a basis to solve the nonhomogeneous bulk flow equations. The steps in the numerical solution procedure are:

- a) Setup boundary conditions for zeroth order equations.
- b) Initial guess of the pressure p^0 , velocities (u_m^0, w_m^0) , and gas volume fraction α_g^0 .
- c) On the second row W_m control volume, calculate the coefficients of the axial momentum equations based on the existing flow variables. Use tri-diagonal matrix algorithm (TDMA) to solve the second row axial velocity w_m^k .
- d) Repeat step c) for the second row U_m control volume to solve the circumferential velocity u_m^k .

- e) Use the obtained u_m^k, w_m^k to calculate the correction pressure p' .
- f) Use SIMPLEC method to calculate the correction velocities (u_m', w_m').
- g) Use under relaxation to correct the velocities and pressure:

$$p^{k+1} = p^k + \beta_1 p'$$

$$u_m^{k+1} = u_m^k + \beta_2 u_m'$$

$$w_m^{k+1} = w_m^k + \beta_2 w_m'$$

where β_1 and β_2 are the under relaxation factors for the pressure and velocity.

- h) Use the corrected u_m^{k+1}, w_m^{k+1} , pressure p^{k+1} to solve the gas volume fraction equation α_g^{k+1} .
- i) Use the pressure and gas volume fraction to update the mixture density (ρ_m^{k+1}) and viscosity (μ_m^{k+1}).
- j) Repeat steps c) to i) along the Z direction to solve the U_m and W_m momentum equations, pressure and gas volume equations till the end row of the U_m, W_m, P_m and α_g .
- k) Update the inlet and outlet velocities $(u_m^{k+1})_{in,out}, (w_m^{k+1})_{in,out}$, pressure $(p^{k+1})_{in,out}$, and gas volume fraction $(\alpha_g^{k+1})_{in,out}$ based on the inland $u_m^{k+1}, w_m^{k+1}, p^{k+1}$, and α_g^{k+1} .
- l) Convergence criteria: in each of the control volume, if $|P_{new} - P_{old}| / P_{new} < 0.001$, then the zeroth order equation is considered as converged. If $|P_{new} - P_{old}| / P_{new} > 0.001$, the program returns to step c) to start the new iteration until the convergence

criteria is satisfied. The program is forced to run at least three iterations even though the program reached the convergence criteria at the first iteration.

m) After the flow field is converged, the seal mass flow rate, shear drag torque can be calculated using Eq. (67) and (68).

Numerical solution of the first order equation

Once the zeroth order flow field is obtained, the coefficients of the first order continuity, momentum, and gas volume fraction equations at a specified excitation frequency (ω) can be calculated. The steps a) to k) for the zeroth order equations is adapted to solve the perturbed flow fields ($u_\chi, w_\chi, p_\chi, \alpha_{g\chi}$, the subscribe $\chi = x, y$).

APPENDIX D

FORCE COEFFICIENTS OF HIGH PRESSURE ANNULAR SEAL

Figure 38 through 42 show the measured [55] and predicted dynamic force coefficients versus inlet GVF of a seal having a nominal diameter $D = 89.3$ mm, length $L = 57.8$ mm ($L/D = 0.65$), and a radial clearance $c = 0.163 \pm 0.005$ mm. Table 1 lists the liquid and gas physical properties. During the test the seal supply pressure is 31 bara, the discharge pressure is 6.9 bara, and the shaft speed is 7,500 rpm. The symbols represent test data, the solid lines represent predictions from the current NHBFM, and the broken lines stand for predictions based on the HBFM [10].

Figure 38 shows the measured and predicted seal direct stiffness (K) versus inlet GVF. Both the homogeneous bulk flow model (HBFM) [10] and the current nonhomogeneous bulk flow model (NHBFM) predict a drop in K as the inlet GVF increases from 0 to 10%. The NHBFM predicted K reduces faster than the one predicted from the HBFM.

Figure 39 shows the direct mass coefficient (M) versus inlet GVF. Both the measured and predicted added masses (M) reduce with the increase of inlet GVF. The NHBFM predicts a $\sim 5\%$ larger M compared to the HBFM does. Compared to the test data, the NHBFM under predict M by about 20%.

Figure 40 and Figure 41 show the measured and predicted cross-coupled stiffness (k) and direct damping (C) versus inlet GVF. As the inlet GVF increases from 0 to 0.1, the cross-coupled stiffness (k) increases from 10 MN/m to 14 MN/m. The direct damping (C) increases slightly from 40 kN.s/m to ~ 42 kN.s/m. Both models under predict k and C by

~ 20%.

Figure 42 shows the cross-coupled damping (c) versus inlet GVF. Similar to the results presented in Section 4, the cross-coupled damping (c) reduces continuously with inlet GVF. Both models deliver accurate predictions as compared to the test data [55].

Lastly, Figure 43 shows the predicted and experimentally estimated seal whirl frequency ratio (f_w) versus inlet GVF. For operation with a pure liquid the seal shows a whirl frequency ratio $f_w = 0.31$. For operation with a mixture f_w increases to ~ 0.42. Both the NHBFM and the HBFM accurately predict f_w , as compared to the test data in Ref. [55].

Comparisons of the predicted force coefficients against the test data for the third seal reinforce the conclusions drawn in section 4, in particular that the NHBFM predicted $Re(H)$ reduces faster with inlet GVF than that predicted by the HBFM.

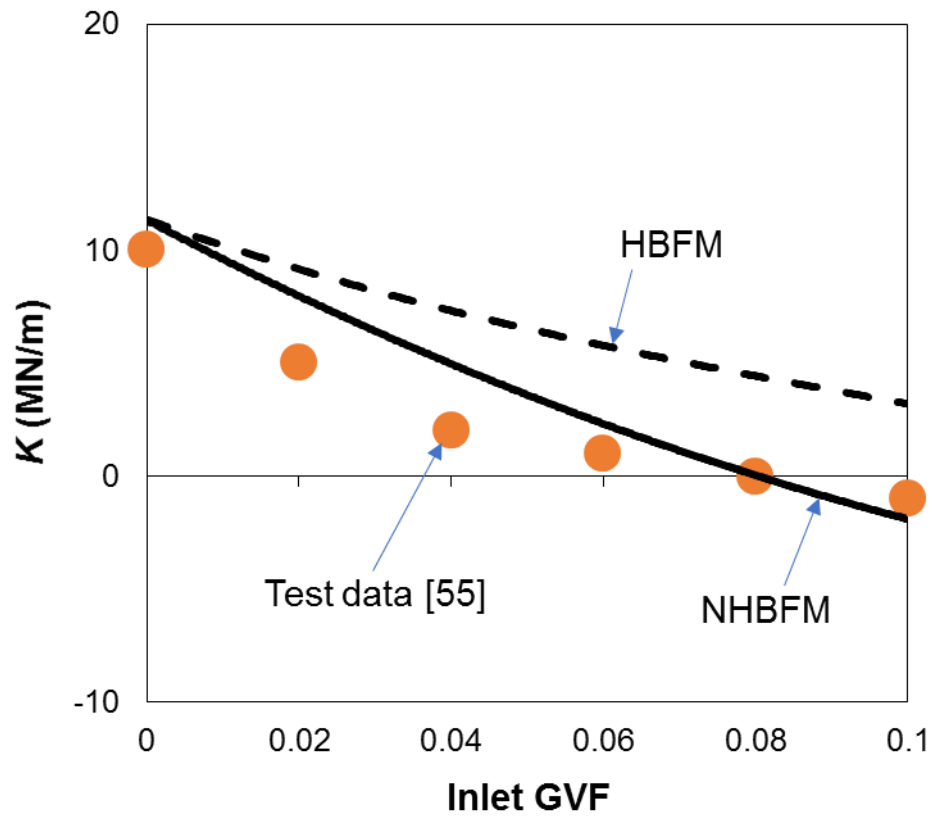


Figure 38 Direct stiffness (K) versus inlet GVF. Shaft speed 7,500 rpm, seal inlet pressure 31 bara, discharge pressure 6.9 bara. Symbols: test data in Ref.[55], Solid line: prediction from NHBFM. Broken line: prediction from HBFM.

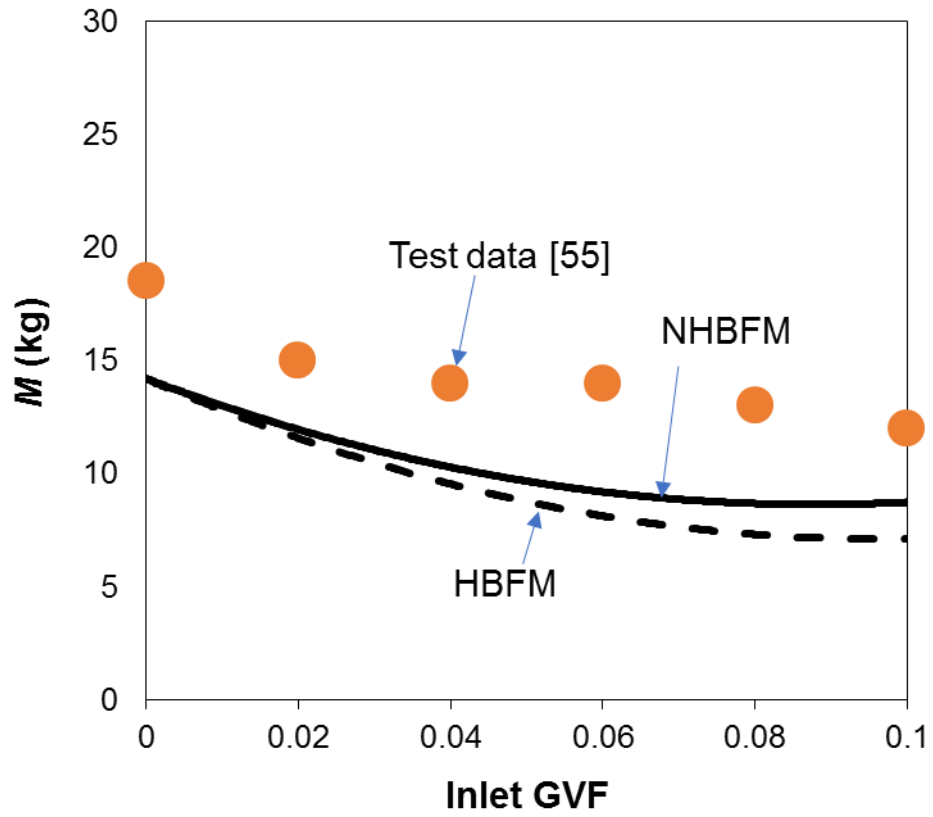


Figure 39 Added mass (M) versus inlet GVF. Shaft speed 7,500 rpm, seal inlet pressure 31 bara, discharge pressure 6.9 bara. Symbols: test data in Ref.[55], Solid line: prediction from NHBFM. Broken line: prediction from HBFM.

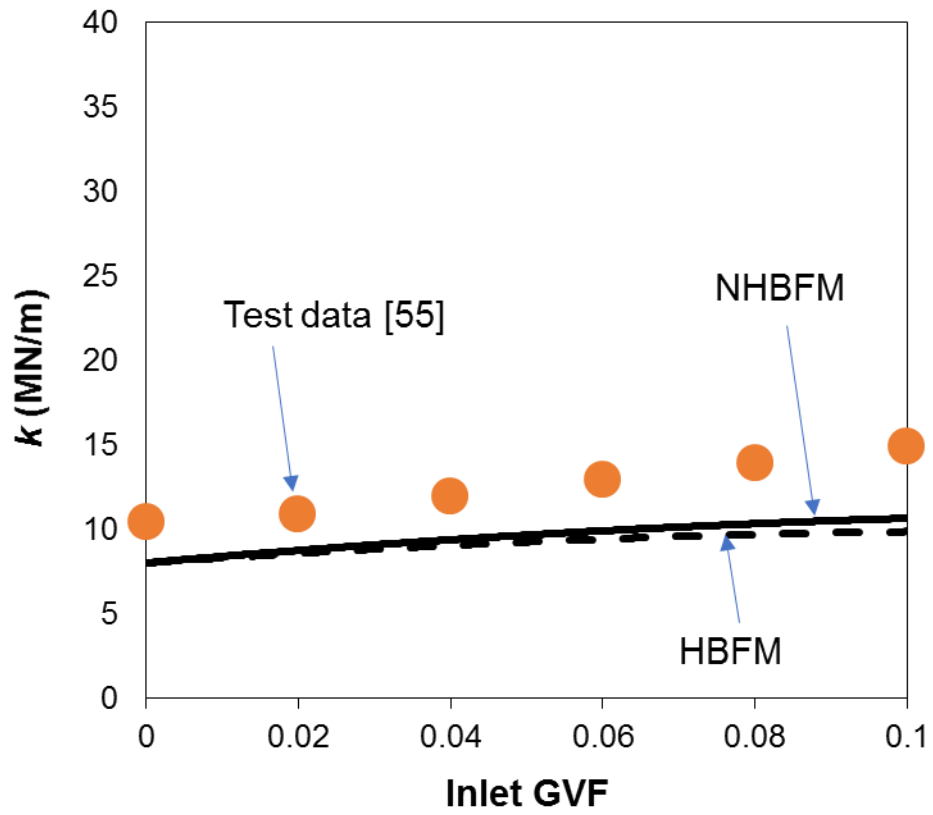


Figure 40 Cross-coupled stiffness (k) versus inlet GVF. Shaft speed 7,500 rpm, seal inlet pressure 31 bara, discharge pressure 6.9 bara. Symbols: test data in Ref.[55], Solid line: prediction from NHBFM. Broken line: prediction from HBFM.

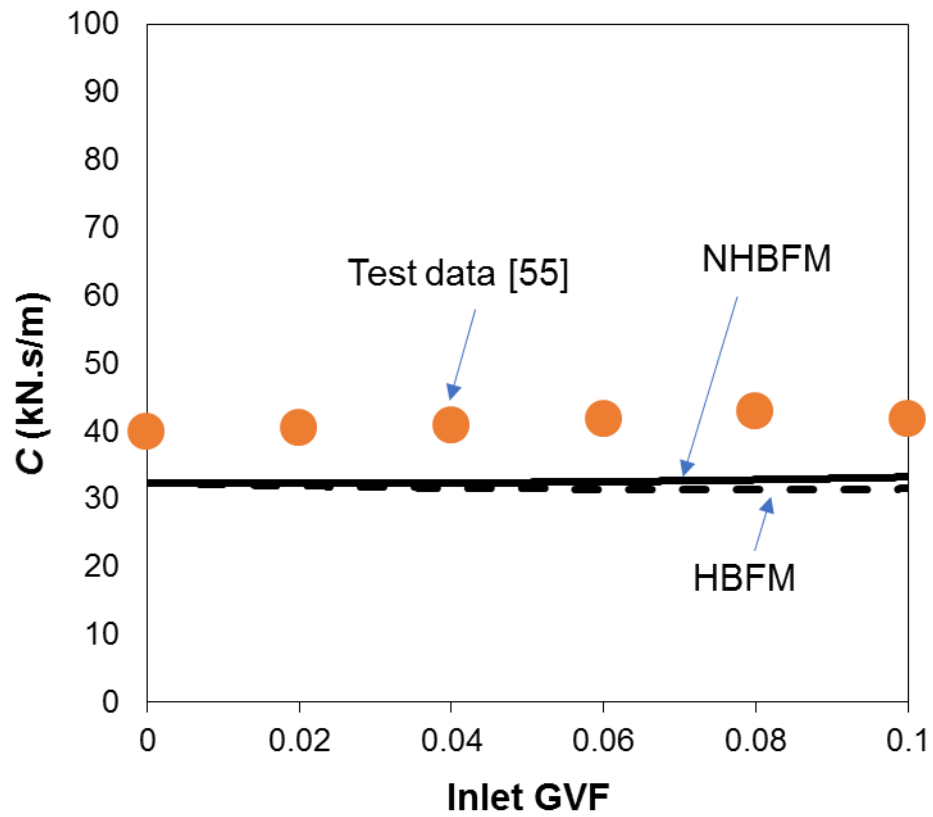


Figure 41 Direct damping (C) versus inlet GVF. Shaft speed 7,500 rpm, seal inlet pressure 31 bara, discharge pressure 6.9 bara. Symbols: test data in Ref.[55], Solid line: prediction from NHBFM. Broken line: prediction from HBFM.

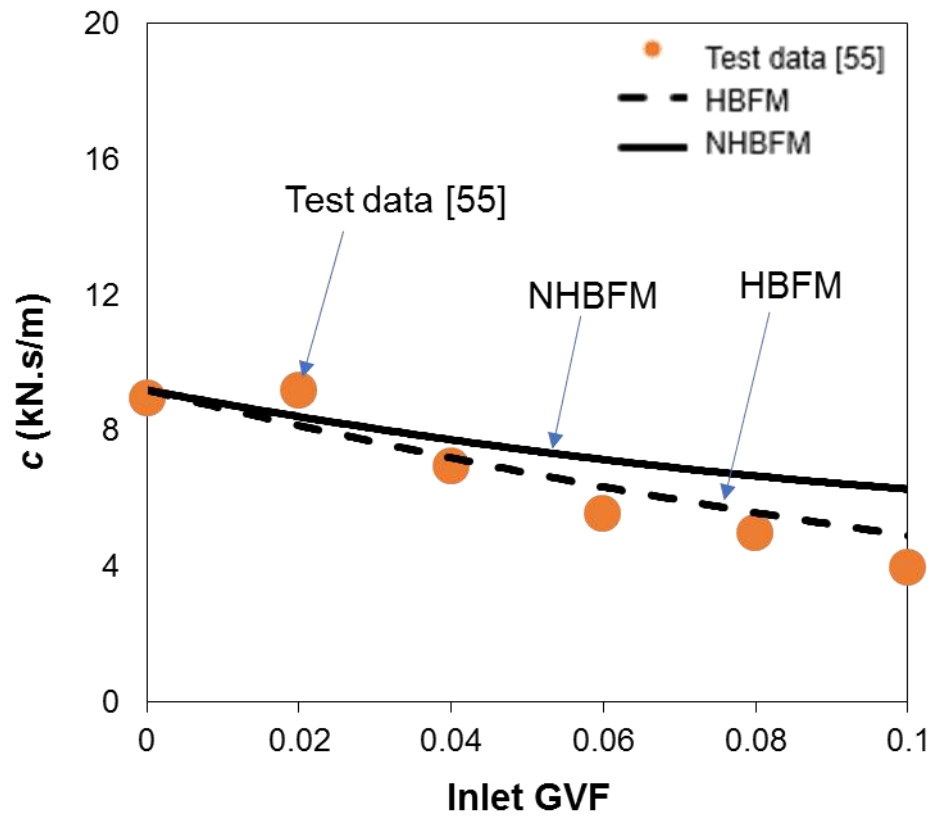


Figure 42 Cross-coupled damping (c) versus inlet GVF. Shaft speed 7,500 rpm, seal inlet pressure 31 bara, discharge pressure 6.9 bara. Symbols: test data in Ref.[55], Solid line: prediction from NHBFM. Broken line: prediction from HBFM.

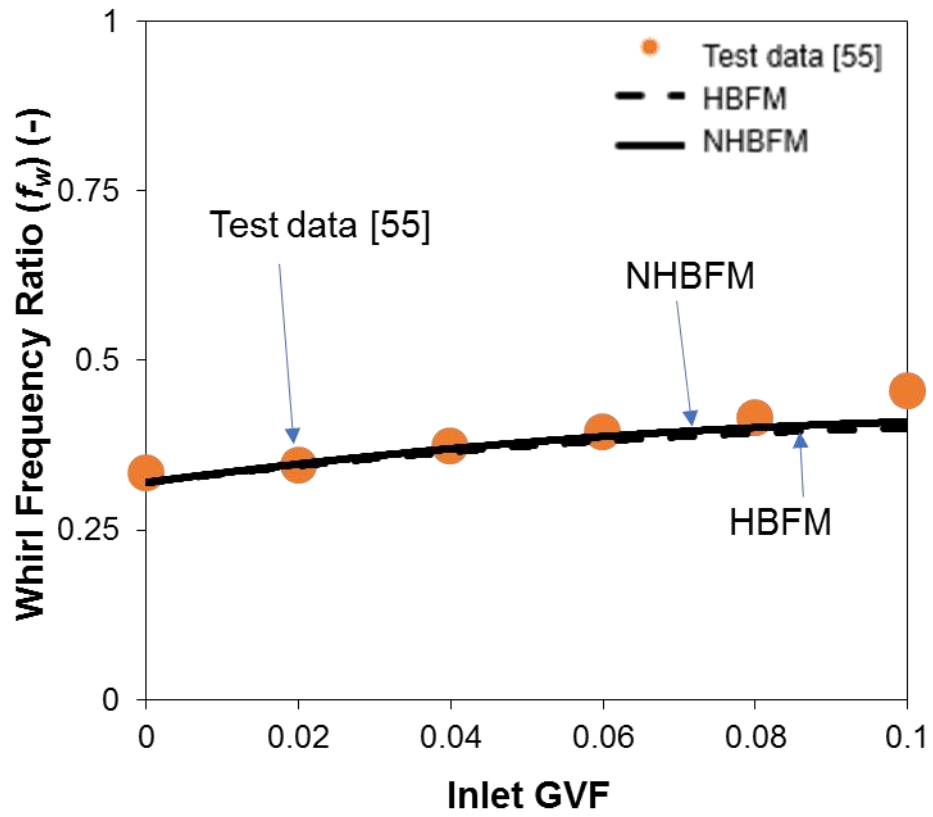


Figure 43 Whirl frequency ratio (f_w) versus inlet GVF. Shaft speed 7,500 rpm, seal inlet pressure 31 bara, discharge pressure 6.9 bara. Symbols: test data in Ref.[55], Solid line: prediction from NHBFM. Broken line: prediction from HBFM.